



2002-09

# Measurements and observations of interfacial creep in engineering systems

Peterson, Keith A.

Monterey, California. Naval Postgraduate School, 2002.

---

<http://hdl.handle.net/10945/9811>



Calhoun is a project of the Dudley Knox Library at NPS, furthering the precepts and goals of open government and government transparency. All information contained herein has been approved for release by the NPS Public Affairs Officer.

**Dudley Knox Library / Naval Postgraduate School**  
**411 Dyer Road / 1 University Circle**  
**Monterey, California USA 93943**

<http://www.nps.edu/library>

# **NAVAL POSTGRADUATE SCHOOL**

## **Monterey, California**



## **DISSERTATION**

### **MEASUREMENTS AND OBSERVATIONS OF INTERFACIAL CREEP IN ENGINEERING SYSTEMS**

by

Keith A. Peterson

September 2002

Dissertation Supervisor:

Indranath Dutta

**Approved for public release; distribution is unlimited**

THIS PAGE INTENTIONALLY LEFT BLANK

<b>REPORT DOCUMENTATION PAGE</b>			<i>Form Approved OMB No. 0704-0188</i>	
Public reporting burden for this collection of information is estimated to average 1 hour per response, including the time for reviewing instruction, searching existing data sources, gathering and maintaining the data needed, and completing and reviewing the collection of information. Send comments regarding this burden estimate or any other aspect of this collection of information, including suggestions for reducing this burden, to Washington headquarters Services, Directorate for Information Operations and Reports, 1215 Jefferson Davis Highway, Suite 1204, Arlington, VA 22202-4302, and to the Office of Management and Budget, Paperwork Reduction Project (0704-0188) Washington DC 20503.				
<b>1. AGENCY USE ONLY (Leave blank)</b>		<b>2. REPORT DATE</b> September 2002	<b>3. REPORT TYPE AND DATES COVERED</b> Dissertation	
<b>4. TITLE AND SUBTITLE:</b> Measurements and Observations of Interfacial Creep in Engineering Systems			<b>5. FUNDING NUMBERS</b>	
<b>6. AUTHOR(S)</b> Keith A. Peterson				
<b>7. PERFORMING ORGANIZATION NAME(S) AND ADDRESS(ES)</b> Naval Postgraduate School Monterey, CA 93943-5000			<b>8. PERFORMING ORGANIZATION REPORT NUMBER</b>	
<b>9. SPONSORING / MONITORING AGENCY NAME(S) AND ADDRESS(ES)</b> N/A			<b>10. SPONSORING / MONITORING AGENCY REPORT NUMBER</b>	
<b>11. SUPPLEMENTARY NOTES</b> The views expressed in this thesis are those of the author and do not reflect the official policy or position of the Department of Defense or the U.S. Government.				
<b>12a. DISTRIBUTION / AVAILABILITY STATEMENT</b> Approved for public release; distribution is unlimited			<b>12b. DISTRIBUTION CODE</b>	
<b>13. ABSTRACT (maximum 200 words)</b> In many applications, large shear stresses develop at interfaces between dissimilar materials during thermo-mechanical excursions, when there is a significant difference in the coefficient of thermal expansion between them. When the system is elevated to a high homologous temperature for one of the adjoining materials, the applied shear stress may allow the interface to slide without debonding by a diffusionally accommodated mechanism, thereby allowing relative dimensional changes to occur. The purpose of this dissertation is to establish the kinetics and mechanism of interfacial creep and to evaluate its impact on thin film structures used in microelectronic devices. Studies of interfacial creep kinetics were based on diffusion-bonded interfaces in Si-Al-Si sandwich specimens, which were loaded in a double-shear configuration with the interfaces being subjected to a nominal shear stress during creep tests. In some tests, a normal stress was superimposed on the applied shear stress to articulate the role of the normal stresses, which are often present at interfaces. It was found that in agreement with previous results, the interface crept by interfacial diffusion-controlled diffusional creep driven by the applied shear stress, with the applied normal compressive stress resulting in a threshold behavior below which no creep occurred. The effect of interfacial roughness was also evaluated and the results showed that the interfacial creep rate decreased for specimens with larger interfacial roughness. The impact of interfacial creep in interconnect structures in microelectronic devices were observed via atomic force microscopy for (a) stand-alone thin film Cu lines on Si and (b) Cu lines embedded in a low k dielectric on Si substrates. Following thermal cycling, changes were observed in the in-plane Cu line dimensions, as well as the out-of plane step height between Cu and dielectric in single layer structures. Both effects were attributed to interfacial diffusion-controlled interface sliding.				
<b>14. SUBJECT TERMS</b> Interface Sliding, Interfacial Creep, Al-Si Interface, Activation Energy, Amorphous, Diffusion Bonding, Interconnect Structures			<b>15. NUMBER OF PAGES</b> 145	
			<b>16. PRICE CODE</b>	
<b>17. SECURITY CLASSIFICATION OF REPORT</b> Unclassified	<b>18. SECURITY CLASSIFICATION OF THIS PAGE</b> Unclassified	<b>19. SECURITY CLASSIFICATION OF ABSTRACT</b> Unclassified	<b>20. LIMITATION OF ABSTRACT</b> UL	

NSN 7540-01-280-5500

Standard Form 298 (Rev. 2-89)  
Prescribed by ANSI Std. Z39-18

THIS PAGE INTENTIONALLY LEFT BLANK

**Approved for public release; distribution is unlimited**

**MEASUREMENTS AND OBSERVATIONS OF INTERFACIAL CREEP IN  
ENGINEERING SYSTEMS**

Keith A. Peterson  
Lieutenant Commander, United States Navy  
B.S., Florida Tech, 1990  
M.S., Naval Postgraduate School, 2000  
M.E., Naval Postgraduate School, 2000

Submitted in partial fulfillment of the  
requirements for the degree of

**DOCTOR OF PHILOSOPHY IN MECHANICAL ENGINEERING**

from the

**NAVAL POSTGRADUATE SCHOOL  
September 2002**

Author:

\_\_\_\_\_  
Keith A. Peterson

Approved by:

\_\_\_\_\_  
Indranath Dutta  
Professor of Mechanical Engineering  
Dissertation Supervisor

\_\_\_\_\_  
Indranath Dutta  
Professor of Mechanical Engineering  
Dissertation Committee Chair

\_\_\_\_\_  
Terry McNelley  
Professor of Mechanical Engineering

\_\_\_\_\_  
Young Kwon  
Professor of Mechanical Engineering

\_\_\_\_\_  
James Luscombe  
Professor of Physics

\_\_\_\_\_  
Gamani Karunasiri  
Professor of Physics

Approved by:

\_\_\_\_\_  
Young Kwon, Chair, Department of Mechanical Engineering

Approved by:

\_\_\_\_\_  
Carson K. Eoyang, Associate Provost for Academic Affairs

THIS PAGE INTENTIONALLY LEFT BLANK

## ABSTRACT

In many applications, large shear stresses develop at interfaces between dissimilar materials during thermo-mechanical excursions, when there is a significant difference in the coefficient of thermal expansion between them. When the system is elevated to a high homologous temperature for one of the adjoining materials, the applied shear stress may allow the interface to slide without debonding by a diffusionally accommodated mechanism, thereby allowing relative dimensional changes to occur. The purpose of this dissertation is to establish the kinetics and mechanism of interfacial creep and to evaluate its impact on thin film structures used in microelectronic devices. Studies of interfacial creep kinetics were based on diffusion-bonded interfaces in Si-Al-Si sandwich specimens, which were loaded in a double-shear configuration with the interfaces being subjected to a nominal shear stress during creep tests. In some tests, a normal stress was superimposed on the applied shear stress to articulate the role of the normal stresses, which are often present at interfaces. It was found that in agreement with previous results, the interface crept by interfacial diffusion-controlled diffusional creep driven by the applied shear stress, with the applied normal compressive stress resulting in a threshold behavior below which no creep occurred. The effect of interfacial roughness was also evaluated and the results showed that the interfacial creep rate decreased for specimens with larger interfacial roughness. The impact of interfacial creep in interconnect structures in microelectronic devices were observed via atomic force microscopy for (a) stand-alone thin film Cu lines on Si and (b) Cu lines embedded in a low k dielectric on Si substrates. Following thermal cycling, changes were observed in the in-plane Cu line dimensions, as well as the out-of plane step height between Cu and dielectric in single layer structures. Both effects were attributed to interfacial diffusion-controlled interface sliding.



THIS PAGE INTENTIONALLY LEFT BLANK

# TABLE OF CONTENTS

<b>I.</b>	<b>INTRODUCTION.....</b>	<b>1</b>
<b>II.</b>	<b>BACKGROUND.....</b>	<b>5</b>
<b>A.</b>	<b>EXAMPLES OF INTERFACIAL SLIDING IN ENGINEERING SYSTEMS .....</b>	<b>5</b>
1.	Microelectronics .....	5
2.	Superplasticity of Particulate Composites .....	7
3.	Metal-Matrix Composites .....	8
<b>B.</b>	<b>POSSIBLE MECHANISMS OF INTERFACIAL SLIDING .....</b>	<b>12</b>
<b>C.</b>	<b>DIRECT MEASUREMENT OF INTERFACIAL CREEP KINETICS .....</b>	<b>16</b>
<b>III.</b>	<b>OBJECTIVES.....</b>	<b>19</b>
<b>IV.</b>	<b>PROCESSING AND CHARACTERIZATION OF DIFFUSION BONDED Al-Si INTERFACES .....</b>	<b>21</b>
<b>A.</b>	<b>INTRODUCTION.....</b>	<b>21</b>
<b>B.</b>	<b>EXPERIMENTAL PROCEDURE.....</b>	<b>22</b>
1.	Material Selection.....	22
2.	Sample Preparation.....	24
3.	Diffusion Bonding.....	26
4.	Specimen Preparation for Microscopy.....	29
<b>C.</b>	<b>RESULTS AND DISCUSSION.....</b>	<b>29</b>
<b>D.</b>	<b>CONCLUSION.....</b>	<b>41</b>
<b>V.</b>	<b>KINETICS OF INTERFACIAL CREEP AT Al-Si INTERFACES .....</b>	<b>43</b>
<b>A.</b>	<b>INTRODUCTION.....</b>	<b>43</b>
<b>B.</b>	<b>EXPERIMENTAL PROCEDURE.....</b>	<b>45</b>
<b>C.</b>	<b>RESULTS.....</b>	<b>49</b>
<b>D.</b>	<b>DISCUSSION .....</b>	<b>63</b>
<b>E.</b>	<b>CONCLUSION.....</b>	<b>78</b>
<b>VI.</b>	<b>INTERFACIAL SLIDING OF INTERCONNECT STRUCTURES IN MICROELECTRONIC DEVICES .....</b>	<b>81</b>
<b>A.</b>	<b>STANDALONE Cu INTERCONNECTS ON Si.....</b>	<b>81</b>
1.	Introduction .....	81
2.	Background.....	82
3.	Experimental Approach .....	84
4.	Modeling Approach.....	85
5.	Results .....	86
a.	<i>Experimental</i> .....	86
b.	<i>Modeling</i> .....	91
6.	Discussion .....	102
7.	Conclusions .....	105
<b>B.</b>	<b>Cu/LOW k DIELECTRIC STRUCTURES ON Si .....</b>	<b>107</b>

1.	Introduction .....	107
2.	Experimental Approach .....	108
3.	Results and Discussion .....	109
4.	Conclusions .....	116
VII. CONCLUSIONS.....		117
LIST OF REFERENCES .....		119
INITIAL DISTRIBUTION LIST .....		125

## LIST OF FIGURES

Figure 1.	(a) Schematic of Cu/PI HDIC on Si with Ta Interlayers. (b) Surface Profile Before and After Thermal Cycling, and Plot Showing Differential Deformation of Cu and PI via Sliding at Cu/Ta Interface [11].	5
Figure 2.	Schematic of Interfacial Shear Stress Distribution along the Width of a Narrow Thin-Film Line. The Film is in In-Plane Biaxial Tension.	6
Figure 3.	In Superplasticity of Particulate Composites, Sliding between Matrix Grains is Accommodated by Diffusional Sliding at Particle-Matrix Interfaces [25].	8
Figure 4.	Cu-Matrix Protruding Beyond the Ends of W-Fibers after Thermal Cycling [1].	9
Figure 5.	(a) Sample Utilized to Separately Measure Matrix and Fiber Strains during Uniaxial Creep Tests. (b) Differential Matrix and Fiber Strain Response during Creep Indicates Interfacial Sliding [4].	10
Figure 6.	Intrusion and Protrusion of Graphite Fiber-Ends Relative to an Al-Matrix Following Slow Thermal Cycling from 298K to 380K and 600K, Respectively [5].	11
Figure 7.	Optical Micrograph of Al Before Prior to Diffusion Bonding, Showing a Nominal Grain Size of 140 $\mu$ m - 150 $\mu$ m.	23
Figure 8.	AFM Roughness Measurements on the Surface of Silicon after Using Various Grits and Grit Sizes During Final Polishing.	25
Figure 9.	AFM Roughness Measurements on the Surface of Aluminum after Using Various Grits and Grit Sizes During Final Polishing.	26
Figure 10.	Schematic of Die, Punch and Specimen Lay-Up Used in Diffusion Bonding.	27
Figure 11.	Diffusion Bonding Apparatus Using a Mechanical Testing System, High Vacuum System, Cylindrical Furnace, Welded Bellows, Die and Punch.	28
Figure 12.	(a) Surface Topography, $h/2$ , and (b) Ratio of Height over Wavelength, $h/\lambda$ , for Si and Al as a Function of the Final Polish Used.	31
Figure 13.	Si/Al Interface Morphology after Diffusion Bonding at 855K (Slightly Above the Eutectic Temperature for ~10 Minutes at 3MPa. The Micrograph Shows that In-Situ Melting of the Interfacial Region Produces a Thick Interfacial Region with Non-planar Si-Al Interfaces.	32
Figure 14.	Optical Micrograph of Diffusion Bonded Si/Al Interface Etched in Modified Keller's Reagent. The Grain Size of Al Close to the Interface is Significantly Smaller than that Farther Away.	33

Figure 15.	OIM Micrograph Showing Small Al Grains ( $\sim 20 - 80\mu\text{m}$ ) Immediately Adjacent to the Interface and Larger Grains ( $\sim 100 - 150\mu\text{m}$ ) Farther Away (a). The Grains Far from the Interface Have a Cube Texture (b), Whereas Those Immediately Adjacent to the Interface Have No Texture (c). ....	34
Figure 16.	(a) Bright Field TEM Image Showing a Diffusion Bonded Si/Al Interface, (b) Microstructure of Al Away from Interface Showing Larger Grains $\sim 1-2\mu\text{m}$ , and (c) Showing Small Grains/Subgrains with Size of $\sim 300\text{nm}$ along the Interface and Very Low Dislocation Density. ....	35
Figure 17.	X-Ray Maps Across the Si/Al Interface Showing a Thin Oxygen-Rich Layer, Where Trace Contaminants (i.e., Sulfur) Segregate. ....	37
Figure 18.	HREM Micrograph Showing Lattice Image of the Single Crystal Si, a Sharp Interface Between the Si and $\sim 40\text{nm}$ Thick Amorphous Region, and a Gradual Transition from the Amorphous Region to the Al Crystal. ....	38
Figure 19.	Plot of $\tau$ Versus $\delta$ at 538K, Showing the Onset of Non-Linearity ( $\sim 4.5\text{MPa}$ ) Commensurate with Shear Yielding of a Very Thin Region of Al Immediately Adjacent to the Si-Al interfaces. Inset Shows the Testing Configuration for the Double Shear Al/Si/Al Specimen. ....	39
Figure 20.	Approximate Interfacial Roughness Corresponding to the Height $h$ and Ratio of Height over Wavelength $h/\lambda$ of the Asperities of Si as a Function of Grit Size Used During Final Polishing. ....	46
Figure 21.	Photo of Interfacial Creep Test Specimen, and (b) Schematic of the Loading Geometry. ....	47
Figure 22.	Experimental Approach for Sample Mounting for Double-Shear Test Specimens Showing Applied Interfacial Shear and Normal Stresses. ....	48
Figure 23.	Micrograph Showing Misalignment of Rows of Al Grid Pattern Deposited Across an Al/Si Interface Following Creep Testing at 1MPa and 573K for 4 hours. ....	49
Figure 24.	Example Interfacial Creep Curves at Various Shear Stresses and Temperatures. ....	50
Figure 25.	Plots (a) and (b) Showing Linear Stress Dependence of Interfacial Displacement Rate. Plot (b) Showing Temperature Normalized Displacement Rate as a Function of Interfacial Shear Stress. ....	52
Figure 26.	Plot (a) Showing Arrhenius Temperature Dependence of Interfacial Displacement Rate, with an Apparent Activation Energy of $\sim 42\text{kJ/mol}$ . Plot (b) Showing Arrhenius Temperature Dependence and Same Activation Energy of $\sim 42\text{kJ/mol}$ . ....	53
Figure 27.	SEM Micrograph at a $45^\circ$ Tilt Showing Al-Si-Al Specimen Bottom that Underwent Interfacial Creep at 573K and 2MPa. The Sample Shown Has a PVD Al Film of $\sim 500\text{nm}$ . ....	54

Figure 28.	Interface Displacement Over Time Showing Interface Displacement Increases with Decreasing Applied Interfacial Normal Stress at a Constant Temperature (623K) and Interfacial Shear Stress ( $\tau_i = 1.0\text{MPa}$ ). .....	55
Figure 29.	Interface Displacement Rate as a Function of Interface Shear Stress Showing Linear Stress Dependence with Corresponding Threshold Stress for Four Applied Interfacial Normal Stresses at 623K and 523K. ....	56
Figure 30.	Interface Displacement Rate as a Function of Interface Shear Stress Showing Linear Stress Dependence with Corresponding Threshold Stress for Four Applied Interfacial Normal Stresses at 523K and 423K. ....	57
Figure 31.	Temperature Normalized Interface Displacement Rate Showing Linear Stress Dependence with Corresponding Threshold Stress for Four Applied Interfacial Normal Stresses. ....	59
Figure 32.	Interfacial Shear Stress and Temperature Normalized Interfacial Displacement Rate Showing Arrhenius Temperature Dependence with an Apparent Activation Energy of $\sim 42\text{kJ/mol}$ with Applied Interfacial Normal Stress. ....	59
Figure 33.	Typical Interfacial Creep Curves at 624K with an Applied Interfacial Shear Stress of $1.5\text{MPa}$ for Three Interfacial Roughnesses ( $h \approx 18, 54,$ and $174\text{nm}$ ) with No Interfacial Normal Stress. Plot Shows an Increase in Interface Displacement for Smoother Surfaces. ....	61
Figure 34.	Interfacial Displacement Rate as a Function of Applied Average Interfacial Shear Stress with No Interfacial Normal Stress Applied for Three Interfacial Roughnesses ( $h \approx 18, 54,$ and $174\text{nm}$ ). The System Exhibits Linear Stress Dependence with No Threshold Stress. ....	61
Figure 35.	(a) Interfacial Displacement Rate as a Function of the Inverse of Interfacial Roughness Showing Squared Showing an Increase in the Interfacial Displacement Rate as the Applied Interfacial Shear Stress Increases for all Interfacial Roughnesses and (b) Interfacial Shear Stress Normalized Displacement Rate Plot is in Agreement with Interfacial Sliding Equation 5.1. ....	62
Figure 36.	Interfacial Displacement Rate as a Function of Applied Interfacial Shear Stress When an Normal Stress is Applied Showing a Linear Shear Stress Dependence with an Observed Threshold Stress. Observed Threshold Stress Increases with Increasing Applied Interfacial Normal Stress and Interfacial Roughness. ....	63
Figure 37.	HREM Micrograph Showing Lattice Image of the Single Crystal Si, a Sharp Interface Between the Si and the $\sim 40\text{nm}$ Thick Amorphous Region, and a Gradual Transition from the Amorphous Region to the Al Crystal Before Creep Testing. ....	65

Figure 38.	HREM Micrograph Showing Lattice Image of the Single Crystal Si, a Sharp Interface Between the Si and the ~40nm Thick Amorphous Region, and a Gradual Transition to a Nanocrystalline Region of Al Before Creep Testing.....	72
Figure 39.	After a Typical Creep Test (>24hours, 624K, 1.5MPa), a HREM Micrograph Shows Lattice Images of (from Left to Right) a Single Crystal Si Adjacent to a Nanocrystalline Region, Which is Next to an Al and O-Rich Amorphous Region Followed by Another Nanocrystalline Region Adjacent to the Al Crystal.....	73
Figure 40.	AFM Image of an Array of Square Al Thin Film Islands on Si. Each Island is Nominally 250nm Thick and Has Lateral Dimensions of 6 $\mu$ m x 6 $\mu$ m. [6].....	84
Figure 41.	AFM Image of an Array of Parallel Cu Lines on Si. The Lines are Nominally 250nm Thick and 1.4 $\mu$ m Wide. ....	85
Figure 42.	Schematic of the Film-Substrate System Used for the FE Model where $l_f$ is the Film Width and $t_f$ is the Film Thickness, and $t_s$ the Substrate Thickness. Since the System is Laterally Symmetric, Only Half of the System (Corresponding to Positive x-Values) was Modeled. [6] .....	86
Figure 43.	Representative Cross-Sectional Profiles of the Square Al Films Before and After 5 Thermal Cycles from 293 to 623K. [6].....	87
Figure 44.	Histograms and the Associated Gaussian Fits of the Width Distribution of the Square Al Films at a Distance of 20nm from the Interface; (a) Before Thermal Cycles; and (b) After 5 Thermal Cycles. [6] .....	88
Figure 45.	Typical Cross-Sectional Profiles of a Cu Line at Different Stages of Thermal Cycling from Ambient to 723K. The Width of the Cu Line is Observed to Decrease with Increasing Number of Thermal Cycles. ....	89
Figure 46.	Histograms of the Width Distribution of Cu Lines at a Distance of 20nm from the Interface Prior to Thermal Cycling, and Following 1, 3 and 5 Thermal Cycles. The Means and Standard Deviations of the Distributions are as Follows : (a) Before : 1429 $\pm$ 15 nm, (b) 1 Cycle : 1382 $\pm$ 21nm, (c) 3 Cycles: 1317 $\pm$ 16nm, and (d) 5 Cycles : 1296 $\pm$ 13nm.....	90
Figure 47.	Changes in Cu Line Width and Line Thickness Plotted as a Function of the Number of Thermal Cycles. ....	91
Figure 48.	(a) Distribution of In-Plane Normal Stress ( $\sigma_{xx}$ ) Along Film-Width for an Al Film on Si at Ambient Temperature, Following Cooling from Annealing Temperature. (b) Distribution of Interfacial Shear ( $\tau_i$ ) and Normal ( $\sigma_{i,yy}$ ) Stresses Along Film-Width for the Same Conditions. The Dashed Lines Refer to $\tau_i$ , While the Solid Lines Refer to $\sigma_{i,yy}$ . All the Stress Distributions are Shown for Varying $t_f/l_f$ Values. The Abcissa Represents Distance x Along the Film-Width, Normalized by Half the Film Width $l_f/2$ . [6].....	93

Figure 49.	Computed Variation of $\sigma_{xx}$ and the Von-Mises Effective Plastic and Creep Strains in an Al Film During Thermal Cycling. [6] .....	94
Figure 50.	The Distribution of In-Plane Plastic and Creep Strains Near the Edge of the Al Film at the End of the Heating Segment (623K) and at the End of the Thermal Cycle (300K). The Displacement Scaling Has Been Exaggerated to Reveal Changes in the Edge Profile Associated with Cycling. The Middle of the Film Lies Far Away (Beyond the Picture) Towards the Left. All the Contour Plots have the Same Scaling, and the Observed Differences in Size and Location in the x-Direction Between the Two Temperatures are Representative of Reality. [6] .....	95
Figure 51.	Computed Profiles of the Right Edge of the Al Film at Different Temperatures during Heating and Cooling. The Horizontal Line at the Top of Each Edge-Profile Has Been Drawn in to Delineate the Film Edge Clearly, and Do Not Represent the Actual Data.[6].....	97
Figure 52.	Distribution of Interfacial Shear stress $\tau_i$ Close the Edge of Al Film at Different Temperatures during Thermal Cycling. [6].....	97
Figure 53.	Computed Variation of $\sigma_{xx}$ and the Von-Mises Effective Plastic and Creep Strains in an Cu Film on Si during Thermal Cycling. [6] .....	98
Figure 54.	The Distribution of In-Plane Plastic and Creep Strains Near the Edge of the Cu Film at the End of the Heating Segment (723K) and at the End of the Thermal Cycle (300K). The Displacement Scaling Has Been Exaggerated to Reveal Changes in the Edge Profile Associated with Cycling. The Middle of the Film Lies Far Away (Beyond the Picture) Towards the Left. All the Contour Plots Have the Same Scaling, and the Observed Differences in Size and Location in the x-Direction Between the Two Temperatures are Representative of Reality. [6] .....	99
Figure 55.	Computed Profiles of the Right Edge of the Cu Film at Different Temperatures During Heating and Cooling. The Horizontal Line at the Top of Each Edge-Profile Has Been Drawn in to Delineate the Film Edge Clearly, and Do Not Represent the Actual Data. [6].....	101
Figure 56.	Distribution of Interfacial Shear Stress $\tau_i$ Close the Edge of Cu Film at Different Temperatures During Thermal Cycling. [6].....	101
Figure 57.	AFM Image of the CMPed Surface of a Single Level Interconnect Structure on a Si Device, Consisting of Parallel Cu Lines of Alternating Widths of 1.8 and 0.2 $\mu$ m, Separated by a Low-K Dielectric (LKD). .....	110
Figure 58.	Surface Profiles Showing Changes in Interfacial Step Height Between Cu and LKD During Thermal Cycling Over 293-723K. ....	110
Figure 59.	Change in Interfacial Step Height vs. Probability for 1.8, 0.8 and 0.2 $\mu$ m Wide Cu Lines Following Thermal Cycling from 298K to 723K. ....	110



Figure 60.	Model Showing Elastic Stresses Due to Differences Between CTE of Cu, LKD, and Si. Thick Cu lines Undergo OOP and IP Deformation (a) While Thin Cu Undergo Only OOP Deformation. ....	111
Figure 61.	Cu Line Edge Profile Before and After 5 Thermal Cycles from 298K to 723K in Vacuum. ....	112
Figure 62.	In-Situ Surface AFM Profiles for Sample B for 0.2 $\mu$ m and 0.8 $\mu$ m Cu Lines at 298, 348 and 398K. ....	114
Figure 63.	(a) AFM Image Showing Cross-Section of Cu/LKD Structure on Si. (b) Perimeter of a 0.4 $\mu$ m Wide Cu Line at Different tages of Thermal Cycling from 298K to 398K. ....	116

## LIST OF TABLES

Table 1.	Physical Properties of Al and Si Relevant to Diffusion Bonding .....	22
Table 2.	Composition of Al Used for Diffusion Bonding.....	23
Table 3.	Cleaning Sequence for Surfaces of Si and Al Prior to Diffusion Bonding.....	25
Table 4.	Diffusion Bonding Conditions for Various Experimental Setups.....	30

THIS PAGE INTENTIONALLY LEFT BLANK

## ACKNOWLEDGMENTS

*“All things were made through Him, and without Him nothing was made that was made.” John 1:3*

First and foremost I would like to thank our God for allowing me to have the privilege to further my understanding in what he perfectly made. Endless amount of gratitude and love to my cherished wife, Domonique, for always listening to my frustrations, giving me undo encouragement, and always knowing what I needed. Great thanks goes to my son for giving up the traditional father-son activities in exchange for running endless amount of experiments with me.

I would like to sincerely thank my advisor, Professor Indranath Dutta, for his guidance and always pushing me to achieve more than I thought I could. I would also like to extend my appreciation to my dissertation committee for listening and guiding my ideas throughout my research. A great indebtedness goes to Dr. Mingwei Chen for his contribution of atomic force microscopy work and numerous hours of high-resolution microscopy to this project.

I am grateful to the Mechanical Engineering model makers, Jim Lefler and Frank Franzen, for their hard and tedious work that enabled my ideas to transform into superb experimental equipment. I would like to extend my gratitude to all the technicians that continuously helped me with various laboratory setups and repairs: Don Synder, Bob Sanders, Chanman Parks, Mardo Blanco, Nancy Carroll, and Tom Christian. Many thanks go to the library staff for their endless efforts to find references in articles, books, and web sites.

I am grateful for the undergraduate and high school interns that worked on the project under the Naval Postgraduate School and Monterey Academy of Oceanography Science: Jesse Sherburn, Phil Han, Billy McCoy, Aric Kwon, Alex Buell, and Adam Brown.

Lastly, I would like to thank the National Science Foundation and Space Warfare Systems Center for their support.

THIS PAGE INTENTIONALLY LEFT BLANK

# I. INTRODUCTION

Technological advances to increase the performance and reliability of structures bring about multiplicity of materials and miniaturization, which increases the number of interfaces in a given volume. Therefore, the mechanical behavior of interfaces plays a key role in the overall performance of the structure. In multicomponent structures, shear stresses frequently arise during thermomechanical excursions due to differential expansion/contraction between the different components. At elevated temperatures, interfaces can undergo diffusionally accommodated sliding (interfacial creep) to relieve the thermal stresses, usually resulting in dimensional changes, which affect the overall reliability and performance of the system. In this dissertation, a methodology for measuring interfacial sliding in engineering systems is developed to study the mechanism and kinetics of interfacial creep, and the impact of this phenomenon on thin film-substrate systems applicable to microelectronics is investigated.

The mechanical properties of interfaces between dissimilar materials at elevated temperatures are critical to the performance of a wide range of engineering systems such as those found in metal and ceramic-matrix composites, microelectronic devices and packages, various film-substrate systems and multi-phase alloys. In many such applications, large shear stresses develop at interfaces during thermo-mechanical excursions when the difference in coefficient of thermal expansions (CTE) is large, and one of the materials adjacent to the interface is subjected to a high homologous temperature ( $T/T_m$ ). This enables diffusionally accommodated sliding processes (interfacial creep) to occur at the interface [1-13]. Such processes may severely impact the dimensional stability (e.g., in composites) or reliability (e.g., in microelectronics) of the materials system or component of interest.

Interfacial creep, which is the subject of this thesis, is distinct from columbic interfacial sliding in that no interfacial fracture (or debonding) occurs in the former. The materials adjoining the interface slide relative to each other by diffusional mass transport under the influence of local stress gradients along the interface which arise under the influence of a far-field applied shear stress. As such, the process is akin to grain

boundary sliding by diffusional mechanisms. Contrarily, a prerequisite to columbic interfacial sliding is interface fracture (or delamination), which is followed by frictional sliding at the interface, which results in a relative displacement between the adjacent materials.

The phenomenon of interfacial creep has been observed in systems such as continuous fiber composites [1-5], thin film/substrate systems [8-10], and microelectronic devices [11-13]. Measuring the kinetics of interfacial creep in isolation from other superimposed time-dependent processes (such as creep of one of the components) in materials systems is very difficult. Complications arise because: (1) sliding often occurs near the extremities of one of the phases (e.g., the ends of a fiber within a matrix or the edges of a film on a substrate); and (2) the shear stresses which drive interfacial sliding vary dramatically with position along the interface, making the interpretation of sliding data difficult. Examples of interfacial creep in microelectronics, particulate composites, and metal-matrix composites along with their proposed mechanisms are further discussed in Chapter II.

Funn and Dutta [3] designed experiments and analytical approaches, to study the kinetics of interfacial creep in isolation from other superimposed phenomena, and measured the kinetics of interfacial sliding in Pb-Ni and Pb-SiO<sub>2</sub> single fiber composites. An interface-sliding model was proposed using a diffusion creep law with a threshold stress and an activation energy corresponding to interfacial diffusion. However, Funn and Dutta were unable to experimentally verify the dependence of sliding kinetics on interfacial normal stress and roughness using single fiber composites, because in their approach the interfacial normal stress resulted from thermal stresses, which varied with the test temperature, and the interfacial roughness (i.e., fiber surface roughness) was not controllable.

This dissertation (1) develops a well-controlled experimental approach to systematically study interfacial creep in bulk systems; (2) develops a mechanistic understanding of the phenomenon of interfacial creep by correlating the sliding kinetics with interfacial structure and stress states; (3) generate kinetics data for Si-Al system, which is of practical importance in many microelectronics and micro-electromechanical

systems (MEMs) applications; and (4) measures the impact of interfacial creep on the performance and reliability of thin film interconnect systems using atomic force microscopy (AFM).

First, in order to study the intrinsic interfacial properties in isolation from the overall system behavior, a model system with a well-controlled interface was required. The Si-Al system offered numerous advantages to study interfacial sliding: (1) a limited solubility, which allowed a sharp and well-bonded interface to be fabricated; (2) an elastic body (Si) adjoined to an elastic, plastic, and creeping body (Al), which allows interfacial creep to be isolated from extraneous effects; (3) a low melting temperature for Al, which allows creep testing to be performed at reasonable temperatures and at high homologous temperatures; and (4) a common semiconductor-metal interface which has many applications in the microelectronic industry. Hence, a diffusion-bonding procedure was developed to produce Al/Si/Al sandwich specimens enabling a double-shear geometry to be used during interfacial creep tests. **Chapter IV** explains the optimized conditions necessary to form strong diffusion bonds at Al/Si interfaces and analyzes the impact of process parameters on the morphology, structure, and chemistry of the interface prior to creep testing.

Second, a mechanical testing methodology was developed to isolate the interfacial creep properties from the overall mechanical behavior of the system. The design of the specimen stage enabled simultaneously normal and shear loading of the interface. The ability to independently load the interface in shear, as well as normally, facilitated: (1) the study of the role of interfacial normal stress in diffusional creep, e.g., threshold behavior in compression and (2) the study of the dependence of the operative sliding mechanism on the ratio of shear to normal stresses to investigate any mechanistic changes. The surface roughness of the specimens were also varied prior to diffusion bonding, enabling the interfacial creep rate and the threshold behavior dependence on interfacial roughness to be thoroughly investigated. **Chapter V** comprehensively explains the interfacial creep kinetics and mechanism.

Third, **Chapter VI** shows the impact of interface sliding on the performance and reliability of thin film systems using atomic force microscopy (AFM) measurements of



both lateral and out-of-plane dimensions of stand-alone Cu lines on Si and Cu/LKD structures on Si, with the intent of delineating the role of interfacial sliding during thermal cycling of devices during processing and service. Some preliminary observations of deformation of back-end structures due to global package-level loads were also examined.

## II. BACKGROUND

### A. EXAMPLES OF INTERFACIAL SLIDING IN ENGINEERING SYSTEMS

#### 1. Microelectronics

Interfacial sliding by diffusional mechanisms has been noted in copper/polyimide high density interconnects (HDIC) on silicon during thermal cycling [11, 12]. Here, parallel Cu interconnect lines separated by polyimide (PI) dielectrics are deposited on the Si device, with tantalum as a diffusion barrier at the Si-PI, Si-Cu and Cu-PI interfaces. A single-layer structure based on Cu/PI HDICs is schematically shown in Figure 1a. For multi-level Cu/PI HDIC structures, successive metal-dielectric layers are deposited on top of each other [14]. During the processing steps involved in forming each layer (imidization and Cu deposition), the structure is heated to 350°C ( $\sim 0.45T_m$  for Cu), thereby subjecting the entire package to a thermal cycle.

Evaluation of the impact of one such thermal cycle by atomic force microscopy (AFM) of the surface of a single HDIC layer has revealed that sliding along the vertical Cu-Ta interfaces results in a significant change in the relative heights of the PI and Cu lines following cycling [11, 12]. Figure 1b shows the relative height difference between the PI and Cu layers due to one thermal cycle. This has been attributed to diffusionally accommodated sliding driven by shear stresses generated by the large CTE mismatch ( $\Delta CTE$ ) between the PI, Ta and Cu layers in the out-of-plane direction, and has been identified as a potentially significant reliability issue.

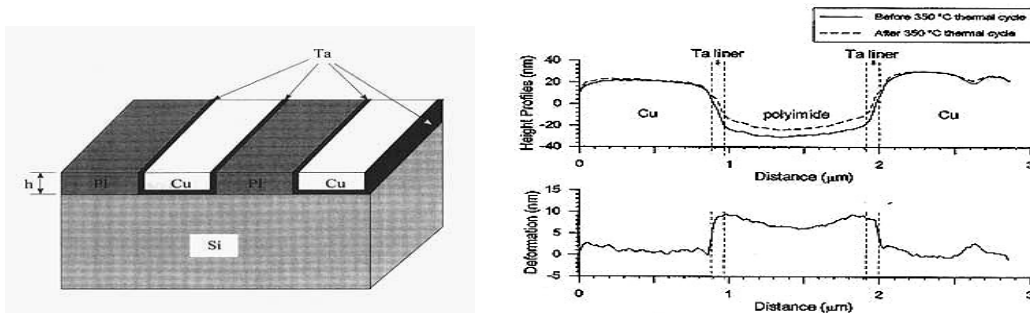


Figure 1. (a) Schematic of Cu/PI HDIC on Si with Ta Interlayers. (b) Surface Profile Before and After Thermal Cycling, and Plot Showing Differential Deformation of Cu and PI via Sliding at Cu/Ta Interface [11].

Sliding may also occur in the in-plane (horizontal) direction, especially when the metallization is not laterally constrained. For instance, the substantial  $\Delta\text{CTE}$  between metal and Si ( $\sim 21 \times 10^{-6}/\text{K}$  and  $14 \times 10^{-6}/\text{K}$  for Al-Si and Cu-Si, respectively) results in very large in-plane stresses in thin film interconnects. Additionally, during device operation, temperatures due to Joule heating may reach  $150^\circ\text{C}$  ( $\sim 0.45T_m$  for Al and 0.32 for Cu). Together, the high stress and temperature can activate creep mechanisms in the metallic film. For example, Cu films on Si may creep at temperatures as low as  $60^\circ\text{C}$  during thermal cycling [15], whereas Al films on  $\text{Al}_2\text{O}_3$  can start creeping at even lower temperatures [16]. Near the edges of the film, creep relaxation of the film can be accommodated by interfacial sliding due to the presence of interfacial shear stresses, thereby allowing the film-dimensions to change. Typically, interfacial shear stresses are confined to a distance of 1-2 film-thicknesses from the film-edges [17-20], and their effect may be ignored for large films. However, for narrow films (e.g., interconnect lines), edge-effects can become significant. For example, for a  $0.5\mu\text{m}$  thick,  $1\mu\text{m}$  wide interconnect line, interfacial shear stresses would prevail over the entire line width (shown schematically in Figure 2), making sliding a potentially important issue. The importance of sliding is likely to increase as devices become more highly integrated and their operating temperatures increase.

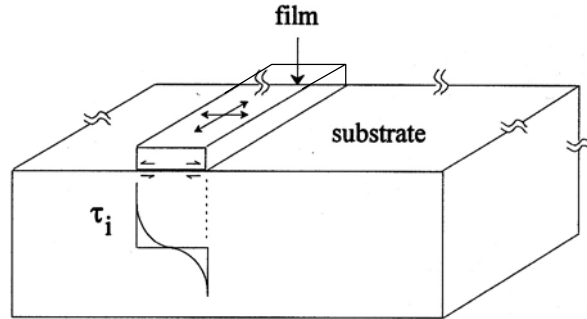


Figure 2. Schematic of Interfacial Shear Stress Distribution along the Width of a Narrow Thin-Film Line. The Film is in In-Plane Biaxial Tension.

Another area where interfacial sliding may play an important role in microelectronics is in C4 solder joints in flip-chip packaging, where a Si device is attached directly to a ceramic or organic substrate via an area array of solder-bumps. During device operation, the solder-bumps near the edges of the chip are subjected to large shear strains due to the  $\Delta\text{CTE}$  between chip and substrate ( $2.3 \times 10^{-6}/\text{K}$  for Si and  $18 \times 10^{-6}/\text{K}$  for FR-4 organic). The situation is aggravated by thermal cycling conditions with temperatures reaching  $\sim 0.75T_m$  for the solder, leading to well-known reliability problems in C4 [21, 22]. In addition to creep and low-cycle fatigue of the solder, the combination of high temperature and shear stresses at the solder-Si and solder-substrate interfaces is likely to cause interfacial sliding, though this effect is usually masked by other superposing processes. As solder-bump sizes decrease and devices run hotter, however, sliding may become performance-limiting, particularly when interfacial diffusivities are high.

## **2. Superplasticity of Particulate Composites**

It has been suggested that the rate controlling mechanism for high strain rate superplasticity in ceramic particulate-reinforced metal-matrix composites is interfacial sliding [23-25]. The proposed mechanism and the role of interfacial sliding are illustrated in Figure 3 for a composite with a particulate size on the order of the matrix grain size. Here, grain boundary sliding between grains A and B is thought to be accommodated by diffusionally accommodated sliding at the metal-ceramic interface. The high activation energy measured for superplasticity ( $\sim 293\text{-}338$  kJ/mol for various ceramic particulate reinforced Al composites) has been attributed to diffusion along the particle-matrix interface [25], based on the treatment of interface reaction-controlled diffusional creep by Arzt et al. [26]. The importance of interfacial sliding is elucidated by the observed inverse reinforcement size-dependence of the superplastic strain rate [25], since a reduction of particulate size causes an increase in the total area available for interfacial sliding.

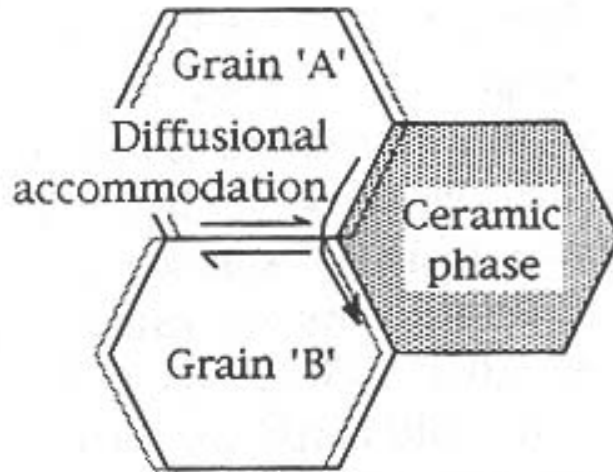


Figure 3. In Superplasticity of Particulate Composites, Sliding between Matrix Grains is Accommodated by Diffusional Sliding at Particle-Matrix Interfaces [25].

### 3. Metal-Matrix Composites

Although axially loaded continuous fiber reinforced composites are generally thought to deform with the matrix and fiber in isostrain condition, there is ample evidence in the literature that this condition is often violated, even in the absence of interfacial fracture. This is most clearly observed following thermal cycling of composites in the absence of any applied load [1, 2, 5]. For instance, Yoda et al. [1] observed that the ends of W fibers in a Cu matrix intruded dramatically into the matrix following thermal cycling, the extent of intrusion increasing with increasing number of cycles (Figure 4). Similar effects have been observed following slow thermal cycling of graphite fiber reinforced aluminum composites [2, 5], whereupon the matrix was observed to protrude past the fiber ends. In both cases, the slow heating / cooling rates during cycling, in conjunction with the tensile matrix thermal stress along the fiber-axes, allowed the matrix to elongate relative to the fibers via creep. Here, no interfacial debonding occurs, and the differential strain between the matrix and fibers is accommodated by time-dependent diffusional sliding at the interface close to fiber-ends, where large interfacial shear stresses exist due to differential thermal expansion/contraction of the matrix and fiber.

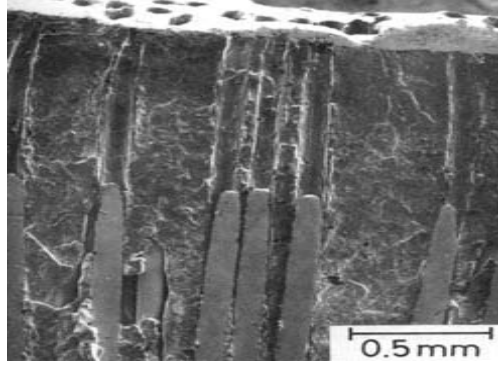


Figure 4. Cu-Matrix Protruding Beyond the Ends of W-Fibers after Thermal Cycling [1]

It should be realized that the above-mentioned effect is very different from that observed during relatively rapid thermal cycling, where interfacial fracture, followed by frictional sliding at the debonded interface, results in the relief of axial tensile residual stresses in the matrix, allowing the matrix to shrink relative to the fibers [27, 28]. Frictional sliding is commonly observed in composites with weak interfaces, which undergo debonding during cycling [27-29], whereas time-dependent sliding via interfacial creep occurs in the absence of debonding.

Evidence of interfacial creep has also been noted during isothermal creep of discontinuous  $\text{Ti}_2\text{AlC}$  platelet reinforced  $\gamma\text{-TiAl}$ -matrix composites, where, beyond about 60 percent of the melting temperature, the composite creep strength was observed to decrease below that of the unreinforced matrix, despite the absence of any interfacial debonding or fracture [30]. This loss of strength at high temperatures has been attributed to diffusional relaxation of the matrix, accommodated by diffusionally accommodated sliding at the interface [31].

The effect of interfacial sliding on axial tensile creep during thermal cycling was investigated [4] using specially designed Pb matrix - Ni fiber SFC samples (Figure 5a). The sample design allowed (1) the axial fiber and matrix strains to be measured separately, and (2) interfacial shear stresses (and therefore interfacial sliding) to prevail within the gauge length. It was demonstrated that the fiber and matrix strained differently during tensile creep testing (Figure 5b), the differential strain being accommodated by interface creep at the extremities of the gauge length.

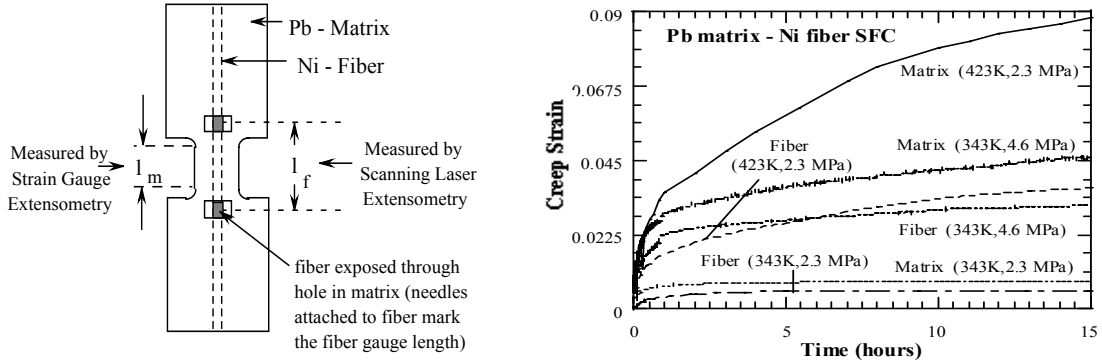


Figure 5. (a) Sample Utilized to Separately Measure Matrix and Fiber Strains during Uniaxial Creep Tests. (b) Differential Matrix and Fiber Strain Response during Creep Indicates Interfacial Sliding [4].

A micro-mechanical model for axial creep, incorporating the effect of interfacial sliding, was also developed [4]. The results showed that during creep testing, sliding is typically confined to the ends of the tensile sample within the grip section, allowing the isostrain condition to be maintained over the tested gauge length. In this case, the composite creep rate decreases continuously and eventually vanishes as the applied load is progressively transferred from the matrix to the fibers. However, for large fiber diameters and short specimen lengths, sliding may occur within the gauge length, resulting in a violation of the isostrain condition. This allows the composite to creep at a finite rate even after long creep times, as seen in Figure 5b. These effects are of particular importance during deformation in the absence of end constraints, e.g., in axial creep of turbine blades, as well as during thermal cycling and flexural creep.

The role of interfacial sliding on the thermal cycling response of continuous fiber composites was also studied [5]. Experiments based on graphite-aluminum composites revealed that the fiber-ends may either protrude or intrude relative to the matrix following slow thermal cycling (Figures 6a and 6b). The strain response during cycling was analytically modeled, accounting for the effects of (1) interfacial creep and (2) matrix creep mechanism transitions due to changing temperature and internal stress state. The

model captured all the important features of the experimental strain response, and showed that both intrusion and protrusion can be accounted for by diffusional-accommodated interfacial sliding near the extremities of the composite sample. It also showed that the operative matrix creep mechanism changes continually during cycling, and is strongly dependent on the heating or cooling rate. Based on the analysis, a transient deformation mechanism map for thermal excursions was constructed. Such maps are plotted with the heating/cooling rate ( $dT/dt$ ) and homologous temperature ( $T/T_m$ ) as the ordinate and abscissa, respectively, and contain contours of constant modulus-compensated matrix stress ( $\sigma_m/G_m$ ) and constant total composite strain ( $\epsilon$ ), and identify regions corresponding to the various matrix deformation mechanisms and interfacial sliding. Interfacial sliding was found to occur at temperatures above  $\sim 0.4T_m$ , with the cumulative differential strain between the matrix and fiber increasing at a decreasing rate with increasing number of cycles.

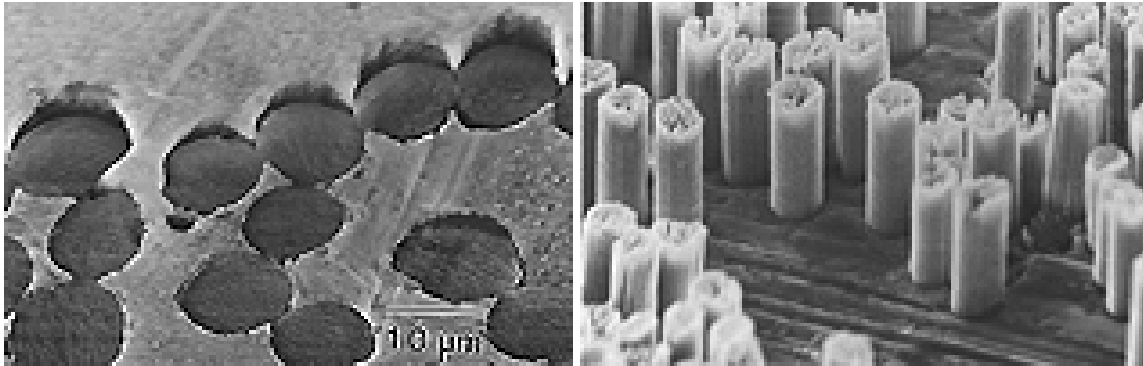


Figure 6. Intrusion and Protrusion of Graphite Fiber-Ends Relative to an Al-Matrix Following Slow Thermal Cycling from 298K to 380K and 600K, Respectively [5].

Five points emerge from the preceding discussion. First, although evidence of interfacial sliding is apparent in many systems, there is no general agreement on its mechanism. Secondly, it is likely that the mechanism of sliding changes depending on the prevailing shear stress-temperature conditions, adding to the confusion. Thirdly, the interfacial diffusivity and the mechanism of sliding probably depend strongly on the



nature (i.e., structure and chemistry) of the interface in the system of interest, further complicating the situation. Fourthly, in order to systematically study interfacial sliding, mechanical tests are needed to isolate the interfacial behavior from the rest of the system and to preclude complicated stress states at the interface. Finally, although interfacial sliding has often been invoked to rationalize the strain response of different materials, very few systematic studies on the impact of interfacial sliding on the behavior of complete materials systems have been reported to date. Clearly, all these issues become particularly important when the sliding kinetics are rapid (e.g., for low  $Q_i$ ), making interfacial sliding a potentially performance-limiting phenomenon.

## **B. POSSIBLE MECHANISMS OF INTERFACIAL SLIDING**

The effect of interfacial creep is often difficult to recognize because of other concurrent and superposed phenomena. Indirect evidence of diffusionally accommodated interfacial sliding during creep/superplastic deformation has been obtained in many systems, including dispersion strengthened metals (e.g., [26, 33-35]), eutectic alloys [36, 37], intermetallics [38], various metal and ceramic-matrix composites [39-42], and film–substrate interfaces [13]. The inferred kinetics of interfacial sliding in these systems varies considerably. In most systems, interface sliding controlled creep results in a stress exponent ( $n$ ) ranging from 1 to 2 [e.g., 3, 13, 23-26, 38], often shows a temperature dependent threshold stress below which creep does not occur [3, 33, 35], and displays an activation energy which is typically well over that for matrix volume diffusion  $Q_{vol}$  [e.g., 23-26, 34], but is sometimes below  $Q_{vol}$  [3, 13, 36-38]. These discrepancies arise because the kinetics of interface sliding was inferred from the overall strain response of the entire materials system. In none of them, the interfacial sliding response was explicitly studied by isolating it from concurrent and superposing effects.

However, the phenomenon of interface sliding has been directly observed in systems such as continuous fiber composites [1-5], thin film/substrate systems [8-10], and microelectronic devices [11-13]. In these cases, the kinetics of interfacial creep was not independently measured in isolation from other superimposed time-dependent processes (such as creep of one of the components) in the materials systems. Complications arose

because the sliding often occurred near the extremities of one of the phases (e.g., the ends of a fiber within a matrix or the edges of a film on a substrate) and the shear stresses which drove interfacial sliding varied dramatically with position along the interface, making the interpretation of sliding data difficult.

The above-mentioned approaches have thought of interfacial creep in a number of different ways. First, grain boundary/interface sliding may be thought to occur by *diffusional creep* [32]. When the interface acts as a perfect source and sink of vacancies due to an abundance of mobile boundary dislocations (BDs),  $n$  equals 1 and  $Q$  equals that for either boundary or lattice diffusion [26, 32]. When the density or mobility of dislocations in the boundary is limited, however, the kinetics of sliding are believed to become "interface reaction-controlled", resulting in  $n \sim 2$ , a threshold stress corresponding to the minimum stress required to move BDs, and a high activation energy associated with rearranging atoms on the more refractory/stiffer side of the interface [26, 33, 43]. This type of representation has been used to describe sliding along phase boundaries in eutectic alloys [36], film-substrate interfaces [11, 12, 13], and particle-matrix interfaces [23-25].

Second, in fibrous metallic composites, the interface has been thought of as a highly dislocated region of the matrix (a work hardened zone), formed due to the difference in stiffness between the fibers and matrix, which makes matrix dislocation loops moving towards the fiber stand off at some equilibrium distance from the fiber [67-69]. This is followed by recovery processes driven either by dislocation annihilation processes in the work hardened zone [44], or by the non-conservative glide of prismatic loops along the interface [45, 46]. Both allow the interface to accommodate differential strain rates between the matrix and fiber, and results in a *power-law creeping interfacial region*, which has been the basis for a number of models of composite creep proposed in the literature [44-48].

Third, the interface is considered to be able to deform via two independent but related mechanisms [49-51]. First, the interface is thought to slide in shear with a linear rheology, e.g., by diffusional shear-creep of an interphase layer. Secondly, mass transport by interfacial diffusion driven by gradients in the normal or hydrostatic stress state along

the interface is also considered possible. Analysis based on short fiber metallic composites has shown that both mechanisms (*viscous drag and diffusional flow*) have the same linear stress dependence and the same direction of net mass flow [49].

Fourth, interfacial sliding along  $\gamma/\alpha_2$  phase boundaries in TiAl has been thought to occur by *cooperative glide of intrinsic interface dislocations* (ID) in the low stress-intermediate temperature regime [38]. The glide rate was postulated to be limited by climb of sessile jogs and/or solute drag from interstitial impurities on the interface plane, giving rise to a thermally activated sliding process with  $n \approx 1$ . Transmission electron microscopy (TEM) revealed IDs, although no evidence of intrinsic jogs or solute interactions with IDs was apparent.

Fifth interfacial sliding occurs due to interaction between IDs and lattice dislocations (LD) in one of the phases, resulting in a *dislocation slip controlled sliding* process with  $n$  approaching infinity [13]. The mechanism is similar to the second treatment outlined above, except that the proposed rate-controlling mechanism in this case is conservative glide, rather than non-conservative motion, of interface dislocations. This type of deformation has been noted at the interface between a brittle film and a ductile substrate deformed under high strain rate conditions [13]. Glide of lattice dislocations in a thin, localized shear band parallel to the interface has also been noted in layered metal-ceramic systems subjected to compressive loading normal to the interface [52].

Based on periodic film-cracking experiments (where a brittle film on a ductile substrate under monotonic loading develops cracks with a spacing dependent on the extent of interfacial sliding) it has been suggested that at high strain rates / low temperatures, sliding occurs by glide-controlled processes (either of IDs or LDs), whereas at low strain rates / high temperatures, it occurs by diffusional flow [13]. It was also suggested that interfacial sliding is unlikely to display power-law kinetics (climb-control), since this is usually associated with sub-grain formation, and sliding is generally confined to a region much narrower than typical subgrain sizes. However, as indicated above, at least some of the existing descriptions of interfacial sliding are based on a

power-law formulation [e.g., 44, 48, 49]. Clearly, significant confusion exists regarding the mechanism of interfacial sliding.

In addition to the divergence of opinion on the mechanism of interfacial sliding, there is significant confusion about the measured activation energy for interfacial creep. For sliding via climb of lattice dislocations near the interface [e.g., 44-46], the activation energy ( $Q$ ) is thought to equal  $Q_{vol}$  for one of the phases. Even when the proposed mechanism necessitates interfacial diffusion,  $Q$  values ranging from well over  $Q_{vol}$  to well below  $Q_{gb}$  have been noted. For instance, the activation energy for interfacial diffusion ( $Q_i$ ) has been observed to be greater than the matrix  $Q_{vol}$  in a number of particulate composites [23-25]. On the other hand,  $Q_i$  values analytically derived from composite creep data [53] were found to lie between  $Q_{vol}$  and  $Q_{gb}$ . Contrarily,  $Q_i$  values determined for sliding at a  $SiO_2$  film-Cu substrate interface based on the periodic film cracking technique [13] were substantially lower than  $Q_{gb}$  for Cu, and nearly a fourth of the  $Q$  for diffusion along Cu- $SiO_2$  interfaces in dispersion strengthened Cu [54]. Studies of sliding at  $\gamma/\alpha_2$  phase boundaries in lamellar TiAl also displayed low  $Q$  [38]. A low value of  $Q$  for interfacial diffusion is also consistent with kinetic measurements of interfacial sliding made by Funn and Dutta in Pb-matrix SFCs [3].

Various studies of interface diffusion in multi-phase alloys (e.g., Ag-Fe, Ag-Ni, Ag-Sn, Zr-Nb, Sn-Ge [55-57]) have shown that interfacial diffusivity is, in general: (1) more rapid compared to lattice diffusion in either of the adjoining phases, and (2) dependent on the orientation relationship between the two phases. A recent study of diffusion in a eutectic Pb-Sn alloy showed that  $Q_i$  (up to  $\sim 400K$ ) lies between  $Q_{vol}$  and  $Q_{gb}$  for Pb [37]. Above 400K, however, it becomes close to  $Q_{gb}$ , commensurate with an abrupt increase in the interfacial energy  $\gamma$ , which coincides with loss of coherency of the interface between Pb-rich and Sn-rich phases.

In the above studies, the methodology used to infer interfacial creep kinetics has consisted of either (1) measuring the overall strain response of the system and deducing the interfacial sliding kinetics, assuming it to be the rate controlling mechanism [e.g., 13, 23-25, 34-36]; or (2) assuming an interfacial flow law, followed by modeling the

behavior of the entire system using the law, and then comparing the analytical results with experiments [31, 44, 48-51]. However, because of the complex nature of many of the systems studied *vis-a-vis* (1) the large spatial variation of interfacial shear stresses, (2) the chemistry/structure of the interfacial region, and (3) the superposition of multiple deformation events (e.g., creep of matrix and interface in a composite, or film and interface in a film/substrate system), the phenomenology of interfacial creep is difficult to ascertain using the above methodologies.

In order to circumvent these difficulties, Funn and Dutta [3] designed experiments and analytical approaches, to study the kinetics of interfacial creep in isolation from other superimposed phenomena, and measured the kinetics of interfacial sliding in Pb-Ni and Pb-SiO<sub>2</sub> single fiber composites. An interface-sliding model was proposed using a diffusional creep law with a threshold stress and an activation energy corresponding to interfacial diffusion.

### C. DIRECT MEASUREMENT OF INTERFACIAL CREEP KINETICS

In previous work [3], the kinetics of interfacial sliding were directly measured at fiber-matrix interfaces and described by a flow law with  $n=1$  and a threshold stress (Bingham flow). The studies were based on two model SFC systems - one with limited mutual solubility (Pb-matrix/Ni fiber) and the other with no mutual solubility (Pb-matrix/quartz fiber). Both systems displayed a low  $Q$  value ( $Q < Q_{gb}$  for Pb) and a stress exponent of 1, based on which, the mechanism of sliding was thought to be interface diffusion-controlled diffusional creep. The low  $Q$  value, along with the small-applied shear stresses, precluded a dislocation climb based rationalization of the observed sliding. Further, scanning electron microscopy (SEM) of the interface revealed a periodic topography, consistent with the notion of local normal stress variation along the interface due to a globally applied shear stress, as considered in the classical model for grain boundary sliding [32]. The classical model was modified to incorporate a global normal stress (in addition to the applied shear) in order to account for the effect of radial stresses which arise from CTE / Poisson's ratio mismatch between the fiber and matrix, and it was shown that the kinetics of sliding may be represented as:

$$\dot{\gamma}_i = \frac{2D_m^{\text{eff}}\Omega\lambda}{kT\pi h^3} \left[ \tau_i + \left( \frac{\pi h}{\lambda} \right)^3 \sigma_R \right] + \frac{4\delta_i D_i \Omega}{kTh^3} \left[ \tau_i + 2 \left( \frac{\pi h}{\lambda} \right)^3 \sigma_R \right] \quad (2.1)$$

where  $\tau_i$  is the shear stress acting on the interface,  $D_m^{\text{eff}}$  and  $D_i$  are the effective matrix and interface diffusivities, respectively,  $\Omega$  is the atomic volume of the diffusing species (matrix),  $\delta_i$  is the thickness of the interface,  $\lambda$  and  $h$  are the periodicity and width (i.e., twice the amplitude), respectively, of the interface, and  $\sigma_R$  is the normal (radial) stress acting on the interface. When  $D_m^{\text{eff}} \gg D_i$ , the first term in Equation 2.1 is negligible, and  $\dot{\gamma}_i$  can be simplified as:

$$\dot{\gamma}_i \approx A_i (\tau_i + \tau_o) \quad (2.2)$$

Here  $\tau_o$ , the contribution of the interfacial normal stress to sliding, is given by

$$\tau_o = 2\pi^3 \left( \frac{h}{\lambda} \right)^3 \sigma_R \quad (2.3)$$

and

$$A_i = \frac{4\delta_i D_{i0} \Omega \lambda}{kTh^3} \exp \left[ -\frac{Q_i}{RT} \right] \quad (2.4)$$

where  $Q_i$  and  $D_{i0}$  are the activation energy and frequency factor, respectively, for interfacial diffusion,  $k$  is Boltzmann's constant,  $R$  is the gas constant, and  $T$  is the absolute temperature.

In Equation 2.1, a compressive  $\sigma_R$  would result in a negative  $\tau_o$  and hence result in a threshold behavior, whereas a tensile  $\sigma_R$  would increase the effective shear stress at the interface, and hence enhance the sliding rate. Equation 2.3 suggests that the temperature dependence of  $\tau_o$  arises from the strong temperature dependence of the radial thermal residual stresses. It is also apparent from Equation 2.1 that diffusional creep would result in significant sliding rates only when  $h$  is small (i.e., when the interface is smooth, as for the cold-drawn Ni and fused quartz fibers used in this study). For composites containing fibers with rough surfaces (e.g., those produced via CVD), sliding by diffusional creep will be minimal, unless  $Q_i$  is very low.

The above results are significant because they provide an alternate rationalization of threshold behavior during diffusional flow (besides interface reaction-control [26]), and may be useful in understanding creep in multi-phase systems with internal stresses. For instance, many dispersion strengthened systems where a threshold behavior has been observed during diffusional creep (e.g., in Au-Al<sub>2</sub>O<sub>3</sub> [33]) have a large CTE mismatch between the matrix and dispersion, thereby producing a strongly temperature-dependent radial compressive stress, which can result in a threshold behavior. Further, as shown in Reference 33, when the activation energies of interfacial and volume diffusion are comparable, the measured  $Q$  can be significantly higher than either, thereby rationalizing the anomalously large apparent  $Q$  noted in many systems. Thus, the above results suggest the means to rationalize some of the observations associated with diffusional creep in multi-phase systems based on a continuum approach, without invoking explanations based on discrete dislocation models of vacancy generation at the interface [26]. Clearly, however, additional work is necessary to establish whether the proposed mechanism is capable of capturing the principal characteristics of diffusional flow in complete systems.

### III. OBJECTIVES

The purpose of this dissertation is to develop a comprehensive mechanistic understanding of interfacial creep. This dissertation has three objectives: (1) to determine the kinetics and mechanism of diffusionally accommodated interfacial sliding in a multicomponent material system, using the Si/Al interface as a model system; (2) to correlate the mechanism with the structure and chemistry of the Si/Al interface; and (3) to evaluate the impact of interfacial sliding on the overall reliability of interconnect structures in microelectronic devices.

In order to satisfy these objectives, a sample geometry and test methodology to isolate the strain response of the interface from other concurrent effects is devised. **Chapter IV** explains the optimized conditions necessary to form strong diffusion bonds at Al/Si interfaces. **Chapter V** comprehensively explains the interfacial creep kinetics dependencies and its mechanism. **Chapter VI** shows the impact of interface sliding on the performance and reliability of thin film interconnect systems on Si based electronic devices.



THIS PAGE INTENTIONALLY LEFT BLANK

## IV. PROCESSING AND CHARACTERIZATION OF DIFFUSION BONDED Al-Si INTERFACES

*Submitted for publication to the Journal of Materials Processing Technology in August 2002 (co-authored with I. Dutta and M.W. Chen)*

### A. INTRODUCTION

Metal-semiconductor interfaces such as those between interconnect lines and ohmic contacts on substrates are critical to the reliability of microelectronic devices. Because of the differences in thermo-mechanical properties between metal and semiconductor interfaces, many of these interfaces present a reliability challenge [7, 8, 10]. As a result, there is substantial interest in studying the mechanical properties of these interfaces. In order to study the intrinsic interfacial properties in isolation from the overall system behavior, model systems with well-controlled interfaces are often utilized. In this chapter, we describe a diffusion-bonding procedure to produce well-controlled Al/Si interfaces. The resulting tri-layered sandwiches (Al-Si-Al) are being utilized to produce double-shear mechanical test specimens in order to investigate the kinetics of diffusionally accommodated interface sliding [3, 5, 58].

Diffusion bonding is frequently used to produce highly reliable interfaces between similar and dissimilar metals, alloys, and nonmetals. Temperature, pressure, and holding time are the three main variables, which govern the integrity of the diffusion bond. The bonding temperature is usually close to the melting point ( $0.7 - 0.9 T_m$ ) of the lower melting constituent. The bonding pressure is usually selected to allow local plastic flow of at least one component adjacent to the interface in order to enable filling of interfacial voids and to disperse surface oxide films. The holding time is usually kept to the minimum required to form a chemical bond across the interface without forming an excessively thick interdiffusion/reaction layer. Other important diffusion bonding parameters include vacuum level (i.e., environment), surface roughness, and surface chemistry. The objective of this chapter is to present the optimized conditions necessary to form strong, clean diffusion bonds at Al/Si interfaces and to analyze the impact of process parameters on the morphology, structure, and chemistry of the interface.

## B. EXPERIMENTAL PROCEDURE

### 1. Material Selection

Diffusion bonded samples were fabricated from pure (99.7+%) polycrystalline Al and 99.999+% pure single crystal Si, with the <100> direction pointing normal to the Si/Al interface. Some of the relevant properties of Al and Si are listed in Table 1 [59-61]. The chemical composition of the Al used in these experiments is given in Table 2. As shown in Figure 7, photomicrography of a polished specimen after etching for 60 seconds with a modified Keller's reagent shows a grain size on the order of 140 $\mu$ m - 150 $\mu$ m, which is typical for hot-rolled Al. A small volume fraction of insoluble FeAl<sub>3</sub> particulates, about 1 $\mu$ m in diameter, are observed dispersed throughout the alloy.

	Silicon	Aluminum [60, 61]
Melting Temperature (K)	1683	933
Crystal Structure	Diamond Cubic	Face Centered Cubic
Hardness (GPa) @ 298K	13 [102]	0.08
Yield Strength (MPa) @ 298K	--	34 5
@ 673K		~1.5
@ 847K		
Coefficient of Thermal Expansion ( $\times 10^{-6} \text{ K}^{-1}$ )	2.35	25.5

Table 1. Physical Properties of Al and Si Relevant to Diffusion Bonding.

Elements	Al	Fe	Si	Zn	Cu	Mg
(wt. pct.)	Bal.	0.20	0.04	0.02	0.01	0.01

Table 2. Composition of Al Used for Diffusion Bonding.

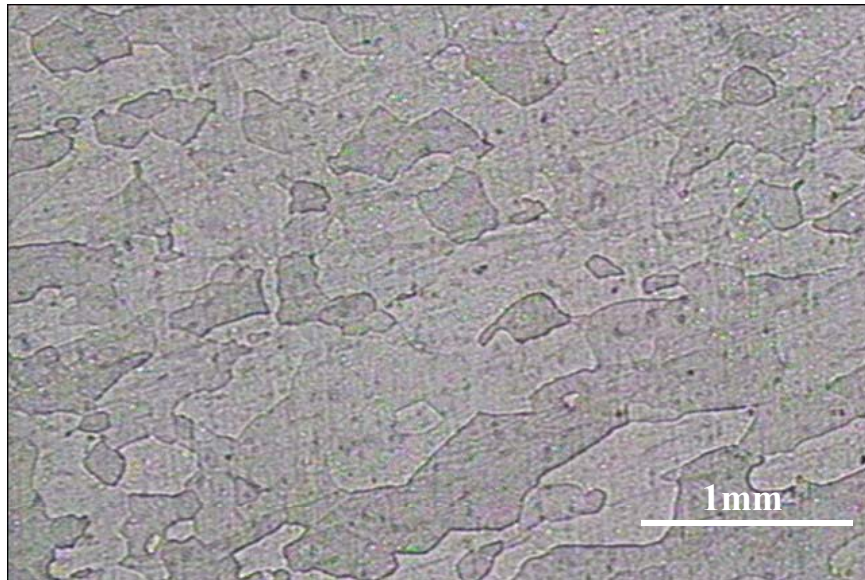


Figure 7. Optical Micrograph of Al Before Prior to Diffusion Bonding, Showing a Nominal Grain Size of 140µm - 150µm.

The phase diagram of the Al/Si system shows very limited mutual solid-solubility at room temperature (298K). At the eutectic temperature (850K, 0.9T<sub>m</sub> of Al), approximately 1.65wt.% of Si can dissolve into Al and at 12.5wt.% Si, an eutectic comprising nearly pure Al and Si forms [61]. Likewise, a maximum of only 0.5wt.% of Al can dissolve into Si at the eutectic temperature. The interfacial chemistry and hence, the thickness of the inter-diffusion zone can easily be controlled, thereby producing a sharp Si/Al interface.

## **2. Sample Preparation**

Pieces of silicon (28.5 x 28.5 x 6.5mm) were sectioned from a four-inch diameter single crystal ingot and polished to a 1 $\mu$ m finish on both square surfaces using standard metallographic polishing techniques. In addition, the edges and corners of Si were rounded and polished (5 $\mu$ m SiC finish) to reduce the risk of crack propagation during diffusion bonding. Pieces of Al (29 x 29 x 20mm) were sectioned from a hot-rolled plate with the rolling direction (RD) pointing normal to the interface. One side was polished to a 3 $\mu$ m finish using standard polishing techniques followed by an ultrasonic cleaning to remove any embedded abrasive particles. The Al pieces were slightly larger than the Si pieces in order to avoid complex stress gradients near the edges or corners of the Si during die pressing.

Surface profiles of Si and Al were obtained by atomic force microscopy (AFM) following surface preparation and prior to bonding as shown in Figures 8 and 9. This information was used to correlate the final polishing condition (polishing grit and grit size) with the resultant surface roughness. The AFM data was obtained at 0.75Hz scan rate over a 5x5 $\mu$ m to 40x40 $\mu$ m square area in contact mode using 25nN constant force. Because the hardness of Al is less than that of Si, the same grit produced deeper trenches (scratches) in Al than in Si. The relative roughness of Al and Si were found to be critical to subsequent diffusion bonding. In general, an Al surface, which is slightly rougher than the Si surface was found to be optimal, enabling the Al to fill the interstices of the asperities on Si via, localized plastic flow upon application of pressure. Ultimately, the surfaces of the Al and Si were optimized using 1 $\mu$ m diamond grit for Si and 3 $\mu$ m diamond grit for Al, in order to reduce bonding pressure (so as to prevent the Si from cracking), while providing intimate contact. The flatness and parallelism of mating surfaces were carefully monitored during sample preparation and any deviation from parallelism was limited to 0.04°. Following surface preparation, the prospective mating surfaces of Al and Si were sequentially degreased and deoxidized by rinsing in a series of reagents, as shown in Table 3.

	Trichloroethylene (Degrease)	Acetone (Degrease)	Isopropyl Alcohol (Drying)	10% HF (Deoxidize)	De-ionized H <sub>2</sub> O (Rinse)	Ethanol (Rinse)	Dry in Hot Air
Silicon	4min	4min	4min	2min	10min	--	5min
Aluminum	4min	4min	4min	--	--	10min	5min

Table 3. Cleaning Sequence for Surfaces of Si and Al Prior to Diffusion Bonding.

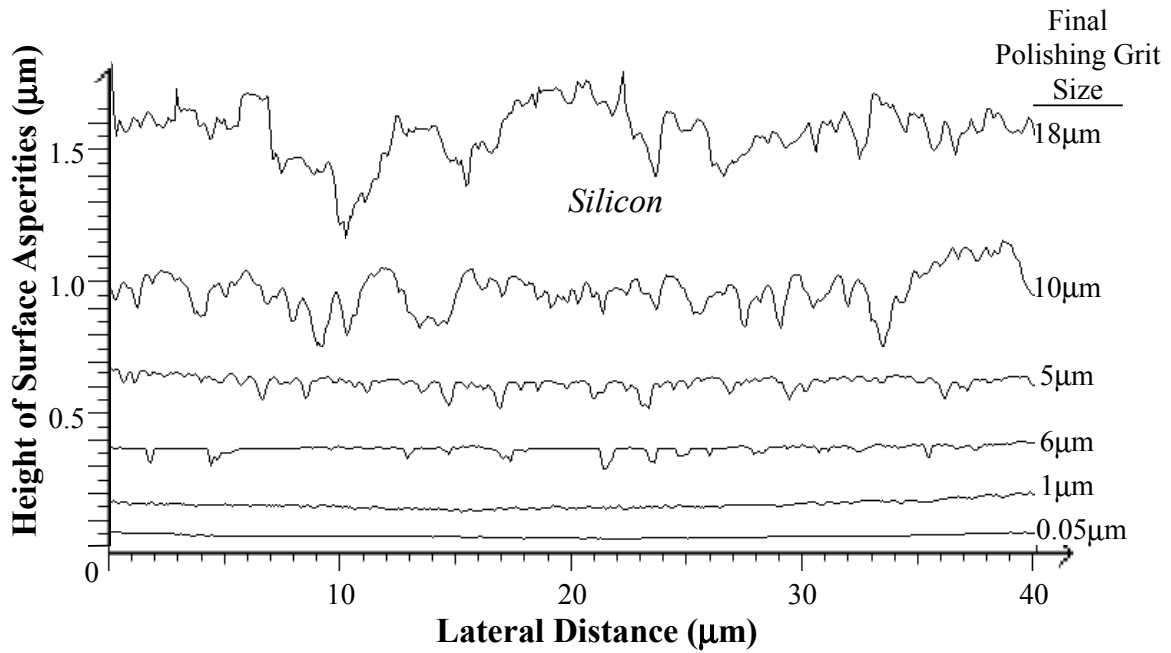


Figure 8. AFM Roughness Measurements on the Surface of Silicon after Using Various Grits and Grit Sizes During Final Polishing.

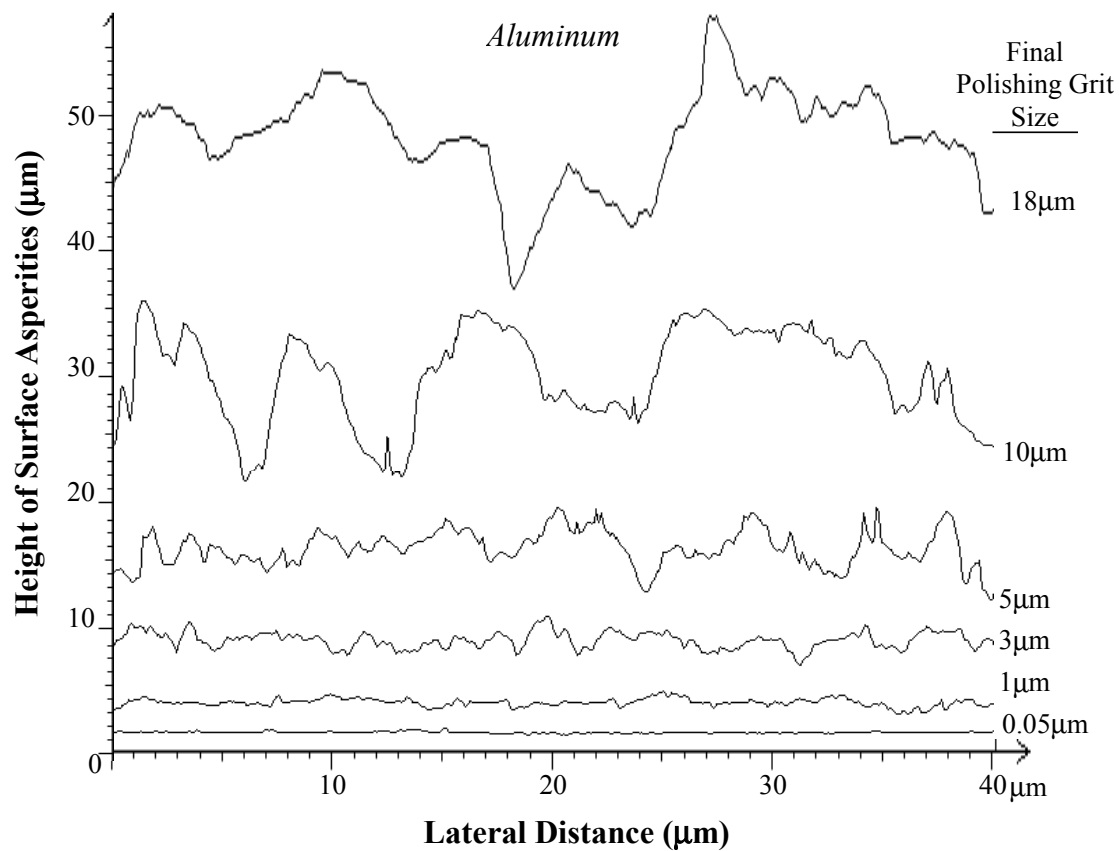


Figure 9. AFM Roughness Measurements on the Surface of Aluminum after Using Various Grits and Grit Sizes During Final Polishing.

### 3. Diffusion Bonding

The polished and chemically treated pieces of Si and Al were stacked in the appropriate sequence (Al-Si-Al) and wrapped with aluminum foil to prevent contamination from the die lubricant during bonding. The stacked pieces were loaded into an uniaxial pressing die made of hardened high carbon steel as shown in Figure 10. The inside walls of the die and punch were lubricated with molybdenum IV sulfide ( $\text{MoS}_2$ ). The setup was inserted into a vacuum chamber which was roughed to approximately  $\sim 1.3\text{Pa}$  ( $10^{-2}$  torr) by alternately evacuating and back-filling the chamber with  $\text{Ar}/2\%\text{H}_2$  gas mixture three times. A diffusion pump was then used to pump the chamber down to  $\sim 1.3 \times 10^{-4}\text{ Pa}$  ( $10^{-6}$  torr). Once high vacuum was achieved, the diffusion-bonding chamber was heated to 843K at a rate of  $\sim 60\text{K}/\text{min}$ . The selection of

this temperature was based on the observation that (a) below 841K, no diffusion bond formed no matter how high the bonding pressure, and (b) above 850K, the eutectic formed resulting in an uncontrollable interfacial structure and chemistry. Once thermal equilibrium was reached, an uni-axial pressure of 1.5MPa was applied on the sandwich structure normal to the interface, and held for one hour. This diffusion-bonding pressure (1.5MPa) yields a creep rate of  $10^{-3}/s$  to  $10^{-2}/s$  at 843K ( $0.9T_m$ ) for Al with a grain size of  $10\mu m$  to 1mm, a calculation based on Reference 62. The shear deformation at the Al/Si interfaces effectively disperses the tenacious oxide film that exists on Al [63-65]. A schematic of the complete experimental setup is shown in Figure 11. After diffusion bonding was complete, the pressure was slowly removed (0.1MPa/min) and the chamber was cooled very slowly to ambient temperature at  $\sim 10K/hr$  to minimize the residual stresses. The specimen was then carefully removed from the die, inspected, sectioned and polished to a  $5\mu m$  finish for future mechanical tests [58].

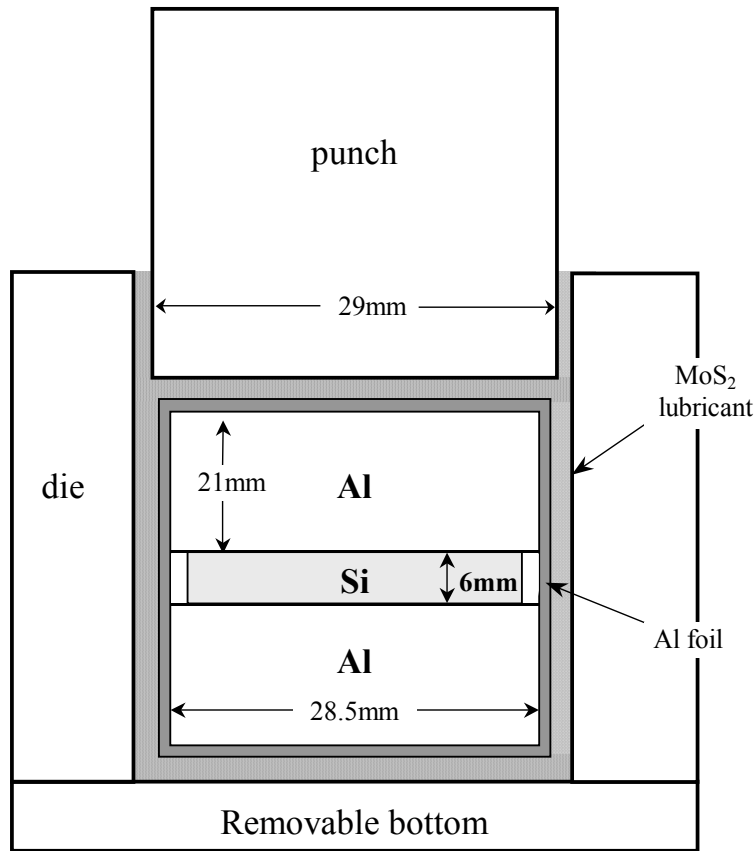


Figure 10. Schematic of Die, Punch and Specimen Lay-Up Used in Diffusion Bonding.



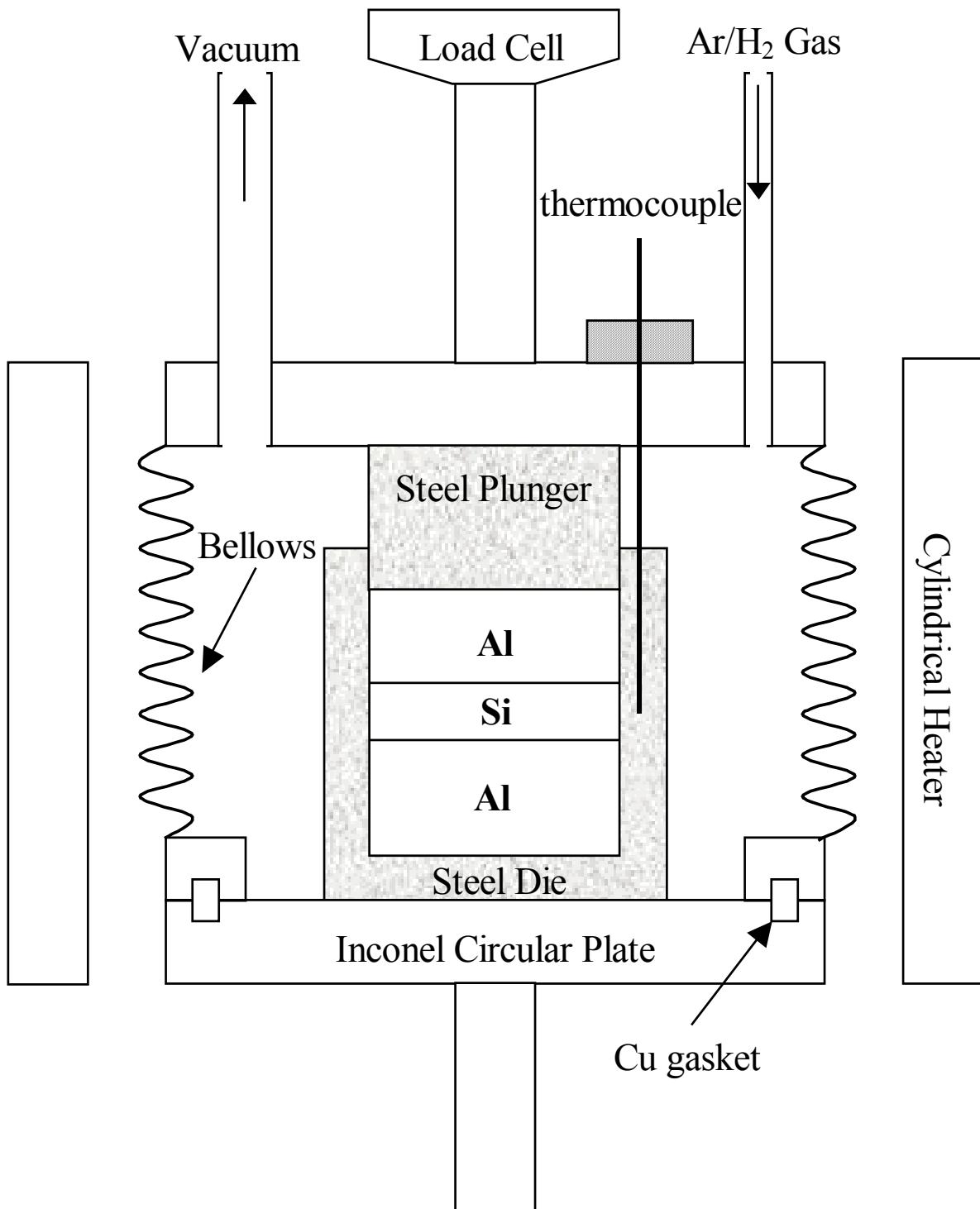


Figure 11. Diffusion Bonding Apparatus Using a Mechanical Testing System, High Vacuum System, Cylindrical Furnace, Welded Bellows, Die and Punch.

#### **4. Specimen Preparation for Microscopy**

Following diffusion bonding, samples were characterized using optical microscopy, orientation imaging microscopy (OIM) in the scanning electron microscope (SEM), and transmission electron microscopy (TEM) to study the structure and chemistry of the interfacial region. Optical microscopy and SEM samples were polished to a 0.05 $\mu\text{m}$  finish using standard polishing techniques with various sizes of SiC, diamond, and silica grits. The specimens for optical microscopy were etched for 60 seconds with modified Keller's reagent (1% HF, 1.5% HCl, 10% HNO<sub>3</sub>, 87.5% H<sub>2</sub>O). The SEM samples for OIM were electropolished for 15 seconds at 37 volts in 20% perchloric acid/80% ethanol reagent as the final preparation for orientation imaging. For cross-sectional TEM, 250 $\mu\text{m}$  thick slices were cut from the diffusion bonded specimen perpendicular to the interface, and ground on both sides to a thickness of 80 $\mu\text{m}$  using 5 $\mu\text{m}$  SiC grit. The thin specimens were initially dimpled to 2 - 5 $\mu\text{m}$  thickness using 1 $\mu\text{m}$  diamond paste, followed by a final dimpling step using 0.25 $\mu\text{m}$  diamond paste. The samples were then ion-milled in a cold stage at 6keV and 0.5mA at 12° tilt for approximately 8 hours.

### **C. RESULTS AND DISCUSSION**

Several attempts with different equipment and diffusion-bonding parameters were used to produce the requisite interfaces, but some attempts were unsuccessful. Initial attempts utilized a vise to clamp the Al-Si-Al sandwich together while heating. This was done first in a flowing argon (Ar) atmosphere and then in low vacuum (0.67 Pa or 5x10<sup>-3</sup> torr), neither of which produced good interfaces. Subsequently, the approach described in Section 3 was developed and refined. Table 4 summarizes the conditions used for the various diffusion bonding experiments along with the results. In general, diffusion bonding in air or a positive pressure of inert gas was not sufficient to stop oxidation during heat up, and appeared to cause entrapment of gases at the interface. Also, when Al surfaces were as smooth or smoother than Si, large bonding pressures were required and still produced inferior results, since all the inter-asperity spaces on Si were not penetrated by Al. Conversely, when the asperities of Al were too large, they promoted

good bonding but left numerous cavities near the interface with a highly deformed structure.

Apparatus	Temp (K)	Press (MPa)	Time (mins)	Vacuum (Pa)	Polish Used (Al/Si)	Bond
Vise	823 - 838	fixed vise gap	30 - 120	Ar purge	0.05/0.05 – 6µm/6µm	Poor
Vise	848	fixed vise gap	60 - 240	Ar or 0.67	1µm/1µm	Fair
uni-axial die press	838 - 848	0.2 - 5.0	30 - 120	atm	1µm/1µm	Fair
uni-axial die press	843	1.2 - 1.8	60	1.3 x 10 <sup>-4</sup>	3µm/1µm	Good

Table 4. Diffusion Bonding Conditions for Various Experimental Setups.

The surface topography of the polished Si and Al may be represented using a simple model based on a periodically varying surface relief,  $y$ , as:

$$y = \frac{h}{2} \cos\left(\frac{2\pi x}{\lambda}\right) \quad (4.1)$$

Here  $x$  and  $y$  are the in-plane and out-of-plane positions along the interface,  $h$  is the peak-to-trough height variation of the surfaces, and  $\lambda$  is the periodicity of the surface roughness (peak-to-peak) along the interface. The amplitude ( $h/2$ ) or the ratio of  $h/\lambda$  of the asperities may be used to represent the surface roughness of a material, which depends on the hardness and grit size of the abrasive used, the hardness and type of material being polished, and the amount of pressure applied during polishing. Based on the AFM measurements, the peak-to-trough height variations of the asperities ( $h$ ) were calculated as twice the statistical root mean square (RMS) of the amplitude of the asperities (roughness) while the wavelengths ( $\lambda$ ) were calculated by averaging the peak-to-peak distances of the asperities for each scanned surface. Then, the amplitude ( $h/2$ )

and the ratio of  $h/\lambda$  were correlated with the final abrasive grit size used for each polished surface. Figure 12a shows the variation of RMS amplitude ( $h/2$ ) for the polished surfaces of Si and Al as a function of the final polishing grit. Two important points to note are (1) the roughness obtained after sample preparation is considerably finer than the final polishing grit size used and (2) the same polishing grit produces a much finer surface on Si than on Al. Figure 12b shows that the normalized surface roughness ( $h/\lambda$ ) of Si and Al have a similar dependence on the final abrasive grit size used during final polishing. The surface roughness of Si and Al that produced optimal results for diffusion bonding was found to exist when the Al ( $h \cong 100\text{nm}$  or  $h/\lambda \cong 0.39$ ) was slightly rougher than the Si ( $h \cong 20\text{nm}$  or  $h/\lambda \cong 0.16$ ).

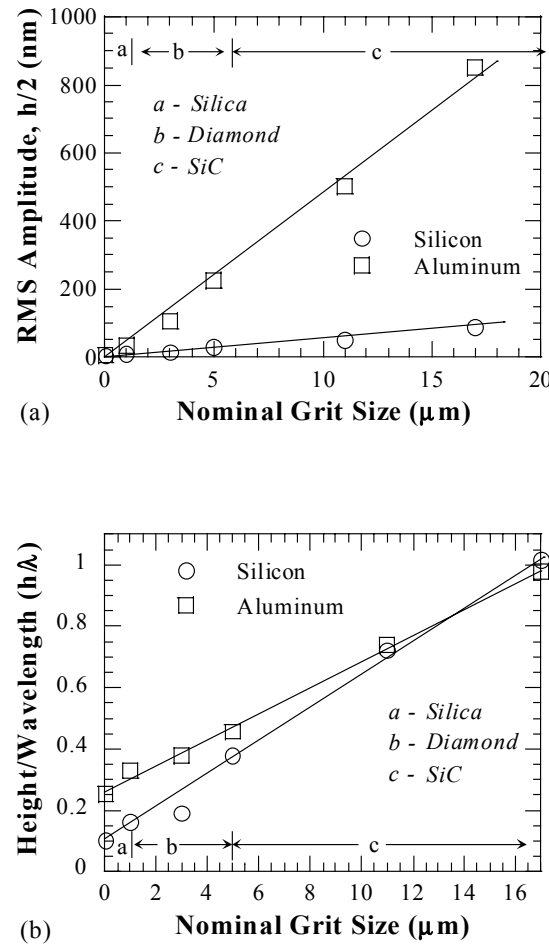


Figure 12. (a) Surface Topography,  $h/2$ , and (b) Ratio of Height over Wavelength,  $h/\lambda$ , for Si and Al as a Function of the Final Polish Used.

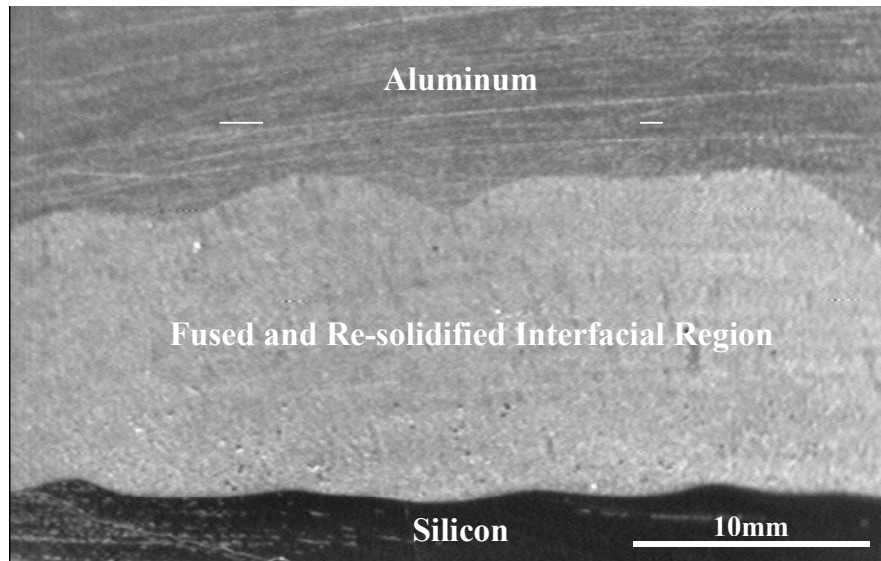


Figure 13. Si/Al Interface Morphology after Diffusion Bonding at 855K (Slightly Above the Eutectic Temperature for ~10 Minutes at 3MPa. The Micrograph Shows that In-Situ Melting of the Interfacial Region Produces a Thick Interfacial Region with Non-planar Si-Al Interfaces.

Some of the experiments allowed the diffusion bonding temperature to slightly exceed the eutectic temperature (850K) for approximately 10 minutes. In these samples, the Al/Si interfaces lost their planar shape and created a thick (on the order of millimeters), albeit strong, interfacial region as shown in Figure 13. A melted and re-solidified layer is readily visible at the Si/Al interface. Once melting occurred, it was difficult to control the morphology and thickness of the interface because of rapid diffusion through the liquid. Since planar interfaces are desirable for most applications, bonding temperatures for all the experiments reported here were limited below the eutectic temperature.

All the unsuccessful attempts to diffusion bond Si to Al could be traced to insufficient temperature, insufficient pressure to deform the asperities, insufficient time to allow inter-diffusion to occur, lack of intimate contact due to mismatch between the surface roughness of the two materials, unbroken surface oxide layers, and contamination at the interface acting as diffusion barriers. These deficiencies were corrected by raising the bonding temperature close to the Al/Si eutectic temperature, increasing the bonding

time to one hour, polishing and chemically treating the mating surfaces immediately prior to diffusion bonding, and purging the system with a reducing gas (Ar/2% H<sub>2</sub>) before drawing high vacuum. In addition, bonding pressure was increased while using the optimal surface roughness between Si and Al, which allowed sufficient Al to flow into the interstices of the asperities on the surface of Si.

Figure 14 is an optical micrograph that shows an Al grain size of 20 $\mu$ m-80 $\mu$ m adjacent to the diffusion-bonded interface and increases to approximately 100 $\mu$ m-150 $\mu$ m a couple grain diameters away. This is supported by the OIM micrograph in Figure 15a, which plots all grain boundaries with a misorientation of 7° or higher. Figure 15b shows the crystal orientation for the large grains away from the interface (relative to 200, 220, and 111 poles), where a clear <100> cube texture is observed. However in the immediate vicinity of the interface, where the grains are small, the cube-texture was presumably replaced by a nearly random texture. Clearly, nucleation of new textureless grains has occurred via recrystallization at the interface during diffusion bonding. This is possibly due to a mechanism analogous to the phenomenon of particle stimulated nucleation (PSN) of recrystallization during thermo-mechanical cycling [66-69], where new strain-free, textureless grains can nucleate in a soft matrix immediately adjacent to a hard material due to large lattice rotations associated with intense localized plasticity. Here, this locally intense plasticity is probably associated with the surface asperities of Al which are subjected to large local strains under the bond-pressure, and is essential to the formation of a diffusion-bond with Si, since it allows the native oxide layer on Al to break up and disperse.

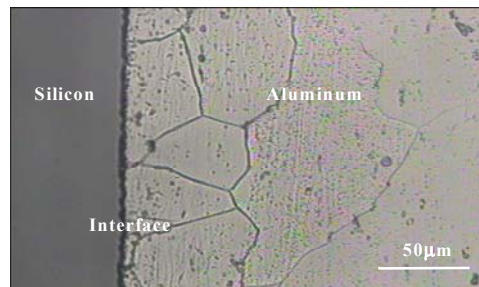


Figure 14. Optical Micrograph of Diffusion Bonded Si/Al Interface Etched in Modified Keller's Reagent. The Grain Size of Al Close to the Interface is Significantly Smaller than that Farther Away.

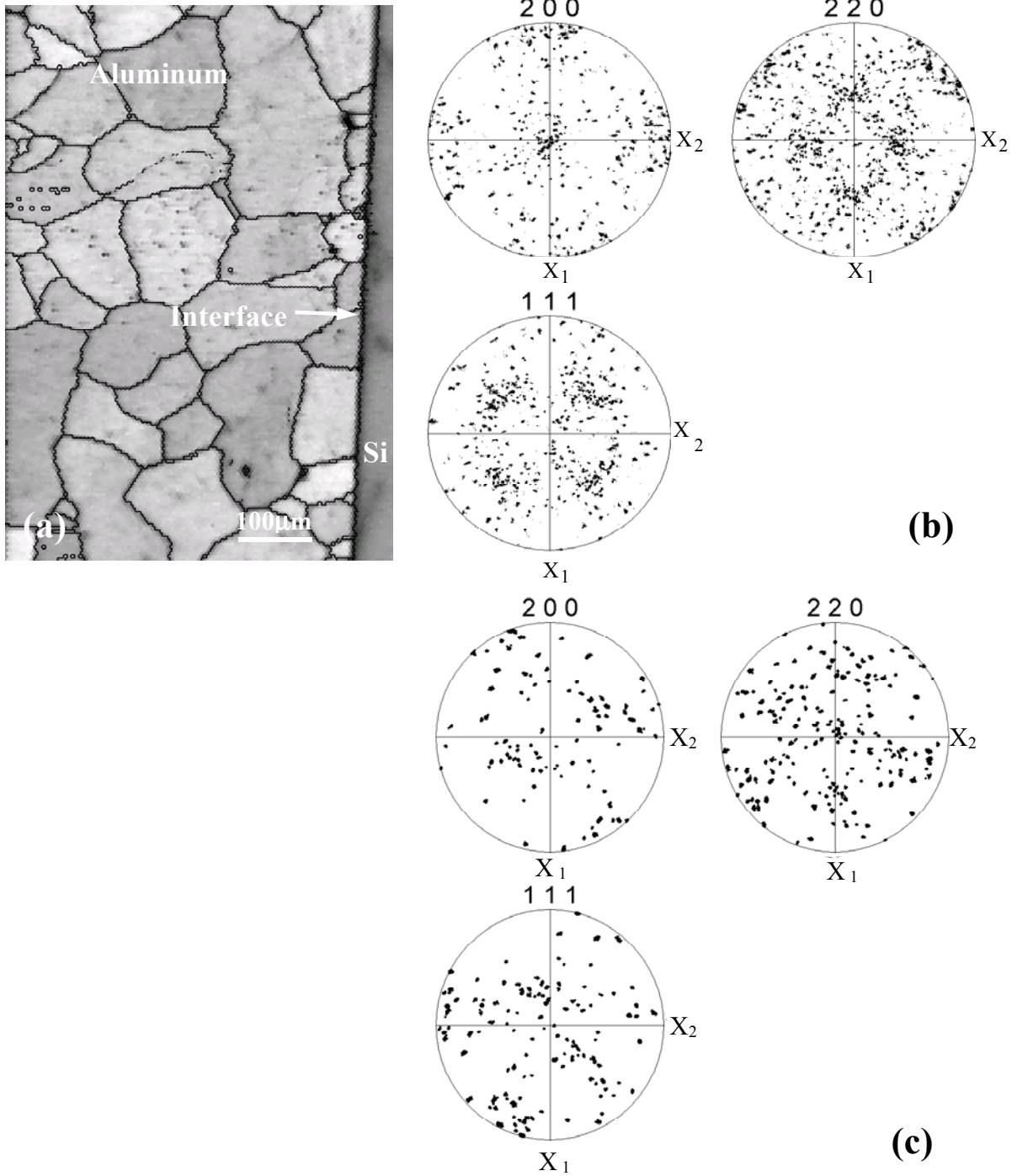


Figure 15. OIM Micrograph Showing Small Al Grains ( $\sim 20 - 80 \mu\text{m}$ ) Immediately Adjacent to the Interface and Larger Grains ( $\sim 100 - 150 \mu\text{m}$ ) Farther Away (a). The Grains Far from the Interface Have a Cube Texture (b), Whereas Those Immediately Adjacent to the Interface Have No Texture (c).

Further investigation of diffusion-bonding effects on the interface was conducted using cross-sectional TEM. The bright field TEM image in Figure 16a shows the Si/Al interface to be well bonded. Figure 16b shows a bright field image with a subgrain structure of  $\sim 1 - 2\mu\text{m}$  in the Al away from the interface. An even smaller subgrain structure ( $\sim 300 - 600\text{nm}$ ) is observed immediately adjacent to the interface as shown in Figure 16c. Overall, the Al immediately next to the interface was found to contain a fine subgrain structure, with a very low overall dislocation density. No evidence of thermally generated dislocations (due to CTE mismatch between Al and Si during cooling) was found, suggesting that the structure is nearly fully recovered/recrystallized. This is consistent with the mechanism analogous to PSN proposed here, which allows new Al grains to nucleate next to the interface during diffusion bonding. The prevalence of such a mechanism seems particularly likely since the intense strain localization associated with the interface would allow recrystallization to occur at relatively small global strains, and may result in nearly randomly oriented grains next to the interface, as observed here.

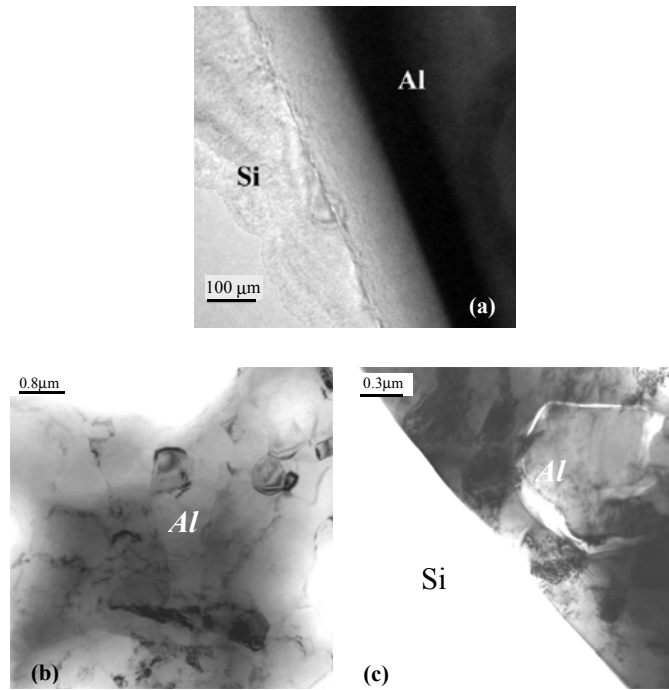


Figure 16. (a) Bright Field TEM Image Showing a Diffusion Bonded Si/Al Interface, (b) Microstructure of Al Away from Interface Showing Larger Grains  $\sim 1-2\mu\text{m}$ , and (c) Showing Small Grains/Subgrains with Size of  $\sim 300\text{nm}$  along the Interface and Very Low Dislocation Density.



Figure 17a shows a bright field TEM image of the Si/Al interface, with an inset showing the region over which the elemental maps were obtained for Si, Al, O and S (Figures 17b – 17e). Figures 17b and 17c show that the diffusion-bonded Si/Al interface is sharp with a very narrow inter-diffusion zone between Si and Al. Figures 17d and 17e further show that there is some segregation of oxygen and sulfur on the Al side, about 100nm from the Si/Al interface. In particular, there is an appreciable concentration of oxygen at the interface, most likely from the native oxide layers present on Si and Al prior to diffusion bonding. The small amount of sulfur in the interfacial region is probably associated with MoS<sub>2</sub> used for lubricating the die during pressing. Although the distance between the sharp Si/Al interface and the band of solutes is significant (~100nm), it is on the same order as the surface roughness of Al present prior to diffusion bonding (3 $\mu$ m grit used on Al renders ~100nm surface roughness in Figure 12a). As previously discussed, the solutes are probably present on the surface of Al prior to and during bond-pressing, which breaks up the oxide layer, and allows this surface layer to get trapped away from the interface as the surface asperities of Al undergo intense plastic flow and recrystallization. It should be noted that the thickness of the segregated region and its distance from the interface vary considerably along the interface.

HREM of the interface revealed that an amorphous layer, ranging in thickness from ~20 to 100nm, was present at the Si/Al interface on the Al side, roughly corresponding to the region of solute segregation as noted above. Figure 18 shows a montage of HREM images of the Si/Al interface, along with the computed fast Fourier transforms (FFT) of the lattice images of Si, Al and the intervening amorphous zone. The Si side of the interface displays a relatively sharp transition to the amorphous region, which is situated almost entirely on the Al side, showing a gradual transition to crystalline Al. This is clear from the FFT pattern from the apparently crystalline part of Al, which shows the spots due to the lattice planes are superimposed by a diffuse intensity due to the amorphous character. Amorphous layers on the order of a few to several tens of nanometers thick are frequently observed at interfaces in both bulk and thin film systems with either Al/Al<sub>2</sub>O<sub>3</sub> or Si/SiC on one side [70-73]. This is typically associated with adsorbed oxygen and/or nascent oxide layers on the surfaces of Si and Al

[70]. In this present work, the amorphous layer is somewhat wider (up to 100nm in some areas along the interface) than these typically found, and extends from the Si/Al interface to the far side of the solute band on the Al side. This is possibly attributable to the relatively large asperities present on the Al prior to diffusion bonding, which allowed the surfaces contaminants to get embedded deeper inside the Al side (i.e., further away from the interface) during bonding. It is thought that the highly non-equilibrium amount of dissolved solute results in the formation of the amorphous Al region next to the interface.

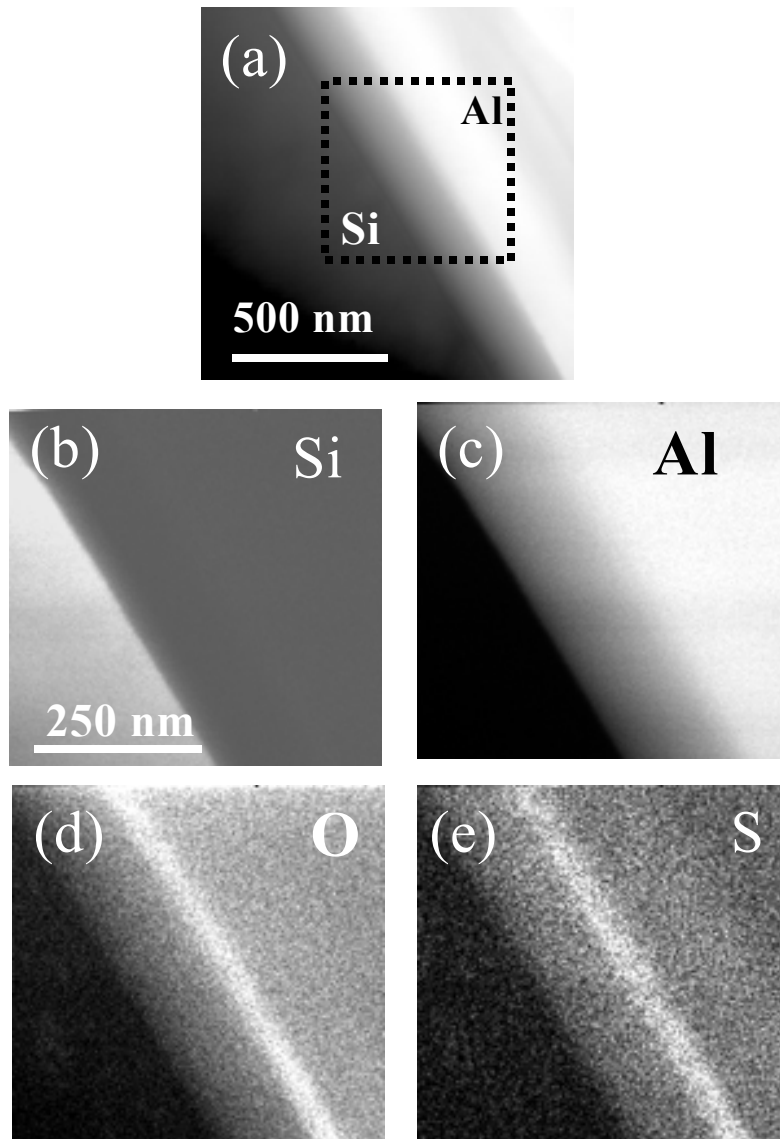


Figure 17. X-Ray Maps Across the Si/Al Interface Showing a Thin Oxygen-Rich Layer, Where Trace Contaminants (i.e., Sulfur) Segregate.

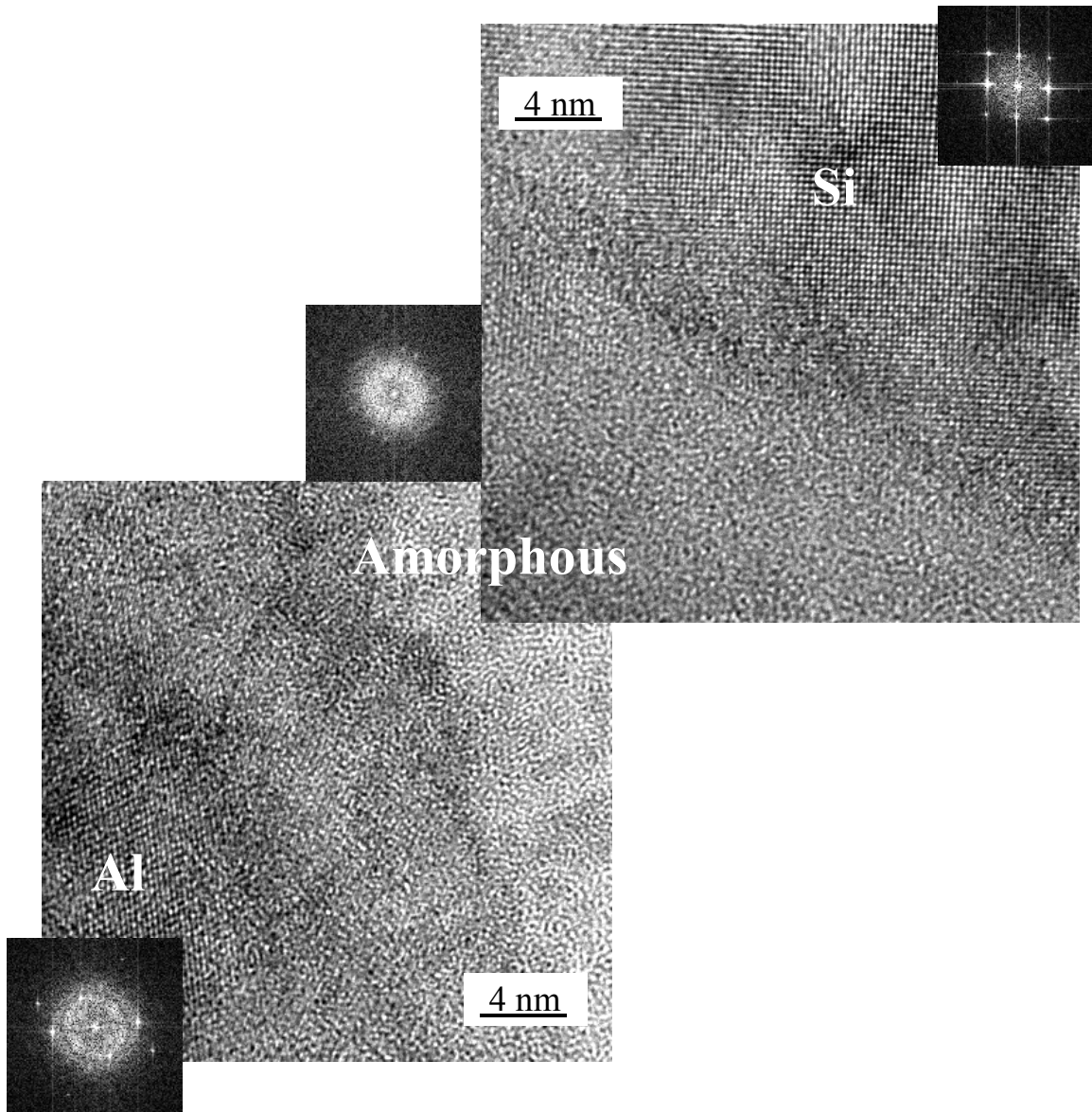


Figure 18. HREM Micrograph Showing Lattice Image of the Single Crystal Si, a Sharp Interface Between the Si and ~40nm Thick Amorphous Region, and a Gradual Transition from the Amorphous Region to the Al Crystal.

In order to determine the approximate shear strength of the diffusion-bonded interface, constant displacement rate ( $15\mu\text{m/s}$ ) tests using a double-shear test configuration were performed at temperatures ranging from ambient to 538K. Here, the two parallel interfaces in the diffusion-bonded Al/Si/Al sandwich were simultaneously loaded in shear, and the average interfacial shear stress  $\tau$  is plotted against the

displacement of the bottom surface of Si  $\delta$  (which corresponds to the displacement of the interfacial region), as shown in Figure 19. The loading geometry is shown in the inset, where  $\tau=F/2A$ ,  $F$  being the applied force and  $A$  being the area of each Si/Al interface. This geometry has been successfully used earlier to study the creep behavior of Si/Al interfaces [58].

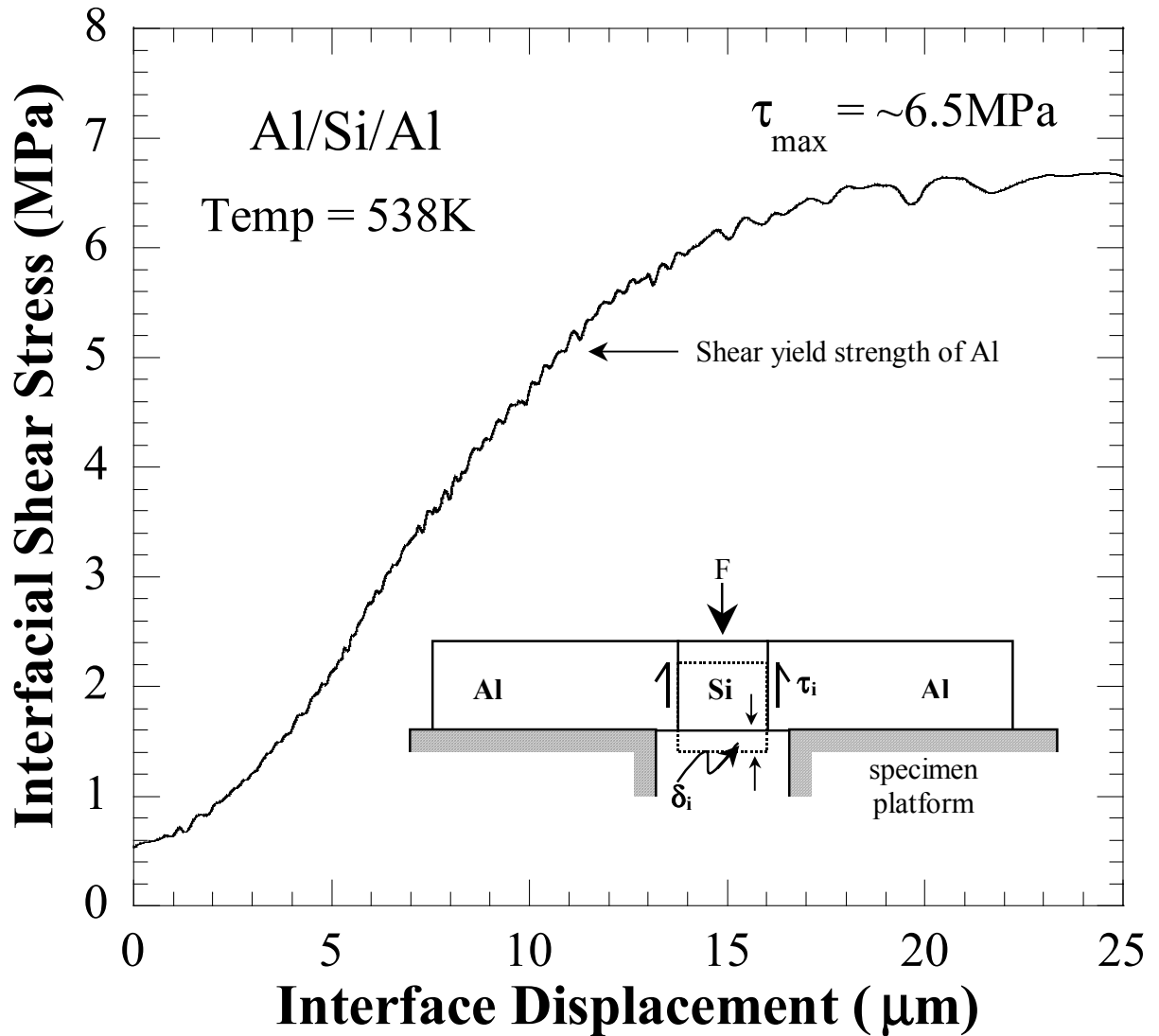


Figure 19. Plot of  $\tau$  Versus  $\delta$  at 538K, Showing the Onset of Non-Linearity ( $\sim 4.5 \text{ MPa}$ ) Commensurate with Shear Yielding of a Very Thin Region of Al Immediately Adjacent to the Si-Al interfaces. Inset Shows the Testing Configuration for the Double Shear Al/Si/Al Specimen.

It is observed from Figure 19, which plots  $\tau$  versus  $\delta$  for the highest test temperature (538K), that beyond the initial slack in the load-train, there is first a linear region, which extends to about 4.5MPa, and then the plot transitions to non-linearity. At 538K, the Si underwent continuous downward displacement up to  $\sim 30\mu\text{m}$ , whereupon, the test was terminated. Inspection suggested that there was no failure of the Si-Al interface, and that a thin layer of Al immediately adjacent to the interface underwent plastic flow, thereby causing the observed displacement  $\delta$ . For 99.8% Al, the shear yield strength of Al at 538K is approximately 4MPa [60, 74], in agreement with the hypothesis that the observed non-linearity is due to plastic flow of Al. Clearly, since plastic flow of the Al precluded interfacial fracture, the interfacial shear strength must be greater than the shear flow stress of the Al ( $\sim 6\text{MPa}$ ). Although, at 538K, plasticity precludes crack propagation, at the lower temperatures, the onset of non-linearity (which was observed to be  $\sim 5\text{MPa}$ ) may also be attributed to the initiation of stable crack growth at the interface in Mode II from the top face of the specimen [75].

It should be noted that the surfaces of the test samples, albeit mechanically polished to a  $5\mu\text{m}$  finish prior to testing, leave trenches with depths on the order of several microns at the interface, as clearly observed from Figure 14. These polishing artifacts act as in-situ interfacial cracks, thereby enabling the crack initiation fracture toughness ( $J_{\text{IC}}$ , which is proportional to  $\tau^2$  and  $a$ , where  $a$  is the crack length) to be reached at a relatively low applied shear stress value. Therefore, despite the relatively low  $\tau$  values observed for the onset of non-linearity, it is deemed that the interface is moderately tough.

It is likely that the interfacial toughness is limited due to the presence of a glassy (amorphous) phase as noted in the TEM micrographs, since the continuous amorphous phase is likely to provide a preferential crack propagation path. In addition to limiting the fracture toughness of the interface, the amorphous interfacial layer has also been noted to increase creep susceptibility of the interface by providing a short circuit diffusion path [58]. It is therefore suggested that future efforts focus on the minimization of the amorphous region at the interface to improve the interfacial properties

#### **D. CONCLUSION**

Well-bonded Si/Al interfaces were produced via diffusion bonding in high vacuum at 843K for 1 hour with an applied pressure of 1.5MPa in an uni-axial compression die. The surface roughness ( $h$ ) of Si and Al that produced optimal diffusion bonding results were  $h \cong 18\text{nm}$  ( $h/\lambda \cong 0.16$ ) for Si and  $h \cong 210\text{nm}$  ( $h/\lambda \cong 0.39$ ) for Al, where the Al was rougher than Si. An amorphous O-rich region formed on the Al side of the interface. The Si/amorphous interface was sharp compared to the Al side, where the amorphous region gradually transitioned to crystalline Al as the solute concentration decreased. Shear strength measurements of the Si/Al interface suggest that the Al/Si interface is moderately tough.

THIS PAGE INTENTIONALLY LEFT BLANK

## V. KINETICS OF INTERFACIAL CREEP AT Al-Si INTERFACES

*Accepted for publication by Scripta Materialia in July 2002  
(co-authored with I. Dutta and M. W. Chen)*

*and*

*Submitted for publication to Acta Materialia in September 2002  
(co-authored with I. Dutta and M. W. Chen)*

### A. INTRODUCTION

Interfaces may have a profound effect on the mechanical properties and dimensional stability of multi-component materials, such as composites, multi-layers and thin-film / substrate systems. Large shear stresses may develop at interfaces between dissimilar materials during thermo-mechanical excursions when there is a significant difference in the coefficient of thermal expansion (CTE) between them. Most typically, these shear stresses are confined to the extremities of one of the components, such as fiber-ends in a composite, or the edges of a thin film on a substrate [e.g., 4, 76]. However, when the dimensions of the phases is small, e.g., for narrow metallic thin film lines on a substrate or short discontinuous fibers embedded in a metallic matrix, these shear stresses may prevail over a large area fraction of the total interface. Under appropriate thermal-mechanical conditions, the interface may slide via diffusional processes, thereby accommodating relative dimensional changes between the phases. This phenomenon has been noted in metal-matrix composites where fiber-ends were observed to either intrude into, or protrude from the matrix following thermal cycling [1, 5], and in thin-film Al and Cu interconnects on Si, where the film-footprint on the substrate was found to change after thermal cycling [6, 8]. It has also been observed in Cu-dielectric interconnect structures on Si devices, where thickness differences were noted to arise between adjacent Cu and dielectric thin film lines after thermal cycling [11]. In each of the above cases, differential strains between adjacent phases, driven by CTE mismatch, were accommodated at the interface by a diffusionally accommodated sliding process, in the absence of interfacial fracture or decohesion. With the continuing



trend towards miniaturization of components with numerous multi-material interfaces in microelectronics, MEMS, etc., where one or more material(s) is subjected to high homologous temperatures, interfacial sliding is likely to play an increasingly important role, making it imperative to develop a mechanistic understanding of this phenomenon.

Funn and Dutta [3] measured the kinetics of interfacial sliding in Pb-Ni and Pb-SiO<sub>2</sub> single fiber composites, and proposed that sliding occurs via diffusional creep. The basic mechanism is akin to that of grain boundary sliding [32], where an applied far-field stress causes normal stress gradients at the interface due to topographical variations, allowing mass transport, and hence sliding, along the interface. It was shown that the interfacial shear displacement rate due to sliding is given by:

$$\dot{U} = \frac{4\delta_i D_i \Omega}{kTh^2} \left[ \tau_i + 2\pi^3 \left( \frac{h}{\lambda} \right)^3 \sigma_n \right] \quad (5.1)$$

where  $\delta_i$  and  $D_i$  are the interfacial thickness and diffusivity, respectively,  $\Omega$  is the atomic volume of the diffusing species,  $\lambda$  and  $h$  are the topographical periodicity and roughness of the interface respectively, and  $k$ ,  $R$ , and  $T$  have the usual meanings. The interfacial shear stress  $\tau_i$  is the primary driving force for this process, which is enhanced if a tensile normal interfacial stress  $\sigma_n$  is present, or reduced if there is a compressive  $\sigma_n$ . Since  $\dot{U} \propto h^{-2}$ , a smooth interface would slide more readily.

Funn and Dutta [3] were unable to experimentally verify the dependence of sliding kinetics on interfacial normal stress and roughness using single fiber composites, because in their approach the interfacial normal stress resulted from thermal stresses, which varied with the test temperature, and the interfacial roughness (i.e., fiber surface roughness) were not controllable. Recently, Funn and Dutta's experimental approach [3] was refined isolating and measuring the creep behavior of interfaces in multicomponent systems using model diffusion-bonded Al-Si interfaces [58]. Experiments showed that the Al-Si interface underwent diffusionally accommodated sliding under shear stresses at high homologous temperatures. The measured kinetics showed that the mechanism of sliding was interfacial diffusion-controlled. This is consistent with the mechanism

proposed by Funn and Dutta [3] although verification of the dependencies of the kinetics on interfacial morphology and interfacial normal stress was not performed.

In this chapter, we (1) develop a well-controlled experimental approach to systematically study interfacial creep in bulk systems; (2) develop a mechanistic understanding of the phenomenon of interfacial sliding by correlating the sliding kinetics with interfacial structure and stress states; and (3) generate kinetics data for Si-Al system, which is of practical importance in many microelectronics and micro-electromechanical systems (MEMs) applications.

## **B. EXPERIMENTAL PROCEDURE**

The sandwich specimens (Al-Si-Al) were fabricated by a diffusion bonding process from 99.7+% pure polycrystalline Al and undoped, single crystal Si with the crystallographic direction  $\langle 100 \rangle$  pointing normal to the interface [79]. The Al-Si system was chosen because of: 1) the limited mutual solid-solubility allowing the sharpness of the interface to be controlled while promoting good bonding, 2) plethora of creep data available, and 3) the practical importance to the microelectronic industry. Al-Si-Al sandwich structures were fabricated in vacuum ( $10^{-6}$  torr) at a temperature, applied pressure, and time of 838K, 1.5MPa and 1 hour, respectively. Because of the limited mutual solid solubility (At 850K,  $\sim 1.65$  wt% Al in Si and  $\sim 0.5$  wt% of Si in Al [61]), the Al-Si interfaces thus produced were relatively sharp, and yet well bonded [77].

Prior to diffusion bonding, the Al and Si surfaces were metallographically polished to a nominal finish, and sequentially cleaned and degreased in ethanol, trichloroethylene, acetone and isopropyl alcohol, following standard microelectronic processing practice. The roughness of Si was varied by polishing the surface with a final grit size of  $1\mu\text{m}$ ,  $5\mu\text{m}$ , and  $17\mu\text{m}$ . Assuming the changes in the morphology of the interface are negligible during diffusion bonding and creep testing, the interfacial roughness can be taken as the roughness of the surface of Si prior to diffusion bonding. Atomic Force Microscopy (AFM) was used to determine the surface roughness of the Si prior to diffusion bonding as shown in Figure 8. The surface topography of the polished

Si may be represented using a simple model based on a periodically varying surface relief,  $y$ , as:

$$y = \frac{h}{2} \cos\left(\frac{2\pi x}{\lambda}\right) \quad (5.2)$$

Here  $x$  and  $y$  are the in-plane and out-of-plane positions along the interface,  $h$  is the peak-to-trough height variation of the surfaces, and  $\lambda$  is the periodicity of the surface roughness (peak-to-peak) along the interface. The nominal height ( $h$ ) or the ratio of  $h/\lambda$  of the asperities may be used to represent the surface topography. Based on the AFM measurements, the peak-to-trough height variations of the asperities ( $h$ ) were calculated as twice the statistical root mean square (RMS) of the amplitude of the asperities (roughness) while the wavelengths ( $\lambda$ ) were calculated by averaging the peak-to-peak distances of the asperities for each scanned surface. Then, the nominal height ( $h$ ) and the ratio of  $h/\lambda$  were correlated with the abrasive size used for the final polish. Figure 20 shows the variations of nominal height ( $h$ ) and the ratio of  $h/\lambda$  for each scanned surface of Si as a function of the final grit size used during polishing. An important points to note is that the nominal height ( $h$ ) rate of change due to increasing grit size is much larger than the rate of change of  $h/\lambda$ . The height and ratio of  $h/\lambda$  of the asperities of Si will be used in conjunction with Equation 5.1 to show the interface sliding rate dependence on interfacial roughness.

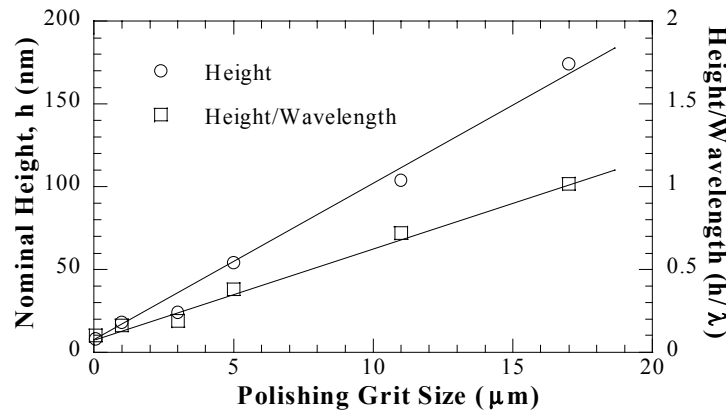


Figure 20. Approximate Interfacial Roughness Corresponding to the Height  $h$  and Ratio of Height over Wavelength  $h/\lambda$  of the Asperities of Si as a Function of Grit Size Used During Final Polishing.

After diffusion bonding, the sandwich structure was cooled very slowly ( $\sim 2\text{K/minute}$ ) in order to minimize thermally induced residual stresses at the Si-Al interfaces. Subsequently, the sandwich was sectioned to produce  $45\text{mm} \times 6\text{mm} \times 6\text{mm}$  test samples (Figure 21a). The sample surfaces were then ground to  $5\mu\text{m}$  and a coated with  $\sim 500\text{nm}$  of Al by physically vapor deposition (PVD) to increase the accuracy and sensitivity of the capacitance gauge that was used to measure the displacement of the bottom of Si.

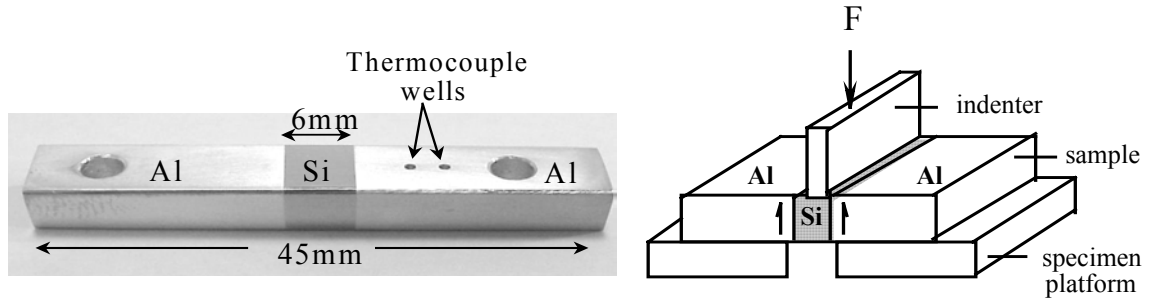


Figure 21. Photo of Interfacial Creep Test Specimen, and (b) Schematic of the Loading Geometry.

The samples were then mounted on a slotted specimen platform with the 6mm wide Si centered precisely on the 7mm wide slot (Figures 21b and 22). The specimen thickness, the widths of the Si layer, and the slot were optimized using finite element modeling, so as to enable uniform shear loading of the two interfaces along the specimen thickness, while minimizing bending stresses. The ratio of the gap opening ( $t_{\text{gap}}$ ) to the width of the Si ( $W_{\text{Si}}$ ) and the ratio of specimen height ( $h$ ) to the gap opening ( $t_{\text{gap}}$ ) was kept close to  $\sim 1.2$ . A tungsten plate indenter, connected to a servo-hydraulic MTS frame equipped with an appropriate load cell (0.1N resolution) was utilized to apply a constant load to the top of the Si. This arrangement allows the two Al-Si interfaces to be loaded in shear ( $\tau_i = F/2A_i$  where  $A_i$  is the cross section-interfacial area). The samples were oriented on the testing platform with the metallographically polished scratches aligned perpendicular to the applied shear stress ( $\tau_i$ ). At the same time, a linear drive DC stepper motor was used in conjunction with an appropriate load cell and the MTS Test Start IIs controller to apply a normal stress ( $\sigma_i = F_n/A_i$ ) to the Si-Al interface as shown in Figure 22.

The resulting time-dependent interfacial deformation (i.e., the relative displacement between Si and Al) was measured with a capacitive displacement gauge (0.01 $\mu\text{m}$  resolution) located inside the slot in the specimen platform, just below the Si. A displacement gauge (0.1 $\mu\text{m}$  resolution) was also used to measure the top of the silicon to verify the displacement of Si. The sample and indenter were heated with twin-radiant heaters interfaced with a proportional controller, which allowed maintenance of the temperature with an accuracy of  $\pm 0.25\text{K}$ . The entire set-up was enclosed in an environmental chamber with a slight positive pressure of forming gas (98%Argon/2% $\text{H}_2$ ) during testing. The shear stress required to de-bond (i.e. fracture) the interface ( $\tau_d$ ) was determined over the temperature span in which the creep tests were performed using constant displacement rate pushdown tests. All creep experiments were conducted at loads well under those required to cause interfacial de-bonding at the relevant temperature.

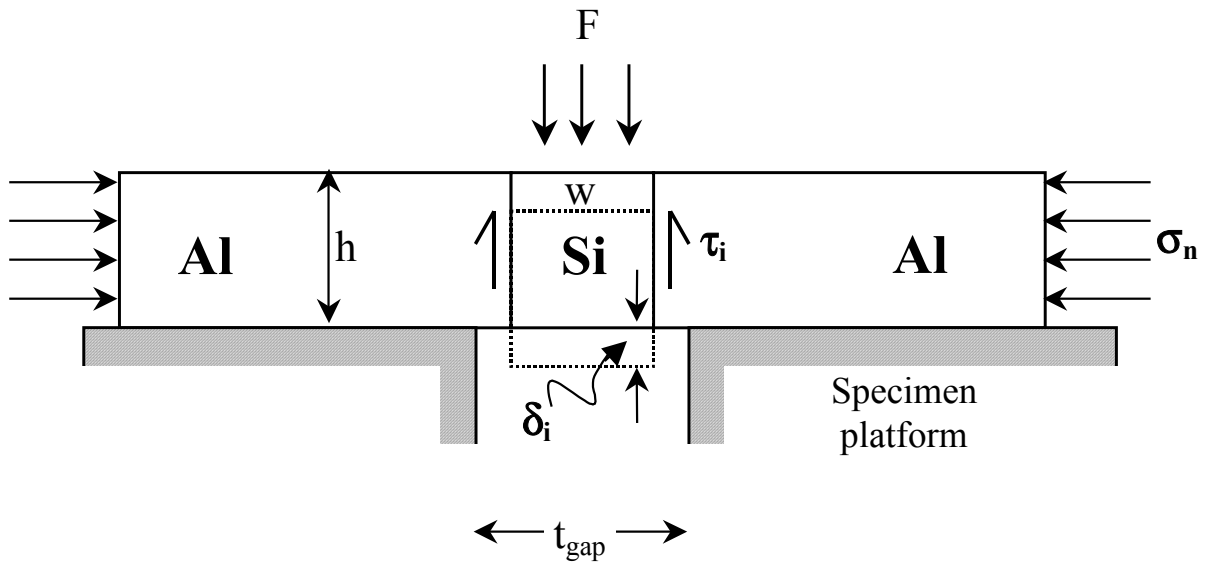


Figure 22. Experimental Approach for Sample Mounting for Double-Shear Test Specimens Showing Applied Interfacial Shear and Normal Stresses.

### C. RESULTS

Figure 23 illustrates the displacement obtained at the Al-Si interface after being subjected to a creep test for 4 hours at 573K and a mean interfacial shear stress ( $\tau_i$ ) of 1MPa, as revealed by a grid pattern of nominally 5 $\mu$ m diameter circles evaporated across the interface in one of the samples. Evidently, all deformation was confined to the interface only, with negligible deformation in either Si or Al. No evidence of interfacial de-cohesion was observed, with the observed displacement being uniform along the interface, and consistent with the measured creep displacement. Clearly, the experimental approach is able to isolate and measure interfacial creep displacements.

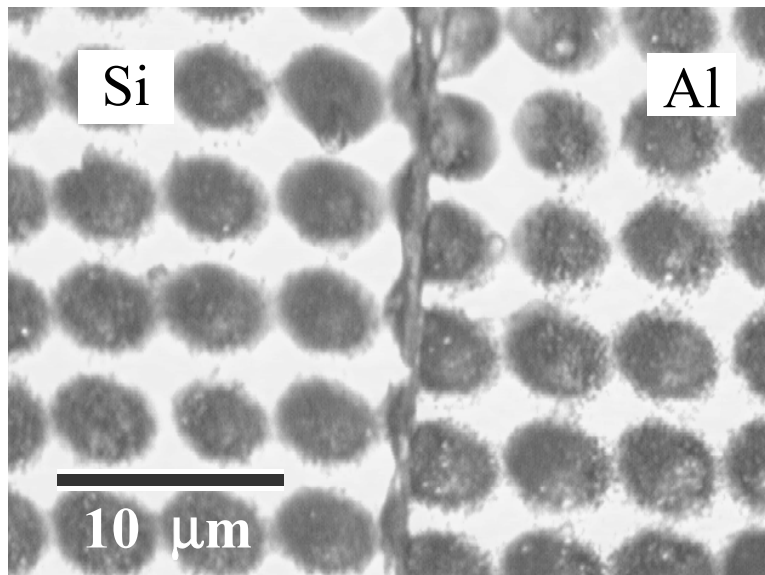


Figure 23. Micrograph Showing Misalignment of Rows of Al Grid Pattern Deposited Across an Al/Si Interface Following Creep Testing at 1MPa and 573K for 4 hours.

Typical creep curves obtained from the interface creep tests are shown in Figure 24. In most cases, steady state was established after ~300-400 minutes. This steady state continued for a long time (at least 24 hours at all tested temperatures and loads), until enough of the Si emerged from the bottom so that the associated reduction in interfacial area resulted in an appreciable increase in  $\tau_i$ .

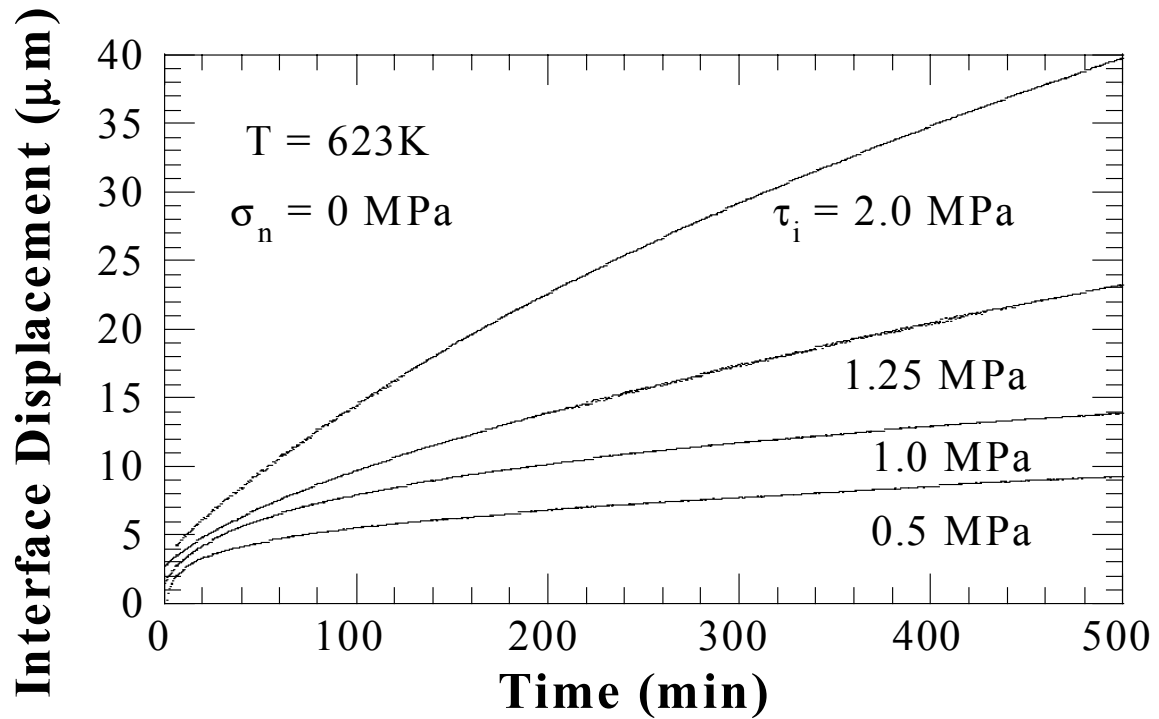
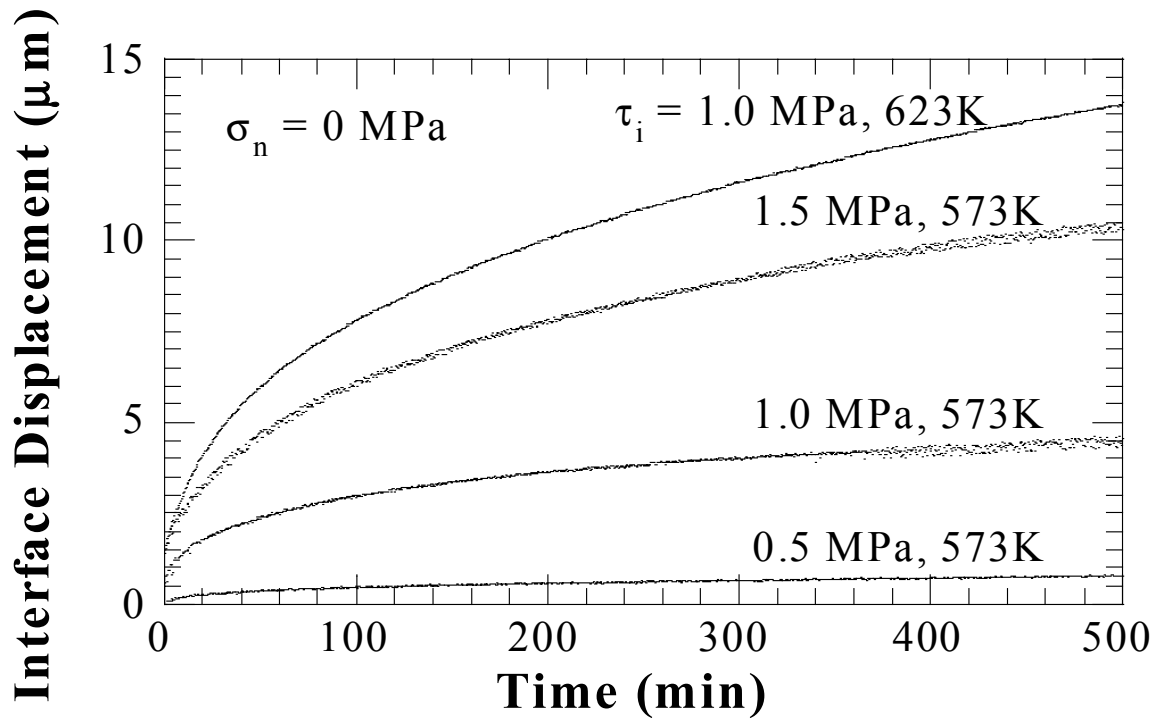


Figure 24. Example Interfacial Creep Curves at Various Shear Stresses and Temperatures.

The first set of experiments were conducted using samples which had a 1 $\mu$ m finish on both sides of Si (scratches running the same direction,  $h \approx 18\text{nm}$ ) in the sandwich structure with no normal stress applied during creep testing while varying only the temperature and applied shear stress ( $\tau_i$ ). Figure 25a shows a plot of the average interfacial displacement rate ( $\dot{\bar{U}}$ ) as a function of  $\tau_i$ . Over the entire temperature range of testing (0.45  $T_m$  - 0.72  $T_m$  of Al),  $\dot{\bar{U}}$  displays linear stress dependence, with the creep rate vanishing at zero interfacial shear stress ( $\tau_i=0$ ). Figure 25b shows the temperature compensated interface displacement rate ( $\frac{\dot{\bar{U}}kT}{\exp^{-Q/RT}}$ ) as a function of  $\tau_i$  also showing

(1) a linear shear stress dependence, (2) negligible threshold stress when no normal stress is applied, and (3) Arrhenius type of behavior [101], in agreement with Equation 5.1. Figure 26a shows a plot of  $\ln \dot{\bar{U}}$  vs.  $1/T$  for applied stress levels ranging from 0.25 to 2 MPa. All the curves yield the same nominal slope, yielding an apparent activation energy ( $Q_{app}$ ) of  $\sim 42$  kJ/mole for all testing conditions. In addition, Figure 26b shows the temperature and interfacial shear stress compensated interface displacement rate ( $\ln \frac{\dot{\bar{U}}kT}{\tau_i}$ ) as a function of  $1/T$  (relationship shown in Equation 5.1) revealing the same activation energy as before ( $\sim 42\text{kJ/mol}$ ). Clearly, the same mechanism of interfacial creep operates over the entire test range ( $T/T_m$  of 0.45-0.72 and  $\tau_i/G$  of  $\sim 2 \times 10^{-5}$  to  $2 \times 10^{-4}$  with respect to shear modulus of Al). The observed linear stress dependence and the low  $Q_{app}$  are in nominal agreement with Equation 5.1, where the normal interfacial stress is zero in these experiments ( $\sigma_n=0$ ).



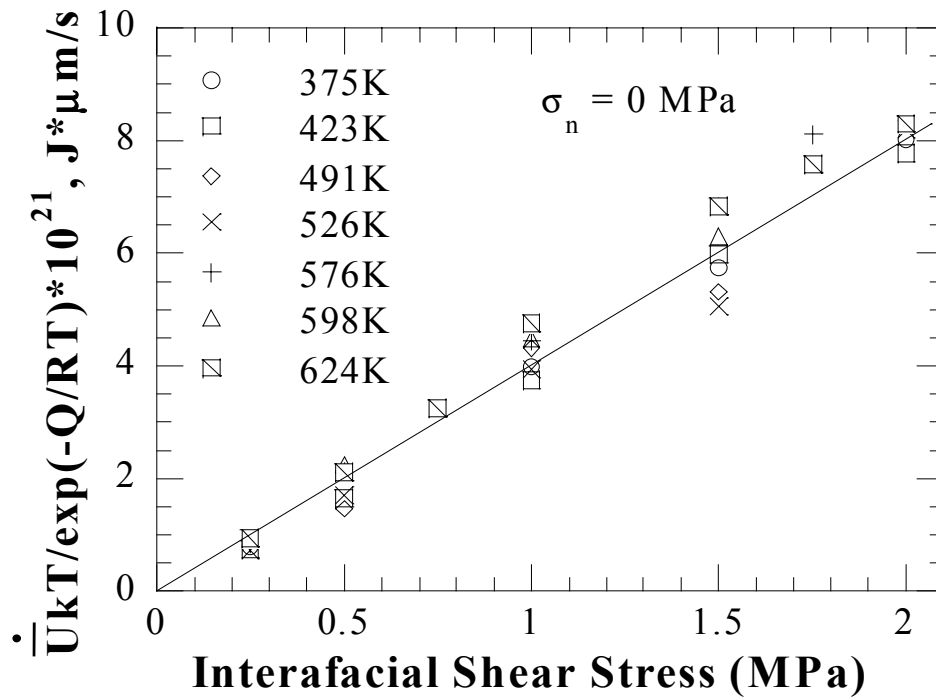
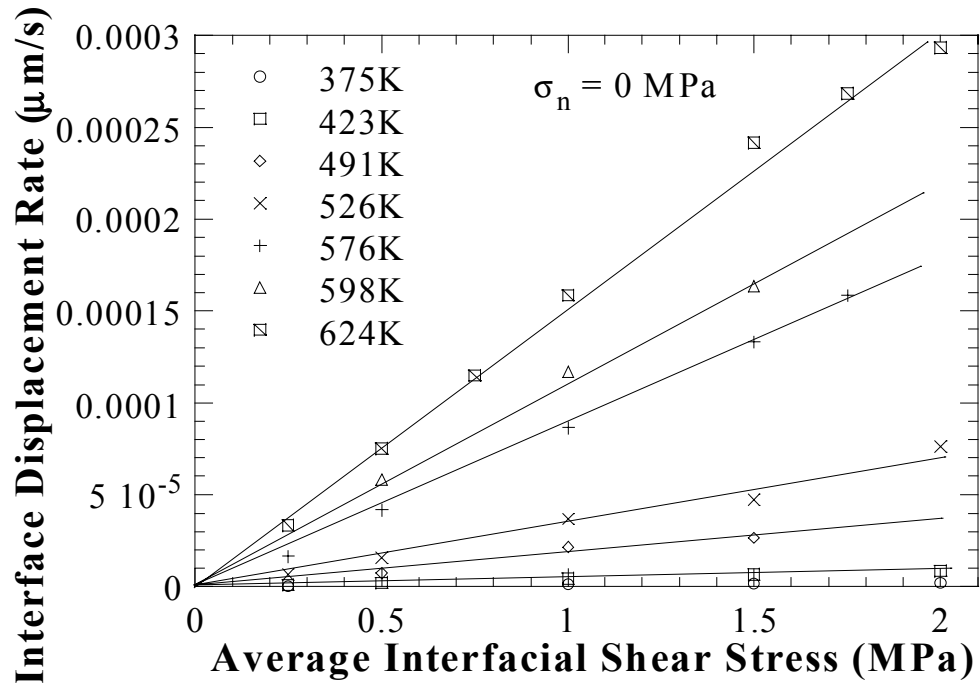


Figure 25. Plots (a) and (b) Showing Linear Stress Dependence of Interfacial Displacement Rate. Plot (b) Showing Temperature Normalized Displacement Rate as a Function of Interfacial Shear Stress.

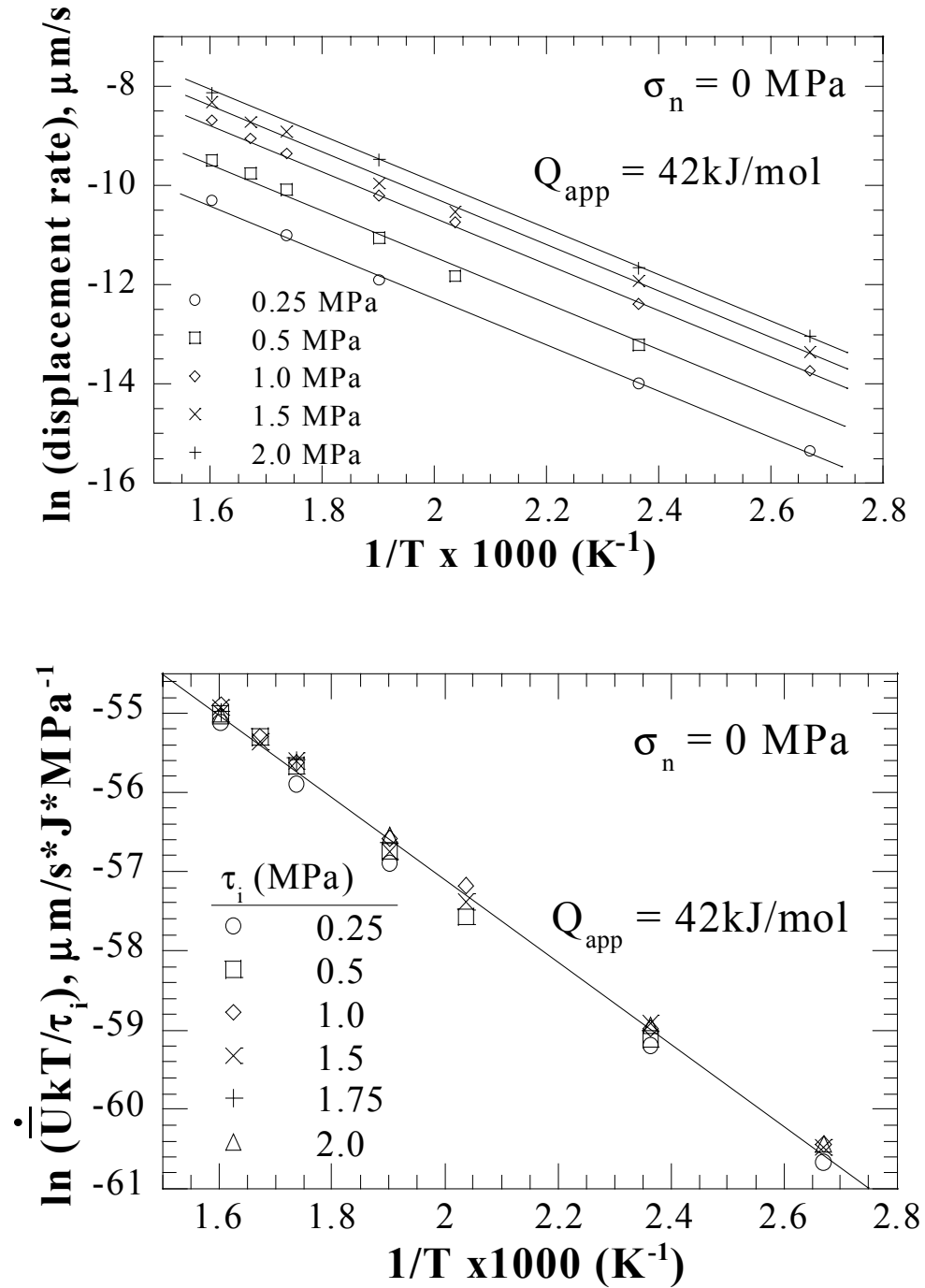


Figure 26. Plot (a) Showing Arrhenius Temperature Dependence of Interfacial Displacement Rate, with an Apparent Activation Energy of  $\sim 42 \text{ kJ/mol}$ . Plot (b) Showing Arrhenius Temperature Dependence and Same Activation Energy of  $\sim 42 \text{ kJ/mol}$ .

Since Si is not expected to display creep at the relevant temperatures, the measured deformation occurs either at the interface or in a narrow band of Al immediately adjacent to the interface. However, under the conditions of interest, grain boundary diffusion controlled Coble creep would be the only mechanism yielding measurable strain rates in Al [62]. While this would explain the observed linear stress dependence, it would yield an activation energy value commensurate with that of grain boundary diffusion in Al, i.e.,  $Q_{gb} \approx 84 \text{ kJ/mole}$ , which is about twice the value of  $Q_{app}$ . Furthermore, given that the grain sizes in Al immediately adjacent to the interface were  $\sim 20\text{-}80 \mu\text{m}$  (Figure 14), Coble creep would not result in the very narrow deformation band indicated by Figure 23. Besides, the Coble creep rate of Al over most of the test conditions would be  $\sim 10^{-10} - 10^{-8} / \text{s}$ , far below the equivalent strain rates of  $\sim 10^{-3} / \text{s}$ , which may be estimated assuming that Al deforms within a  $\sim 0.1 \mu\text{m}$  thick band next to the interface. Figure 27 is one of many scanning electron micrographs (SEM) that show a Si-Al step after significant interface sliding has occurred. SEM with Orientation Imaging Microscopy (OIM) and optical observations show that no lattice curvature or deformation transpired in the Al matrix near the interface. These observations provide evidence that all the creep deformation was confined to the interface, negligible deformation occurred in either Si or Al, and no evidence of interfacial de-bonding was observed. Again, the experimental approach is able to isolate and measure interfacial creep displacements.

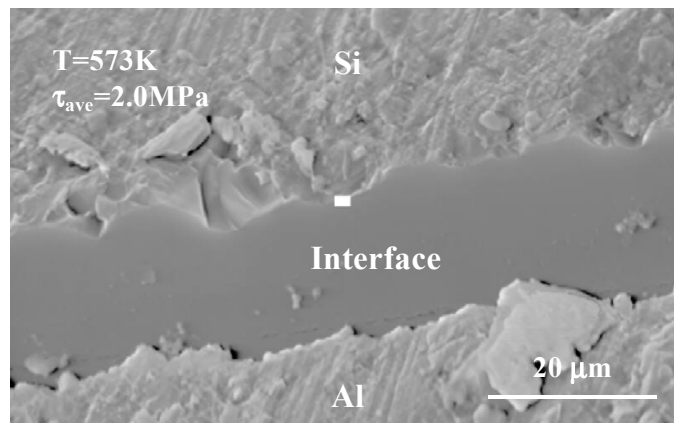


Figure 27. SEM Micrograph at a  $45^\circ$  Tilt Showing Al-Si-Al Specimen Bottom that Underwent Interfacial Creep at 573K and 2MPa. The Sample Shown Has a PVD Al Film of  $\sim 500 \text{ nm}$ .

The second set of experiments also used sandwich specimens with a  $1\mu\text{m}$  finish on the Si ( $h \approx 18\text{nm}$ ), but allowed the normal stress to vary along with temperature and interfacial shear stress. Typical creep curves obtained for three interfacial normal stresses ( $\sigma_n$ ) while holding temperature ( $T=623\text{K}$ ) and interfacial shear stress ( $\tau_i=1.0\text{MPa}$ ) constant are shown in Figure 28. The duration of the primary interfacial creep appears to diminish along with the secondary interfacial creep rate (minimum slope of the creep curve  $\dot{\bar{U}}$ ) proportional to the increase of applied normal stress ( $\sigma_n$ ). When the normal stress is relieved ( $\sigma_n = 0$ ) and only an interfacial shear stress ( $\tau_i$ ) is present, the steady state interfacial creep rate is re-established to the original rate ( $\dot{\bar{U}} \approx 1.5 \times 10^{-4} \mu\text{m/s}$ ) as shown in Figure 28.

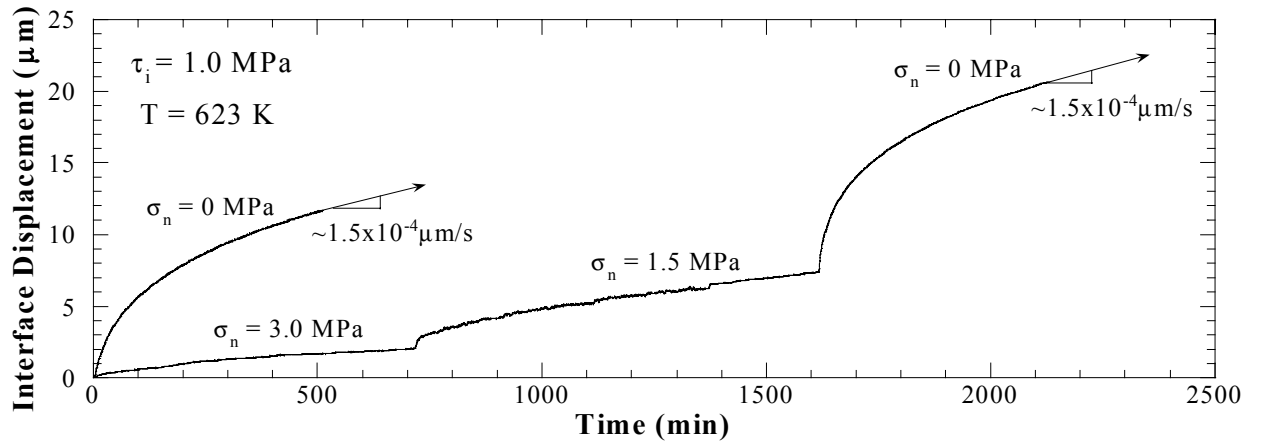


Figure 28. Interface Displacement Over Time Showing Interface Displacement Increases with Decreasing Applied Interfacial Normal Stress at a Constant Temperature (623K) and Interfacial Shear Stress ( $\tau_i = 1.0\text{MPa}$ ).

Figures 29 and 30 show plots of the average interfacial displacement rate ( $\dot{\bar{U}}$ ) as a function of  $\tau_i$  at 623K, 523K, and 423K, with various levels of applied normal compressive stresses ( $\sigma_n = 0, -0.6, -1.5, \text{ and } -3.0\text{MPa}$ ). When a compressive  $\sigma_n$  is applied to the interface, the interfacial displacement rate ( $\dot{\bar{U}}$ ) decreases at a given  $\tau_i$  because the effective shear stress ( $\tau_{\text{eff}}$ ) is decreased. Figures 29 and 30 still show a linear shear stress dependence, and an apparent threshold shear stress  $\tau_0$  below, which no creep occurs. The

threshold stress  $\tau_0$  increases with increasing magnitudes of applied  $\sigma_n$ . For each of the three temperatures in Figures 29 and 30,  $\sigma_n = 0$  produces  $\tau_0 = 0$ , whereas compressive normal stresses ( $\sigma_n$ ) of increasing magnitudes produce increasingly larger threshold stresses ( $\tau_0$ ). According to Funn and Dutta [3],  $\tau_0$  is given by:

$$\tau_0 = 2\pi^3 \left( \frac{h}{\lambda} \right)^3 \sigma_n \quad (5.3)$$

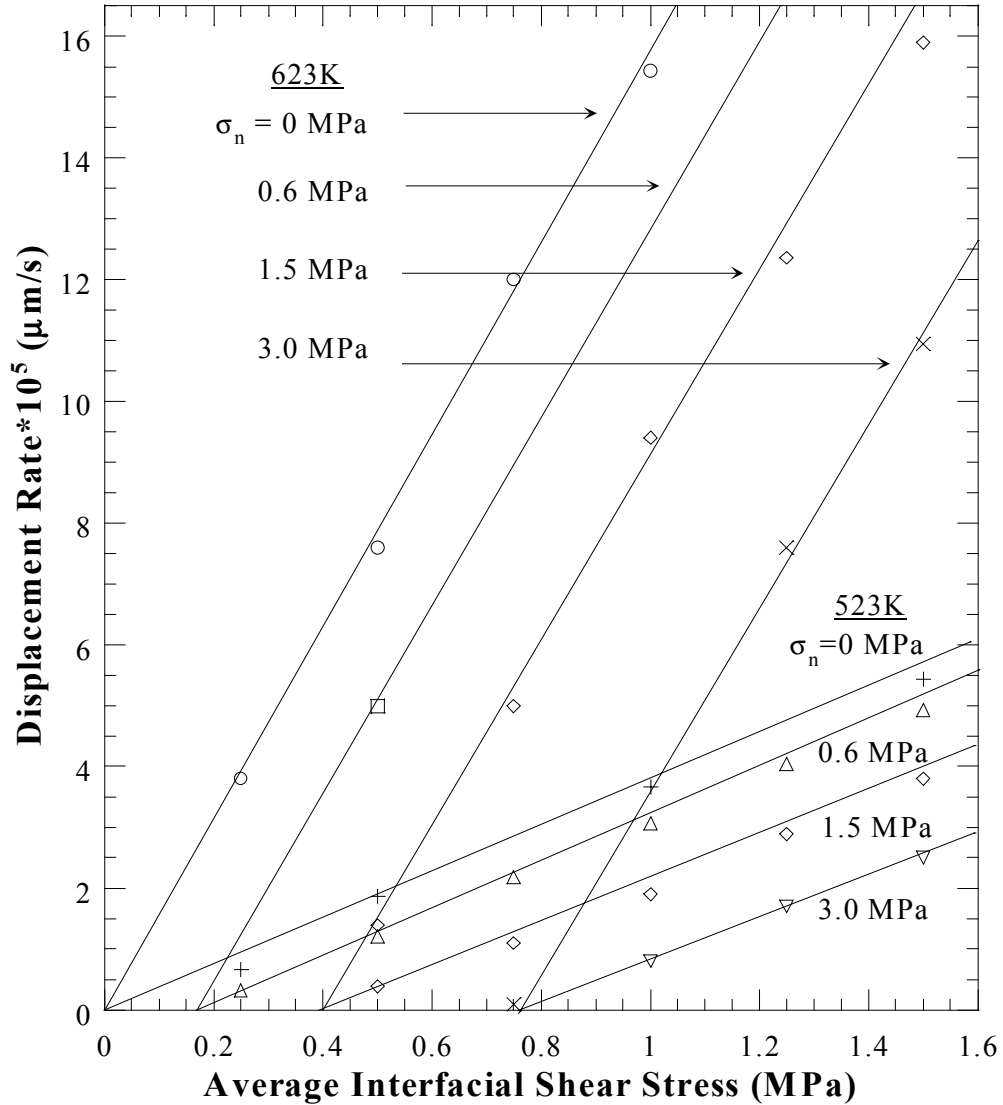


Figure 29. Interface Displacement Rate as a Function of Interface Shear Stress Showing Linear Stress Dependence with Corresponding Threshold Stress for Four Applied Interfacial Normal Stresses at 623K and 523K.

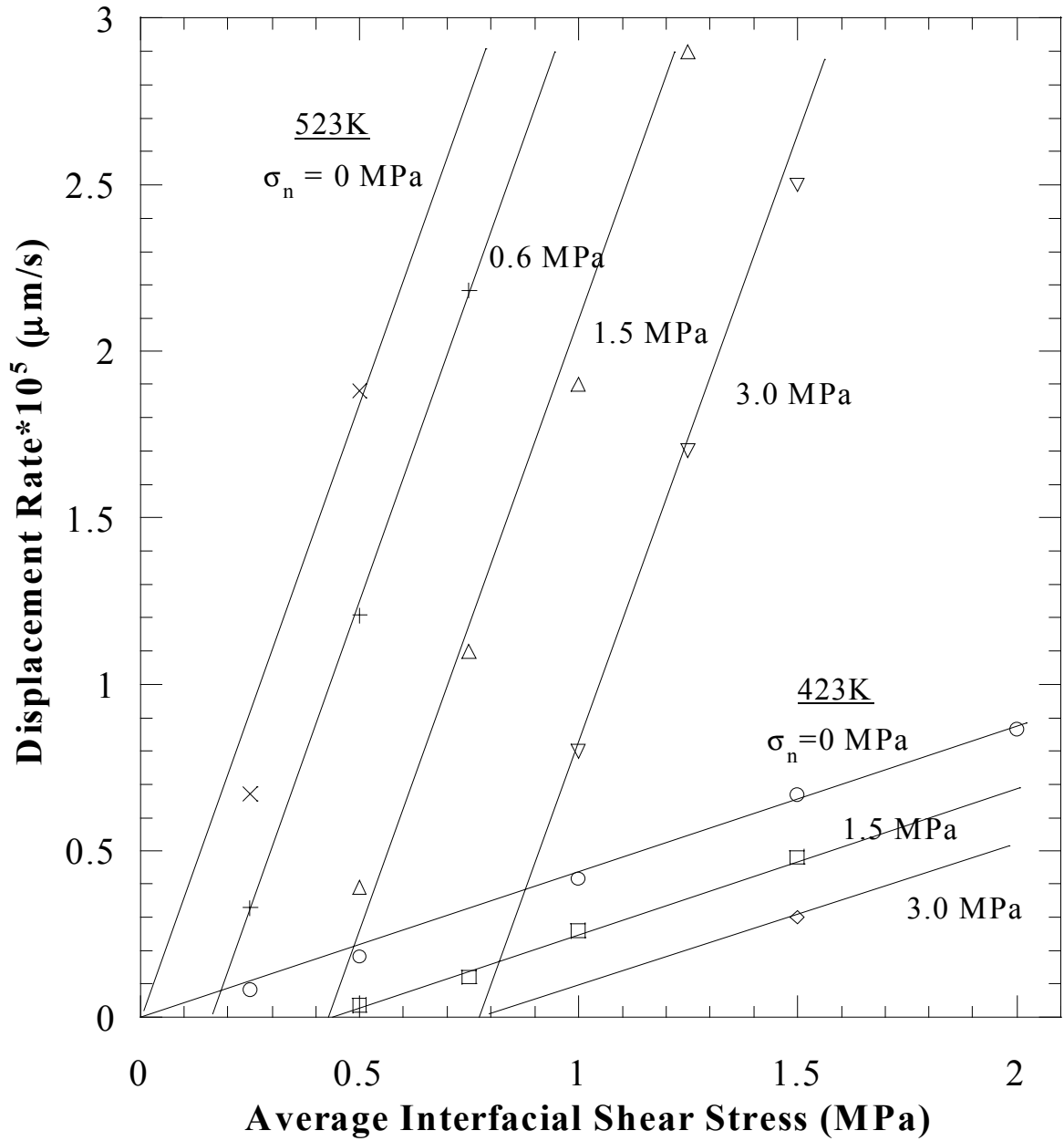


Figure 30. Interface Displacement Rate as a Function of Interface Shear Stress Showing Linear Stress Dependence with Corresponding Threshold Stress for Four Applied Interfacial Normal Stresses at 523K and 423K.

Therefore, a negative  $\sigma_n$  (i.e., a negative  $\tau_o$ ) serves to reduce the effective shear stress ( $\tau_{eff} = \tau_i + \tau_o$ ) acting on the interface, thus reducing the creep rate as observed in Figures 28 - 30. Clearly, the experimental data validates the dependence of the interfacial displacement rate on the applied normal stress, as well as the physical origin of the observed threshold stress  $\tau_o$ , proposed in Equations 5.1 and 5.3. Figure 31 shows temperature compensated interfacial displacement rate  $\frac{\dot{U}kT}{\exp(-Q/RT)}$  as a function of  $\tau_i$

with an applied normal stress ( $\sigma_n$ ) of 0, -0.6, -1.5, and -3.0MPa. The plot still shows a linear shear stress dependence along with a threshold stress, which remains in agreement with Equation 5.1. The threshold stress was carefully determined for each normal stress applied to the interface ( $\tau_o \approx 0$  MPa for  $\sigma_n \approx 0$  MPa,  $\tau_o \approx -0.16$  MPa for  $\sigma_n \approx -0.6$  MPa,  $\tau_o \approx -0.39$  for  $\sigma_n \approx -1.5$  MPa, and  $\tau_o \approx -0.77$  MPa for  $\sigma_n \approx -3.0$  MPa). By taking the ratio of the apparent threshold stress ( $\tau_o \approx -0.16, -0.39, -0.77$  MPa) over the applied normal stress ( $\sigma_n \approx -0.6, -1.5, -3.0$  MPa respectively) and constants ( $h/\lambda = \sqrt[3]{\tau_o/2\pi^3\sigma_n}$ ), a roughness ratio  $h/\lambda$  of about 0.16 was calculated for all the three normal stresses, which is in agreement with the AFM measurements (Figure 20) for specimens with a 1 $\mu$ m polish on the surface of Si ( $h \approx 18$ nm). This  $h/\lambda$  value yields a threshold stress, which is approximately 26% of the applied shear stress (i.e.,  $\frac{\tau_o}{\sigma_n} = 2\pi^3\left(\frac{h}{\lambda}\right)^3 \approx 0.26$ ). Figure 32

shows temperature and effective shear stress ( $\tau_{eff}$ ) compensated interfacial displacement rate ( $\ln \frac{\dot{U}kT}{\tau_{eff}}$ ) versus  $1/T$  yielding the same nominal slope as before with an apparent activation energy ( $Q_{app}$ ) of  $\sim 42$  kJ/mole for all testing conditions, where  $\tau_{eff} = \tau_i - \tau_o$ . The apparent mechanism has not changed with the presence of the applied normal stress. The interface displacement rate ( $\dot{U}$ ) dependence on interfacial temperature, shear, and normal stresses is in agreement with Equation 5.1.

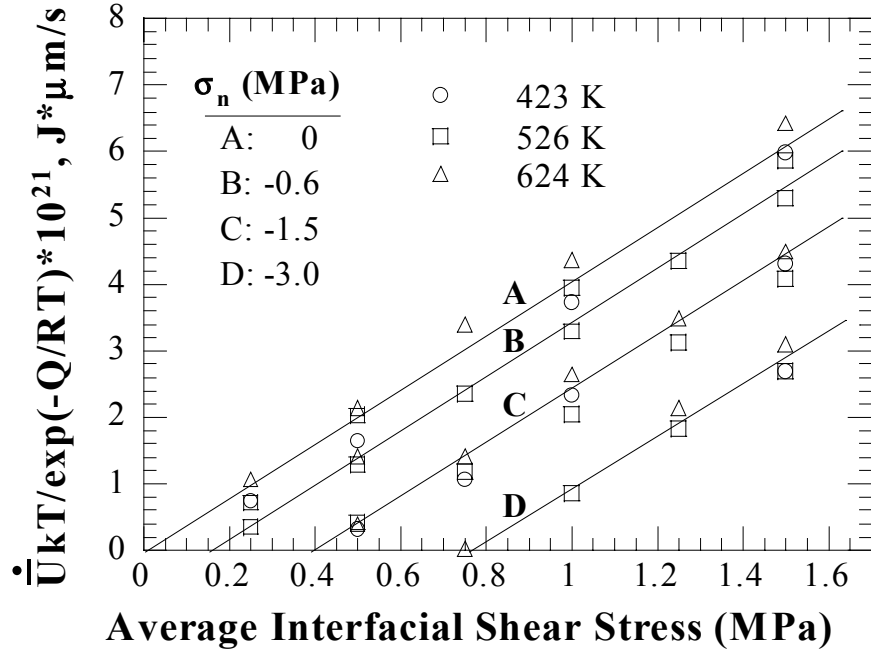


Figure 31. Temperature Normalized Interface Displacement Rate Showing Linear Stress Dependence with Corresponding Threshold Stress for Four Applied Interfacial Normal Stresses.

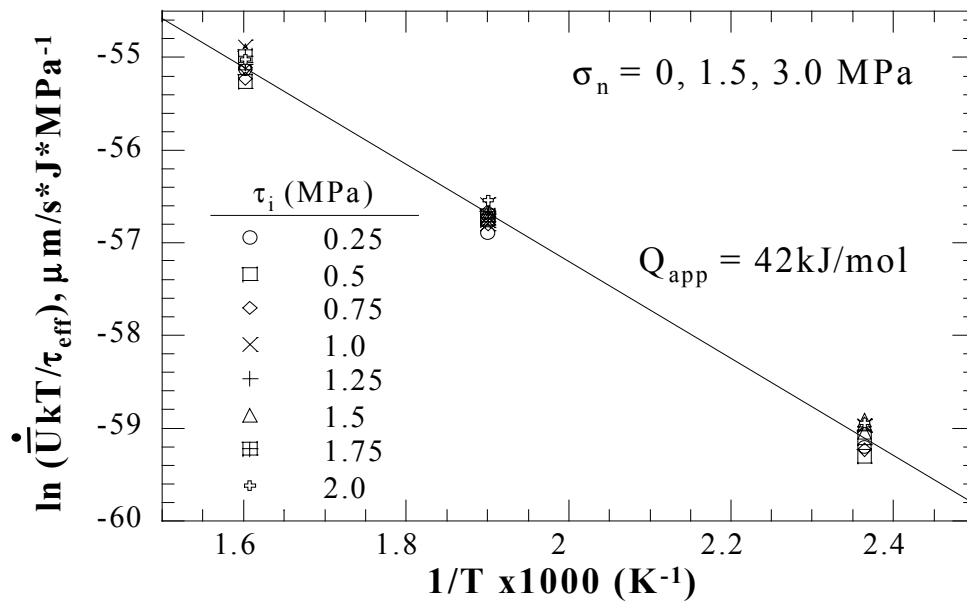


Figure 32. Interfacial Shear Stress and Temperature Normalized Interface Displacement Rate Showing Arrhenius Temperature Dependence with an Apparent Activation Energy of  $\sim 42 \text{ kJ/mol}$  with Applied Interfacial Normal Stress.



The third set of experiments varied the surface roughness of the Si in the sandwich structure (Al-Si-Al) and the applied interfacial shear stress ( $\tau_i$ ) while holding the temperature (624K) constant with no applied normal stress ( $\sigma_n = 0$ ). Figure 33 shows typical creep curves for three interfacial roughnesses  $h \approx 18, 54, \text{ and } 174 \text{ nm}$ , (corresponding to the final polishing 1, 5, and  $17\mu\text{m}$  on Si) at 624K with applied stresses of  $\tau_i = 1.5 \text{ MPa}$  and  $\sigma_n = 0$ . The duration of the primary creep regime and the secondary creep rate appear to decrease to the increase in interfacial roughness. Figure 34 shows the interfacial displacement rate ( $\dot{U}$ ) as a function  $\tau_i$  with no applied normal stress ( $\sigma_n = 0$ ) for three interfacial roughness ( $h \approx 18, 54, \text{ and } 174\text{nm}$ ). All three sets of specimens with different interfacial roughness display a linear stress dependence with no apparent threshold stress ( $\tau_o=0$ ) along with the interfacial displacement rate diminishing to zero as  $\tau_i$  approaches zero. Figure 35a shows the interfacial displacement rate ( $\dot{U}$ ) as a function of the inverse of interfacial roughness squared ( $1/h^2$ ), determined from Figure 20 as a function of the final grit size used to polish Si. The plot shows the interfacial displacement rate behaves parabolic as a function of surface roughness  $\dot{U} \propto 1/h^2$ . It is important to note that the interface displacement rate dependence on the interfacial roughness is greater than that of interfacial shear stress ( $\dot{U} \propto 1/h^2$  versus  $\dot{U} \propto \tau_i$ ). Figure 35b is a plot of the normalized displacement rate ( $\dot{U}/\tau_i$ ) as a function of  $1/h^2$  (interface roughness), showing that all specimens tested behave in accordance with Equation 5.1.

The fourth set of experiments varied the surface roughness of the Si (as above) along with applying a normal stress ( $\sigma_n \neq 0$ ) while varying the applied interfacial shear stress at a given temperature (624K). Figure 36 shows the interfacial displacement rate ( $\dot{U}$ ) as a function of  $\tau_i$ . The plot shows a linear shear stress dependence for all interfacial roughnesses and applied normal stresses ( $\sigma_n$ ). The apparent threshold stress (where the interface displacement rate diminishes to zero) increases with increasing interfacial roughness and applied normal stress ( $\tau_o \propto \sigma_n$  and  $\tau_o \propto (h/\lambda)^3$ ).

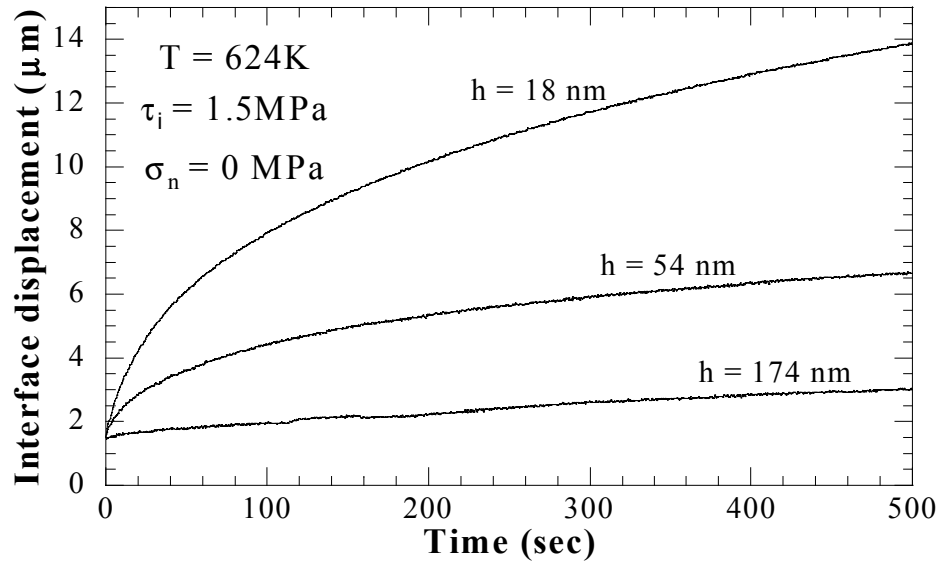


Figure 33. Typical Interfacial Creep Curves at 624K with an Applied Interfacial Shear Stress of 1.5MPa for Three Interfacial Roughnesses ( $h \approx 18, 54$ , and  $174\text{nm}$ ) with No Interfacial Normal Stress. Plot Shows an Increase in Interface Displacement for Smoother Surfaces.

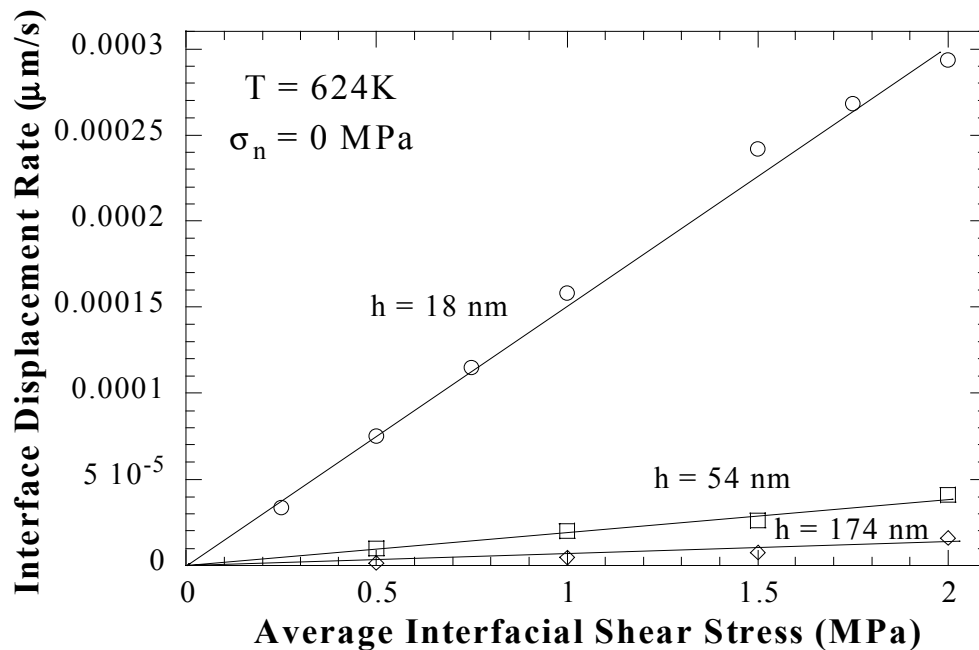


Figure 34. Interfacial Displacement Rate as a Function of Applied Average Interfacial Shear Stress with No Interfacial Normal Stress Applied for Three Interfacial Roughnesses ( $h \approx 18, 54$ , and  $174\text{nm}$ ). The System Exhibits Linear Stress Dependence with No Threshold Stress.

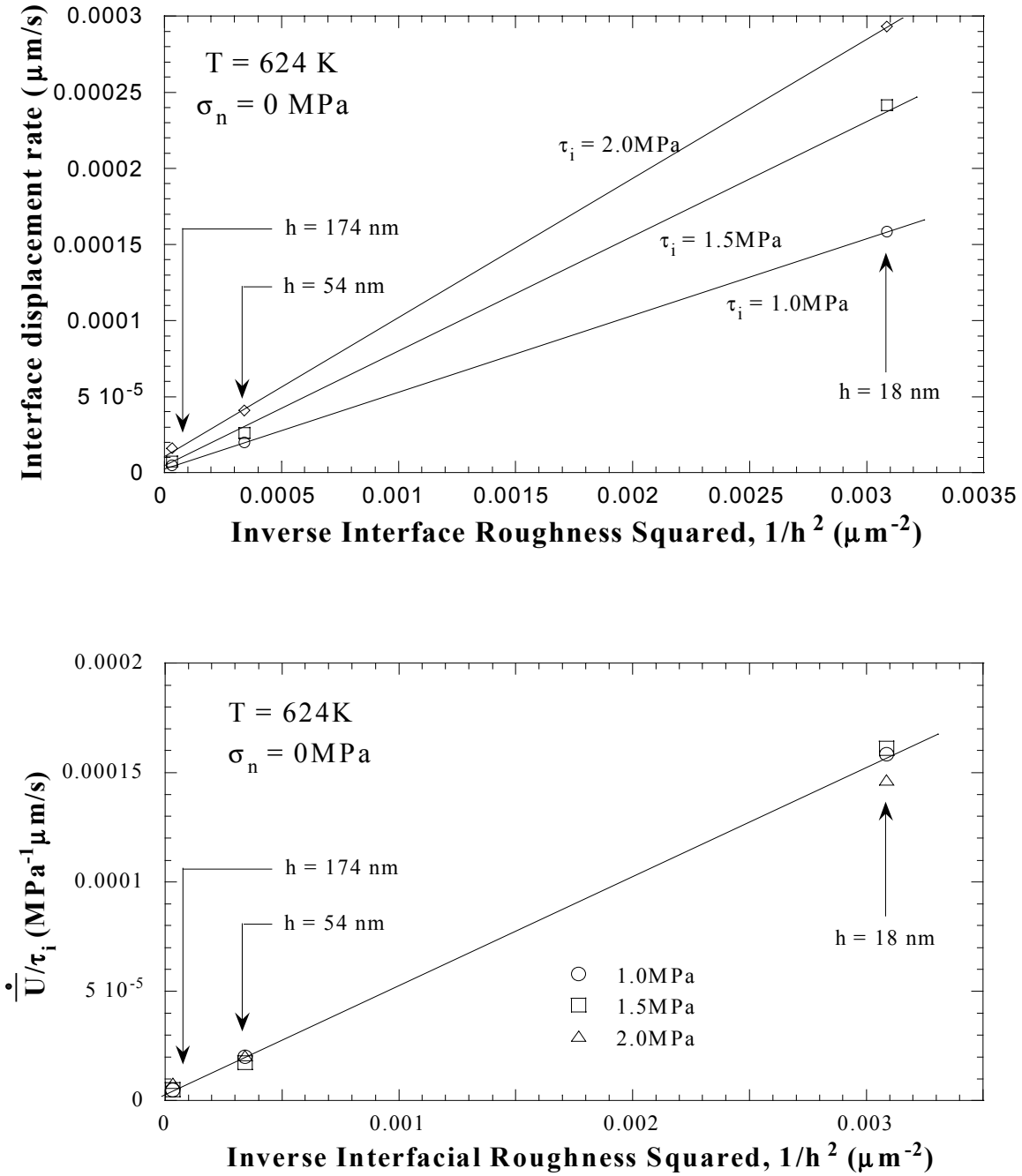


Figure 35. (a) Interfacial Displacement Rate as a Function of the Inverse of Interfacial Roughness Showing Squared Showing an Increase in the Interfacial Displacement Rate as the Applied Interfacial Shear Stress Increases for all Interfacial Roughnesses and (b) Interfacial Shear Stress Normalized Displacement Rate Plot is in Agreement with Interfacial Sliding Equation 5.1.

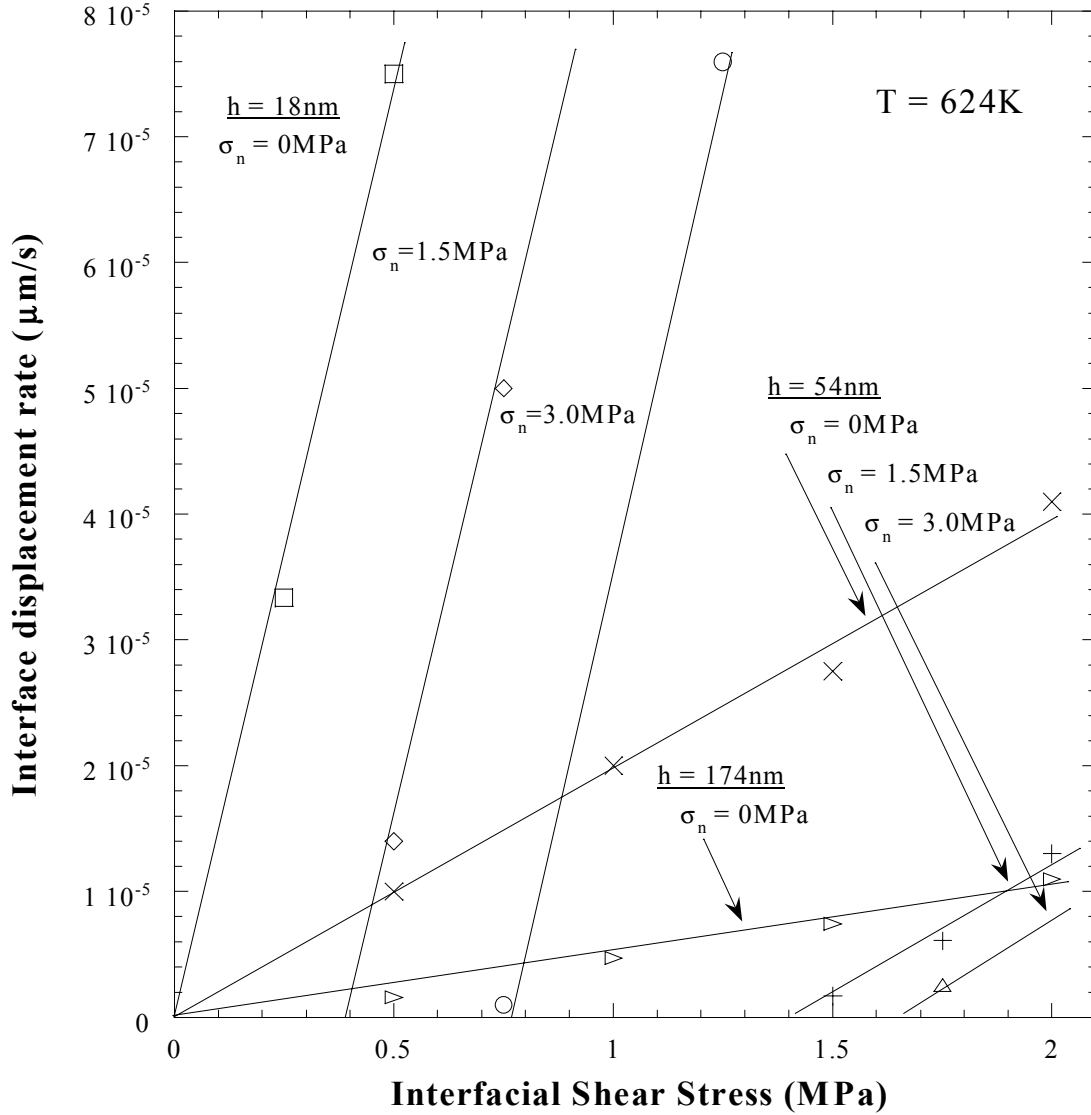


Figure 36. Interfacial Displacement Rate as a Function of Applied Interfacial Shear Stress When an Normal Stress is Applied Showing a Linear Shear Stress Dependence with an Observed Threshold Stress. Observed Threshold Stress Increases with Increasing Applied Interfacial Normal Stress and Interfacial Roughness.

#### D. DISCUSSION

Interfacial creep has been thought to occur in several systems (including dispersion strengthened metals [26, 33, 34], eutectic alloys [36], intermetallics [38], composites [39-41], and film-substrate interfaces [13]), although its kinetics have usually been deduced from the overall system response, instead of being measured directly. Not

surprisingly, there is as yet no consensus on the mechanism of interfacial sliding. However, by examining the literature, one can conclude that there are two situations where interfacial creep may occur with little or no matrix deformation, as in this study.

First, interfacial sliding may occur by diffusional creep [3, 32]. When the interface acts as a perfect source and sink of vacancies, e.g., due to an abundance of mobile boundary dislocations (BDs), the stress exponent  $n=1$ , and  $Q$  equals that for either boundary or lattice diffusion, and the process is "diffusion controlled" [26, 32]. When the density of mobility of dislocations in the boundary is limited, on the other hand, the kinetics of sliding are believed to become "interface reaction controlled," resulting in  $n \sim 2$ , a threshold stress corresponding to the minimum stress required to move BDs, and a high activation energy associated with rearranging atoms on the more refractory/stiffer side of the interface [26, 33]. However, in the present study,  $n=1$ ,  $Q$  is low, and a threshold stress is not observed, suggesting that the observed sliding is not interface-reaction controlled.

Another mechanism which would lead to  $n \approx 1$  is cooperative glide of intrinsic interface dislocations (ID), which has been thought to cause sliding at  $\gamma/\alpha_2$  phase boundaries in TiAl in the low stress / intermediate temperature regime [38]. Here, the glide rate is thought to be limited by climb of sessile jogs and/or solute drag from interstitial impurities on the interface plane, giving rise to a thermally activated process.

Based on the above, the data obtained here could be rationalized by either diffusion-controlled diffusional creep or viscous glide of interface dislocations. A clear understanding of the structure of the interface is therefore necessary to identify the operative mechanism of interfacial creep. High-resolution electron microscopy (HREM) of the interface revealed that an amorphous layer, ranging in thickness from  $\sim 20$  to  $100\text{nm}$ , was present at the Al-Si interface. Figure 37 shows HREM images of the Si and Al sides of the interface, respectively, along with the computed fast Fourier transforms (FFT) of the lattice images. The Si side of the interface displays a relatively sharp transition to the amorphous region, which is situated almost entirely on the Al side, showing a gradual transition to crystalline Al. This is clear from the FFT pattern from

the apparently crystalline part of Al, which shows that the spots due to the lattice planes are superimposed by a diffuse intensity due to the amorphous character. Energy dispersive X-ray spectroscopy (EDXS) confirmed that the amorphous layer is primarily Al with a high (non-equilibrium) amount of dissolved oxygen. Amorphous layers on the order of a few to several tens of nanometers thick are frequently observed at interfaces in both bulk and thin film systems with either Al/Al<sub>2</sub>O<sub>3</sub> or Si/SiC on one side [70, 72, 73, 78]. This is typically associated with adsorbed oxygen and/or nascent oxide layers on the surfaces of Si and Al [70], consistent with the high oxygen concentration observed in the present work.

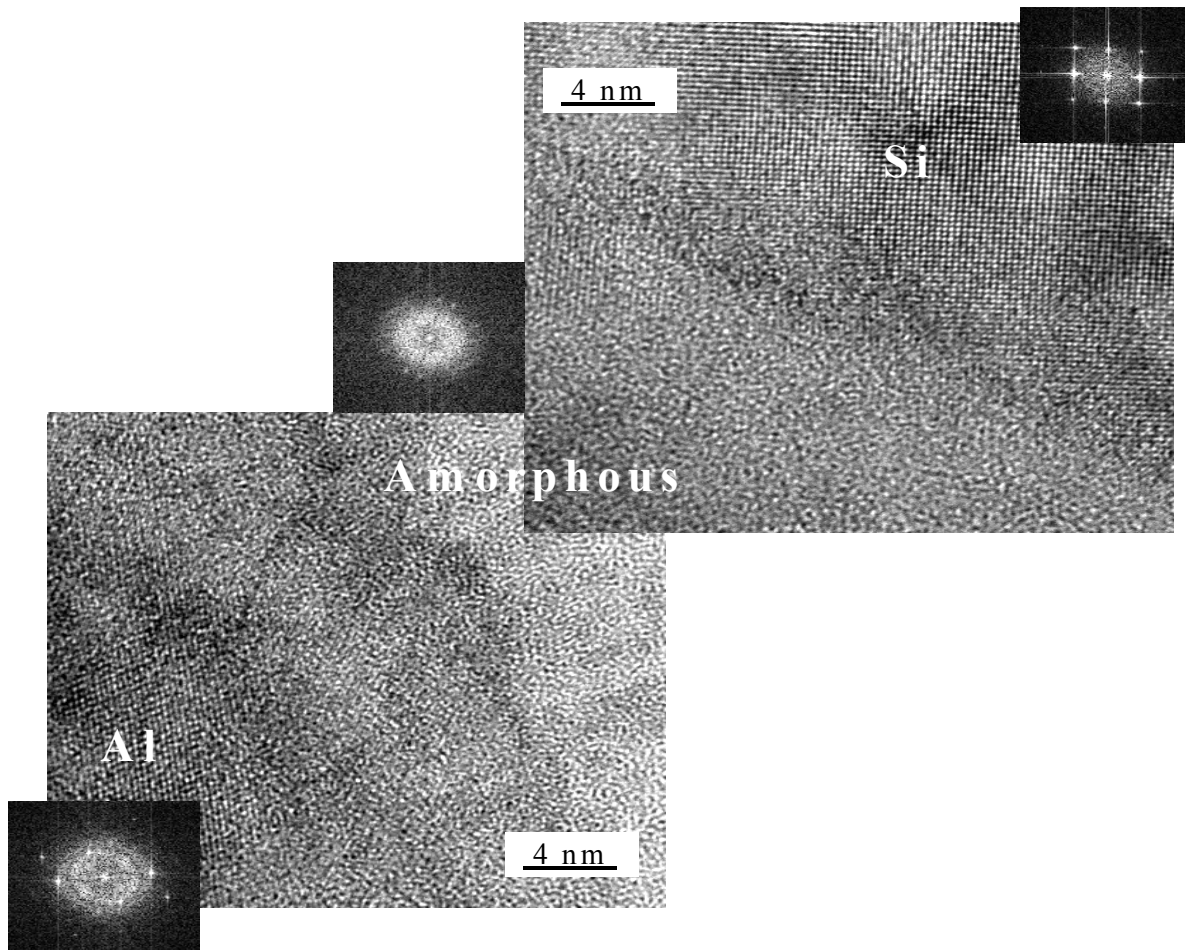


Figure 37. HREM Micrograph Showing Lattice Image of the Single Crystal Si, a Sharp Interface Between the Si and the ~40nm Thick Amorphous Region, and a Gradual Transition from the Amorphous Region to the Al Crystal Before Creep Testing.

The presence of the amorphous interfacial layer suggests that the dislocation-based viscous glide model suggested in Reference 78 is not applicable here. Further, the  $Q$  values obtained in the present experiments are not consistent with either climb of jogs (which would produce  $Q \approx Q_{\text{vol}}$  for Al = 142kJ/mol), or solute diffusion ( $Q \approx Q_{\text{Si in Al}} \sim 123\text{-}136$  kJ/mol) [74], which would be needed for glide of interfacial dislocations. It is therefore proposed that the mechanism of interfacial sliding in the present studies is 'interface diffusion-controlled' diffusional creep, identical to that observed in Reference 3. The interfacial roughness results in a periodically varying normal stress at the interface, which drives diffusive flux of Al through the interface, producing a relative displacement of Si and Al [3, 32]. The specific path of interfacial diffusion is not clear, but may be surmised from the observed  $Q$  value of  $\sim 42\text{kJ/mole}$ .

Creep studies conducted on several amorphous Al alloys [79] have shown that below the glass transition temperature  $T_g$ , creep occurs by diffusional flow of Al in the glass with  $Q \approx 24 - 45$  kJ/mol, whereas above  $T_g$ , deformation occurs by viscous flow of the supercooled liquid with  $Q \approx 188 - 328$  kJ/mole. This is consistent with the hypotheses that diffusional flow below  $T_g$  occurs by fast atomic diffusion through a relatively open amorphous structure leading to a low  $Q$ , whereas viscous flow above  $T_g$  requires movement of volumes of short-range ordered atoms in the supercooled liquid past other such volumes, producing a higher  $Q$  [80, 81]. The  $Q$  value of  $\sim 42$  kJ/mole obtained in the present study is consistent with solid-state diffusion of Al in amorphous Al below  $T_g$ , and therefore it is inferred that even at the highest testing temperature,  $T_g$  of the interfacial layer is not exceeded. An interfacial sliding mechanism based on viscous flow of the amorphous phase above  $T_g$  may be further discounted, realizing that this can only occur when the interfacial roughness is significantly smaller than the amorphous layer thickness; a condition which is not valid for the present samples.

In previous work by Funn and Dutta [3], the kinetics of interfacial sliding at fiber-matrix interfaces is described by a flow law with  $n=1$  and a threshold stress (Bingham flow). The studies were based on two model SFC systems - one with limited mutual solubility (Pb-matrix/Ni fiber) and the other with no mutual solubility (Pb-matrix/quartz fiber). Both systems displayed a low  $Q$  value ( $Q < Q_{\text{gb}}$  for Pb) and a stress exponent of 1,

based on which, the mechanism of sliding was thought to be interface diffusion-controlled diffusional creep. The low  $Q$  value, along with the small-applied shear stresses, precluded a dislocation climb based rationalization of the observed sliding.

Further, scanning electron microscopy (SEM) of the interface revealed a periodic topography, consistent with the notion of local normal stress variation along the interface due to a globally applied shear stress, as considered in the classical model for grain boundary sliding [26]. The classical model was modified to incorporate a global normal stress (in addition to the applied shear) in order to account for the effect of radial stresses which arise from CTE / Poisson's ratio mismatch between the fiber and matrix, and it was shown that the kinetics of sliding was represented as follows:

$$\dot{\bar{U}} = \frac{2D_m^{\text{eff}} \Omega \lambda}{kT \pi h^2} \left[ \tau_i + \left( \frac{\pi h}{\lambda} \right)^3 \sigma_n \right] + \frac{4\delta_i D_i \Omega}{kTh^2} \left[ \tau_i + 2 \left( \frac{\pi h}{\lambda} \right)^3 \sigma_n \right] \quad (5.4)$$

where  $\tau_i$  is the shear stress acting on the interface,  $D_m^{\text{eff}}$  and  $D_i$  are the effective matrix and interface diffusivities, respectively,  $\Omega$  is the atomic volume of the diffusing species (matrix),  $\delta_i$  is the thickness of the interface,  $\lambda$  and  $h$  are the periodicity and width (i.e., twice the amplitude), respectively, of the interface, and  $\sigma_n$  is the normal (radial) stress acting on the interface. When  $D_m^{\text{eff}} \ll D_i$ , the first term in Equation 5.4 is negligible, and  $\dot{\gamma}_i$  can be simplified as:

$$\dot{\bar{U}} \approx A_i (\tau_i + \tau_o) = A_i (\tau_{\text{eff}}) \quad (5.5)$$

Here  $\tau_o$ , the contribution of the interfacial normal stress to sliding, is given by:

$$\tau_o = 2\pi^3 \left( \frac{h}{\lambda} \right)^3 \sigma_n \quad (5.6)$$

and

$$A_i = \frac{4\delta_i D_i \Omega \lambda}{kTh^2} \exp \left[ -\frac{Q_i}{RT} \right] \quad (5.7)$$



where  $Q_i$  and  $D_{i0}$  are the activation energy and frequency factor, respectively, for interfacial diffusion,  $k$  is Boltzmann's constant,  $R$  is the gas constant, and  $T$  is the absolute temperature.

To date, the experimental data for the Al-Si-Al system supports the findings by Funn and Dutta [3] in four aspects. First, the continuum model proposed by Funn and Dutta (Equations 5.4 to 5.7) remains adequate to describe interfacial sliding for planar interfaces in the Al-Si-Al system. Second, the experimental data supports the theory that the threshold stress, below which no creep occurs, predominately originates from the normal stress acting on the interface. Third, the apparent activation energy is quite low compared to the activation energy for volume and grain boundary diffusion in the system supporting the theory that a fast diffusion path exists along the interface. Fourth, the interface-sliding rate and threshold stress strongly depend on interfacial roughness.

Interface sliding must be accommodated by removal/addition of material from the mating surfaces, which allow the interlocked boundaries to slide past one another. This process requires the boundary to act as a source or sink for diffusional flux of atoms and diffusional transport to occur through or along the adjoining crystals. Because most interfaces have significant lattice strains at the interface and possibly other defects due to various bonding processes, the interface acts as a perfect source or sink. Since the rate of emission/absorption of atoms is much faster than the rate at which the atoms can diffuse between sources/sinks, the process of interface sliding is likely “diffusion-controlled” versus “interface-controlled” [26].

In considering diffusion at interfaces, two major processes can be noted: (1) diffusion along the interfaces and (2) diffusion transverse, from, or to the interfaces. Interfaces and grain boundaries promote relatively fast diffusion along their cores known as “short-circuit diffusion.” Interfaces between two very different type of materials (i.e., Si and Al) may exhibit a higher density of coherency dislocations inside the interface which provide a faster short-circuit path [82] (boundary diffusivity varies linearly with the density of dislocations known as the “dislocation pipe model”) than a typical grain boundary. Literature also shows that the diffusivity increases as the disorientation of the

adjoining grains increases [83, 84], which may enhance the sliding rate. Generally, two species diffuse in the same boundary at different rates possibly allowing an even faster path for diffusion compared to diffusing along their own grain boundaries [82-86]. Additionally, species diffuse in boundaries at different rates for different type of bonding systems: metallic [55, 56], ionic [87-89], and covalent materials [55]. Fast diffusion along interfaces between dissimilar materials can become a very complex diffusion problem when multiple diffusion species are present at the interface. The literature has a span of results for a variety of different bonding systems, making it hard to deduce any one mechanism for interfacial diffusion which can accommodate interfacial sliding. However, the rate of interfacial diffusion depends strongly on the detailed atomistic structure of the interface [85, 90-92]. The interface can be thought as an array of discrete primary dislocations embedded in the crystal lattice adjacent to the interface. The cores of the dislocations consist of “bad material” wherein fast diffusion may generally occur [93] for sharp interfaces. For diffuse interfaces, the cores cover several atomic distances. According to St Venant’s principle, the stress field of the interface should decay over a distance comparable to the spacing between intrinsic interfacial dislocations from the interface. If the periodicity of the interface has a small amplitude (<10nm) and a small wavelength (<100nm), the difference in diffusivity between the interfacial diffusion (along dislocation cores) and the near interface lattice diffusion (distorted and strained array), may not be significantly different. If this is plausible, a wide diffusion path (large  $\delta_i$ ) is available, which may increase the overall flow of atoms along the interface.

The activation energy calculated from the experimental interfacial creep data is quite low (~42kJ/mol) compared to the volume and grain boundary diffusion for Al system ( $Q_v \approx 142$  kJ/mol and  $Q_{gb} \approx 84$  kJ/mol respectively) [62] and the activation energy for Si diffusing down grain boundaries of Al ( $Q_{Si \text{ in Al}} \approx 123-136$ kJ/mol) as previously discussed [74]. Since the activation is much lower than the reported activation energy for bulk and grain boundary diffusion of Al, it is assumed that the activation energy represents interfacial diffusion along the Si-Al interface. The low activation energy reveals that the interface is a diffusion path, which behaves much like a free surface. The low activation can be justified by three aspects: First, the small amorphous

layer (loose packed structure) that is present along the Si-Al interface acts as fast diffusion path. The amorphous layer is thicker than a typical grain boundary ( $\delta_i \gg \delta_{gb}$ ) allowing an even larger flow of atoms to occur at a rapid rate which is indicative of the fast interface displacement rate that is observed in the current experiment. Second, the interface can act as *extremely* fast diffusion path because the interfacial structure contains a higher concentration of vacancies than a typical grain boundary of Al. Although coherency strains and interfacial dislocations are not present at interfaces adjacent to amorphous layers, an even more open structure exists between the Si crystal and the amorphous layer as shown in Figure 37. Third, the transportation of atoms or vacancies along the interface to accommodate interfacial sliding when a shear stress is present can be explained using a model similar to the uncorrelated atom shuffling mechanism [85]. A sharp concentration gradient of Al across the Si-Al interface exists because of the interface is not only sharp mechanically but also chemically [77]. This causes a strong chemical potential to exist accompanied with a shear stress gradient across the interface due to an applied load during interfacial creep tests promoting atoms to de-bond from the Al matrix and diffuse into the interfacial region. Once the Al atoms diffuse into the interface toward the Si matrix, multiple competing diffusion paths exist (along the interface, back into the Al matrix, or into the Si lattice). The combination of the fast diffusion path and the applied shear stress along the interface sweep the Al atoms down the interface. As the atoms travel down the interface, the Al atoms may interact with the Si or Al side of the interface allowing yet another Al atom to de-bond and diffuse down the interface, continuing the cascading process. The fast diffusion path, which is assisted by a shear stress gradient across and down the interface, may account for the low activation energy and high interface-sliding rate. The diffusivity of the interface ( $\delta_i D_{oi}$ ) was calculated from Figures 25 and 26 as  $2 \times 10^{-20} \text{ m}^3/\text{s}$ . The interfacial diffusivity ( $\delta_i D_{oi}$ ) lies between grain boundary diffusivity ( $\delta_i D_{ogb} = 5 \times 10^{-14} \text{ m}^3/\text{s}$ ) and dislocation core diffusivity ( $a_c D_{oc} = 7 \times 10^{-25} \text{ m}^3/\text{s}$ ) for Al. The diffusion mechanism for Si atoms or diffusion into the Si matrix was neglected because the experiments were performed at low homologous temperatures of Si ( $0.22T_m - 0.37T_m$ ). Therefore, the diffusion of Si is too slow to account for the high diffusivity and low activation energy.

Before interfacial creep testing, HREM of the interface (Figure 37) revealed that an amorphous layer, ranging in thickness from ~20 to 100nm, was present at the Si/Al interface on the Al side where an intensely deformed interfacial band and a large concentration of solute impurities exist [77]. As previously discussed, the Si side of the interface displays a relatively sharp transition to amorphous region, which is situated almost entirely on the Al side, showing a gradual transition to crystalline Al. Depending on the position along the interface probed, the width of the amorphous layer varies considerably along the interface as shown in the disparity between Figures 37 and 38. Figure 38 shows a thinner amorphous layer (~10nm) adjacent to the Si crystal but a wide nanocrystalline/ amorphous region (~20 to 40nm) on the opposite side that gradually transitions to crystalline Al. In any case, a thick amorphous layer is present at the interface, which allows a fast diffusion path with a large cross sectional area. This enables a massive amount of atoms to flow down the interface to accommodate interface sliding.

After creep tests were performed (>24 hrs, 624K,  $\tau_i=1.5\text{MPa}$ ,  $\sigma_n=0\text{MPa}$ , and  $h=18\text{nm}$ ), a HREM image was acquired showing that the morphology of the interface evolved during the creep tests as shown in Figure 39. A new nanocrystalline region appeared at the sharp Si interface at the expense of the previously existing amorphous layer. Likewise, the nanocrystalline layer adjacent to the Al crystal shrunk in thickness to approximately 10nm leaving only a small amorphous layer between the two-nanocrystalline regions as shown in Figure 39. The Al crystal adjacent to the nanocrystalline region shown in Figure 38 appeared to grow toward the Si interface during creep testing due to the reordering of the nanocrystalline region. The reordering of the amorphous layer near the Si and Al crystals is likely associated with stress induced ordering. Since the test specimens were slowly cooled during fabrication, any morphology changes that are thermally activated would of already occurred prior to creep testing. Therefore, all morphology changes observed here is presumably assisted by the presence of an applied interfacial shear stress.

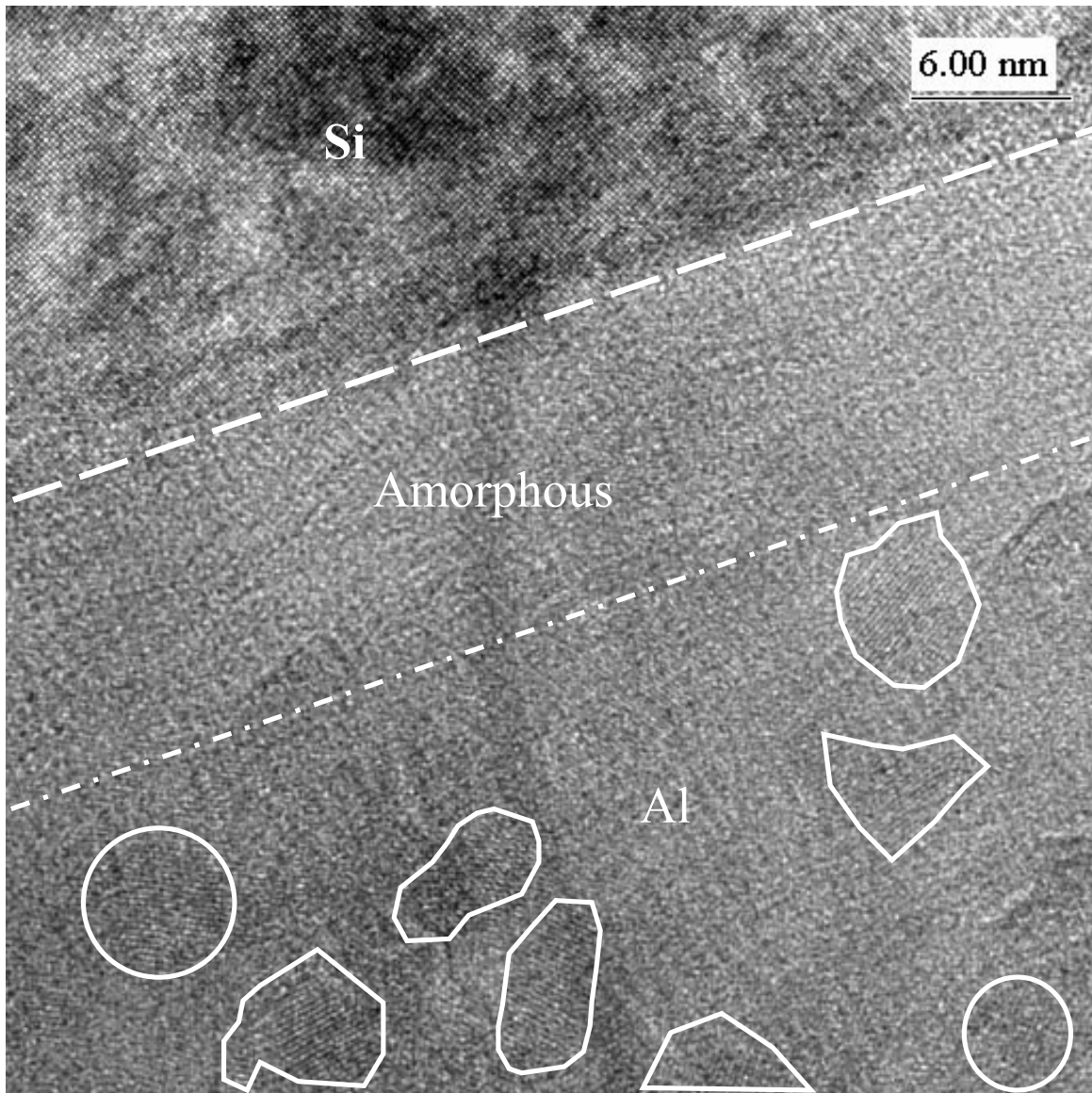


Figure 38. HREM Micrograph Showing Lattice Image of the Single Crystal Si, a Sharp Interface Between the Si and the ~40nm Thick Amorphous Region, and a Gradual Transition to a Nanocrystalline Region of Al Before Creep Testing.

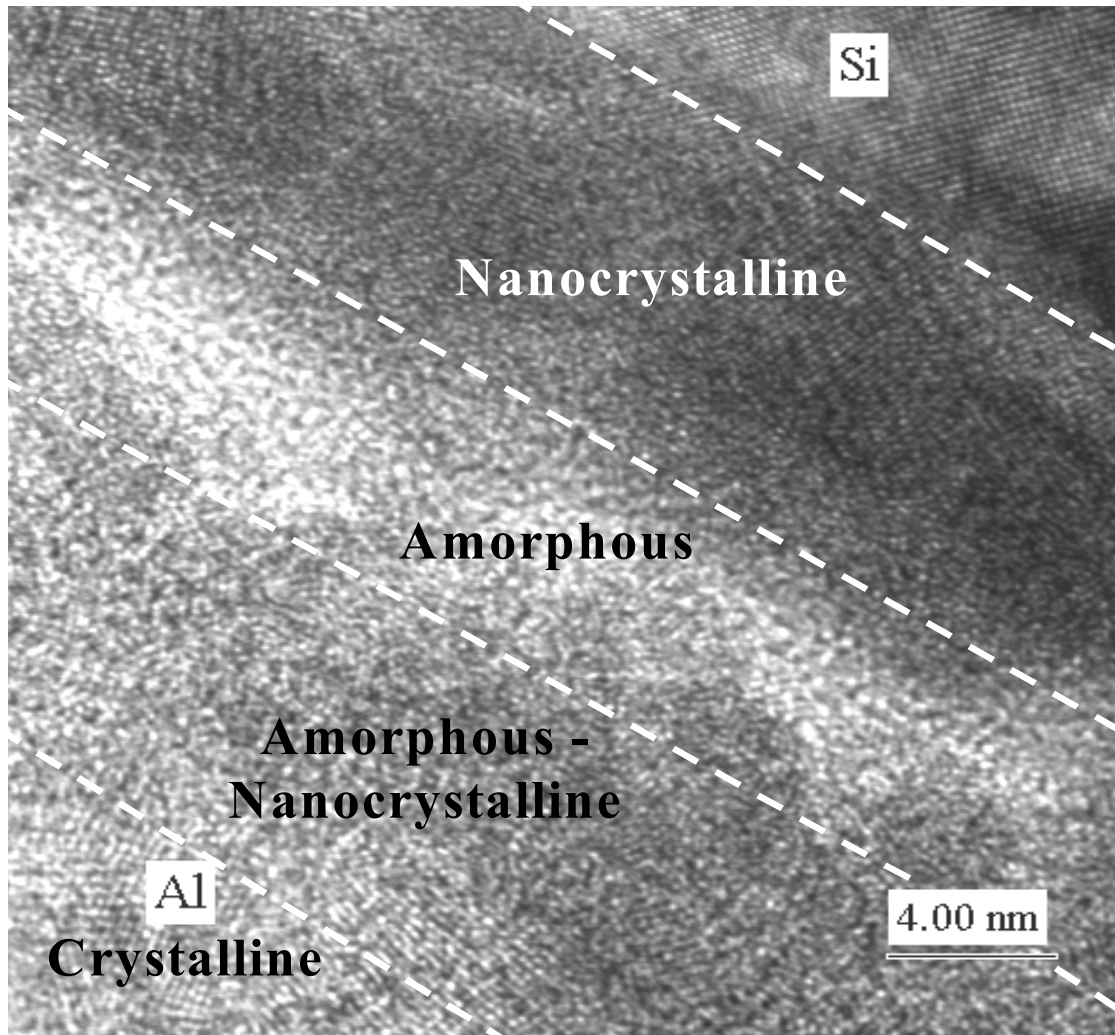


Figure 39. After a Typical Creep Test (>24hours, 624K, 1.5MPa), a HREM Micrograph Shows Lattice Images of (from Left to Right) a Single Crystal Si Adjacent to a Nanocrystalline Region, Which is Next to an Al and O-Rich Amorphous Region Followed by Another Nanocrystalline Region Adjacent to the Al Crystal.

Generally, creep that is “diffusion-controlled” exhibits a minute primary region. In the current Al-Si-Al system, the typical creep curves for various applied shear stresses and interfacial morphologies with and without an applied normal stress show a significant primary region as shown in Figures 24, 28, and 33. The extended primary region is likely associated with the reordering of the amorphous layer. The ordering occurs at the Si and Al crystal interfaces adjacent to the amorphous layer which is thought to be a preferentially nucleation site. Therefore, the nanocrystalline regions grow away from the Si and Al crystalline interfaces toward the middle of the amorphous region. However, the entire amorphous region is not consumed by the reordering. The complete reordering of the amorphous layer is prevented due to the presence of a high concentration of solutes (oxygen and sulfur) which exists in a band less than 10nm wide [77]. Although significant concentration of solutes existed in the nanocrystalline regions prior to creep testing as shown in Figure 16, reordering still occurred during creep testing. This was probably accomplished by exfoliating the solutes out of the region allowing local reordering to occur. The exfoliation of solutes continued until a critical concentration of solutes was attained in a confined band ( $<10\text{nm}$ ) where the formation of the equilibrium structure will never be possible. Once the nanocrystalline regions were fully developed at the expense of ordering the amorphous region, a steady state interfacial creep rate was achieved. As previously discussed, the amorphous region acted as a fast diffusion path but diminished in thickness as the interfacial creep tests continued. As a result, the large interfacial displacement rates that were observed at the beginning of each test (Figures 24, 28, and 33) reduced to a steady state displacement rate once the stable structure of the interface was achieved.

Although the atomistic explanation of the low activation energy is adequate, the interfacial sliding rate dependency on interfacial roughness needs to be addressed. Figures 34 and 35 show that smoother surfaces exhibit a larger interface displacement rate at a constant shear stress and temperature. By taking the slope ( $\dot{U}/\tau_i$ ) from Figure 34 for each of the three interfacial roughnesses ( $h = 18, 54, \text{ and } 174\text{nm}$ ) and normalizing it by the square ( $h^2$ ) of the associated interfacial roughness (experimentally determined by AFM measurements on the surface of Si prior to diffusion bonding as previously

discussed) a relative constant was found to be  $\sim 50 \text{ nm}^2 / \text{MPa} \cdot \text{s}$  shown below and graphically shown in Figure 35b.

$$\left( \frac{h_i^2 \dot{U}}{\tau_i} \right)^{18 \text{ nm}} \cong \left( \frac{h_i^2 \dot{U}}{\tau_i} \right)^{54 \text{ nm}} \cong \left( \frac{h_i^2 \dot{U}}{\tau_i} \right)^{174 \text{ nm}} \approx 50 \frac{\text{nm}^2}{\text{MPa} \cdot \text{s}} \quad (5.8)$$

The relationship between interfacial roughness, shear stress, and displacement rate seems to be in agreement with Equation 5.4 for the three surfaces. An approximate activation energy was experimentally determined for each roughness showing that all the roughnesses ( $h \approx 18, 54, 174 \text{ nm}$ ) are  $\sim 42 \text{ kJ/mol}$  which is correlated with “interfacial diffusion-controlled.” All the plots thus far indicate only one mechanism exists over the entire testing range with an apparent activation energy of  $\sim 42 \text{ kJ/mol}$  ( $T/T_m$  of  $\sim 0.45$ - $0.72$ ,  $\tau_i/G$  of  $\sim 2 \times 10^{-5}$  to  $2 \times 10^{-4}$  with respect to shear modulus of Al,  $\sigma_n$  of 0 to  $3.0 \text{ MPa}$ , and surface roughness  $h \approx 18, 54$ , and  $174 \text{ nm}$ ).

The current model shows that the mechanism may change from interface diffusion-controlled to volume diffusion-controlled (or grain boundary diffusion controlled if the grain size is small), if the interfacial roughness becomes too large. As the ratio of  $h/\lambda$  exceeds unity (Figure 20), the mechanism of diffusion to accommodate interface sliding may change more predominately to volume diffusion ( $\delta_i D_i / D_v \ll 1$ ), where  $D_v$  is the coefficient of volume self-diffusion. Raj and Ashby [32] analytically determined for grain boundaries containing discrete particles that the sliding rate was limited by boundary diffusion ( $\delta_i D_i / D_v \gg 1$ ) when the particles were sufficiently small.

As the particles become large, the grain boundary-sliding rate was be limited to volume diffusion-controlled. Obviously, when an intermediate particle size was present at the grain boundary, the sliding rate was controlled by both diffusion mechanisms, which were at par with each other. In the Si-Al system, the asperities of the Si (interfacial roughness) can be thought as particles at a smooth interface. As the asperities of Si increase (increasing interfacial roughness causes  $\lambda/h \gg 1/h$ ), the controlling diffusion mechanism may shift from “interfacial diffusion-controlled” to “volume diffusion-



controlled” to accommodate interface sliding. The interface sliding relationship proposed by Funn and Dutta (Equation 5.4) is able to model the change of the controlling diffusional mechanism accommodating interface sliding when  $\lambda/h$  becomes much greater than  $1/h$ . Neglecting the effects of threshold stress ( $\sigma_n=0$ ), assuming grain boundary diffusion is negligible, and comparing the diffusional terms in Equation 5.4, the diffusional mechanism dependence on interfacial roughness emerges as seen below:

$$(\text{volume diffusion-controlled}) \frac{D_v \lambda}{\pi h^2} \Leftrightarrow \frac{2\delta_i D_i}{h^2} (\text{interface diffusion-controlled}) \quad (5.9)$$

The comparison between volume and interface diffusion-controlled made in Equation 5.9 shows that for small interfacial roughness ( $h$ ) and small interfacial periodicity ( $\lambda$ ) the volume diffusion-coefficient becomes smaller than the interfacial diffusion-coefficient. In this case, the controlling mechanism is predicted to be interface diffusion-controlled to accommodate interface sliding. When the interfacial roughness ( $h$ ) becomes large and the interfacial periodicity ( $\lambda$ ) increases appropriately (where  $\lambda/h$  remains roughly the same or greater but  $1/h$  diminishes drastically), the interfacial diffusion coefficient diminishes while the volume diffusion-coefficient increases. As a result, the controlling mechanism shifts from interface diffusion-controlled to volume diffusion-controlled. The current interface-sliding model [3] is adequate to predict the shift of the controlling mechanism as the interfacial roughness changes, but more experimental data is needed to validate the model for rougher surfaces.

Threshold stresses, below which no creep occurs, varies from system to system [26]. In the present experiments when no normal stress was applied on the interface ( $\sigma_n=0$ ), a threshold stress ( $\tau_o=0$ ) was not observed for any roughness, temperature, or shear stress regime (Figures 25 and 34), which is consistent with the model proposed by Funn and Dutta [3] delineated in Equations 5.4 to 5.7. However, when a compressive normal load was applied to the interface, the effective shear stress ( $\tau_{\text{eff}}$ ) was reduced, thereby reducing the interface displacement rate  $\dot{U}$  for all interfacial roughnesses (Figures 29 - 31, and 36). In all cases, a compressive normal stress on the interface yielded a significant threshold stress that is clearly observed in Figures 29 - 31, and 36.

The observed threshold stresses ( $\tau_o$ ) for specimens with an interfacial roughness  $h \approx 18$  nm (Figure 31) were approximately 0, -1.4, and -1.7MPa when an applied normal stress of  $\sigma_n \approx 0$ , -1.5, and -3.0MPa respectively was applied. Equation 5.6 can be rearranged to predict the threshold stress for specimens with a larger interfacial roughness ( $\tau_o^{54nm}$ ) from the previously experimentally determined threshold stress for smoother ( $\tau_o^{18nm}$ ) specimens (Figures 29 - 31) along with AFM measurements of the interfacial roughness ( $h/\lambda \approx 0.16$  and 0.36 respectively from Figure 20) by:

$$\tau_o^{54nm} = \tau_o^{18nm} \frac{\left(\frac{h}{\lambda}\right)_{54nm}^3}{\left(\frac{h}{\lambda}\right)_{18nm}^3} \quad (5.10)$$

The predicted threshold stresses ( $\tau_o^{54nm}$ ) for specimens with  $h \approx 54$ nm when a -1.5 MPa or -3.0 MPa normal stress is applied are about  $\sigma_n \approx -4.3$  and -8.7MPa respectively. These values are much higher than observed in Figure 40 ( $\tau_o \approx -1.4$  and -1.7 MPa respectively). The low experimentally determined threshold values are likely because of morphology changes that occurred at the interface during creep tests as previously discussed. If the interfacial roughness ( $h$ ) of the sandwich specimens is reduced by ~30% due to morphology changes during creep tests, the low experimentally determined threshold stress would be in good agreement with the new predicted values of  $\tau_o^{\text{corrected}} \approx -1.4$ MPa from Equation 5.10. Some other errors that might cause low measurements of threshold stresses are (1) the interfacial roughness is reduced more for rougher interfaces than smoother surfaces during creep tests and (2) the AFM statistical representation of the interfacial roughness is inadequate (i.e., average  $h$  and  $\lambda$  versus maximum values of  $h$  and  $\lambda$ ). Overall, the interface-sliding model adequately predicts threshold stresses when a normal stress is applied to various interfacial roughnesses. It is recommended in future studies that the experimental approach be optimized to circumvent any interfacial morphology changes during creep testing.

As the interfacial roughness becomes very rough, not only does the mechanism changes (thus interfacial strain rate) but the origination of the threshold stress. To gain

more insight on the origin of threshold stresses when the controlling diffusional mechanism changes, a comparison between the terms which represent threshold stresses for volume and interfacial diffusion in Equation 5.4, was made (Equation 5.11). Equation 5.11 shows that when the diffusional mechanism changes from interfacial diffusion-controlled to volume diffusion-controlled, the second term in Equations 5.4 and 5.11 becomes negligible, thereby reducing the threshold stress by half compared to interface diffusion-controlled threshold stress.

$$(\text{volume diffusion-controlled}) \left( \frac{\pi h}{\lambda} \right)^3 \sigma_n \Leftrightarrow 2 \left( \frac{\pi h}{\lambda} \right)^3 (\text{interface diffusion-controlled}) \quad (5.11)$$

When the controlling mechanism shifts, not only does the strain rate decrease because of  $\lambda/h \gg 1/h$ , but the effective shear stress ( $\tau_{\text{eff}}$ ) also increases because of the decrease in the threshold stress. The current model is able to predict not only the diffusion-controlling mechanism but also the change in the origination of threshold stresses when interfacial roughnesses become very large.

## E. CONCLUSION

An experimental approach to isolate and measure the creep behavior of interfaces in multi-component systems was refined, and used to study model diffusion-bonded Al-Si interfaces. The kinetic parameters for interface sliding were experimentally determined for the Si-Al system by measuring the interface displacement rates at various temperatures while varying the interfacial shear stress, normal stress, and interfacial roughness. Experiments showed that the Al-Si interfaces undergo diffusionally accommodated sliding under shear stresses at high temperatures. The measured kinetics showed that the mechanism of sliding is interfacial diffusion-controlled diffusional flow. The experimental data also showed that a threshold stress existed when a normal stress was applied and diminished to zero when the applied normal stress was removed. Like the classical grain boundary sliding mechanism [32], interfacial sliding occurs due to mass-transport under a periodically varying normal stress field acting on the interface due to an applied far-field shear stress, with the mass transport path being associated with the

interface. In the present experiments, the activation energy was found to be lower ( $\sim 42$  kJ/mol) than volume (142 kJ/mol) or grain boundary (84 kJ/mol) diffusion for the Al system and was attributed to Al atoms diffuse rapidly along an amorphous interfacial layer under the applied stress, leading to the observed sliding. This is consistent with a mechanism proposed earlier [3], where here the planar semiconductor-metal interfaces undergo thermally activated sliding via interfacial diffusion-controlled diffusional creep mechanism. The experimental data affirms the current model proposed by Funn and Dutta is accurate for planar interfaces with various interfacial roughnesses at high homologous temperatures (with respect to Al) with or without applied normal stresses.

THIS PAGE INTENTIONALLY LEFT BLANK

## **VI. INTERFACIAL SLIDING OF INTERCONNECT STRUCTURES IN MICROELECTRONIC DEVICES**

### **A. STANDALONE Cu INTERCONNECTS ON Si**

*Published in the Journal of Electronic Materials, Vol. 30, No. 12, 2001, p. 1537  
(co-authored with I. Dutta, M.W. Chen, and T. Shultz)*

#### **1. Introduction**

The mechanical behavior of thin films on semiconductor substrates is of much interest to the microelectronics industry. Thin films generally have properties different from their bulk counterparts, and their thermo-mechanical response may be influenced significantly by the underlying substrate [76, 94]. Due to differences in the coefficient of thermal expansion (CTE) between thin metallic films and semiconductor substrates in microelectronic devices, large stresses can develop in thin films during thermal excursions experienced in processing steps or service. This may induce plastic deformation of the thin films accompanied by creep and interfacial sliding [6, 15, 16], possibly leading to a pronounced effect on the reliability of microelectronic devices and components.

During thermal cycling, a metallic film attached to a substrate traverses through a range of stress/temperature regimes, leading to the operation of a multitude of plastic deformation mechanisms, such as dislocation glide (i.e., yielding), as well as dislocation and diffusional creep [15, 16]. In the absence of interfacial sliding, this plasticity results in stress relaxation in the film, with no relative size change between the film and the substrate. However, if interfacial sliding is allowed to occur, plastic deformation of the film may be accommodated by differential deformation between the film and the substrate, resulting in a change of the film size.

Recently, Chen and Dutta [6] studied deformation of unpassivated, small-area Al thin films on Si substrates by atomic force microscopy (AFM), and noted significant changes in film-dimensions associated with thermal cycling. This was attributed to plastic deformation of the film, accommodated by diffusion-controlled interfacial sliding

near the film-edges, which allowed the lateral dimensions of the film to change. It was suggested [6] that the impact of sliding, and hence the proportionate change in film size, increases with decreasing film width. Since the current trend in microelectronics is towards progressively smaller line widths, it is likely that such effects will assume considerable importance in future devices, making it important to develop an understanding of the roles of film plasticity and interfacial sliding in thin film systems.

In this chapter, we report on the results of a study of plastic deformation of Al and Cu thin films on Si substrates using AFM and finite element modeling (FEM), with the goal of understanding the effects of film plasticity and interfacial deformation on the dimensional stability of thin films.

## **2. Background**

It has been demonstrated theoretically and experimentally that the deformation of one of the phases in a multi-component system may be accommodated at the interface by interfacial creep, resulting in dimensional differences between the components during thermo-mechanical loading [4, 5]. In fiber-reinforced metal-matrix composites, for instance, interfacial sliding has been observed near fiber-ends during thermal cycling, resulting in a difference between the lengths of the fiber and matrix phases, although they were identical in length prior to cycling [1, 5]. This differential deformation has been attributed to plasticity/creep of the metallic-matrix due to internal residual stresses, accommodated by interfacial sliding near the fiber-ends. Experiments on high-density Cu/Ta/Polyimide interconnect structures deposited on a Si wafer have also shown evidence of interfacial sliding between Cu lines and Ta liners, resulting in the appearance of out-of-plane steps on an initially smooth surface following thermal cycling corresponding to dielectric processing conditions [11]. In both cases, interfacial sliding was thought to occur by a diffusional mechanism, driven by interfacial shear stresses generated due to thermal expansion mismatch between the constituent phases (in the axial direction for matrix and fiber, and out-of-plane direction for Cu and polyimide).

Funn and Dutta [3] have shown that interfacial sliding in the absence of adhesive failure may be described by a diffusional creep law with a threshold stress and an

activation energy corresponding to interfacial diffusion. Based on a periodic interface model, they proposed that sliding occurs by interface-diffusion-controlled diffusional creep, with contributions from both shear ( $\tau_i$ ) and normal stresses ( $\sigma_i$ ) acting on the interface, with the sliding strain rate  $\dot{\gamma}_i$  being given by:

$$\dot{\gamma}_i = \frac{4\delta_i D_{i_0} \Omega}{kTh^3} \left[ \tau_i + 2\pi^3 \left( \frac{h}{\lambda} \right)^3 \sigma_i \right] \exp \left[ -\frac{Q_i}{RT} \right] \quad (6.1)$$

where  $\delta_i$  is the thickness of the interface,  $Q_i$  and  $D_{i_0}$  are the activation energy and frequency factor, respectively, for interfacial diffusion,  $\Omega$  is the atomic volume of the diffusing species (i.e., film material),  $\lambda$  and  $h$  are the topographical periodicity and roughness, respectively, of the interface, and  $k$ ,  $R$  and  $T$  are the Boltzmann's constant, gas constant, and the absolute temperature, respectively. Clearly, whereas the shear stress  $\tau_i$  is the primary driving force for interfacial creep, the normal stress  $\sigma_i$  also has a contribution, which depends strongly on the interfacial roughness parameter  $h/\lambda$ . A compressive (negative)  $\sigma_i$  would result in a threshold behavior and slow the rate of sliding, whereas a tensile (positive)  $\sigma_i$  would increase the effective stress at the interface, and hence enhance the sliding rate. Finally, since the sliding rate is inversely proportional to  $h^3$ , a smoother interface would be expected to slide more readily. Thus, smooth interfaces with a shear and a normal tensile stress acting on them would be the most susceptible to sliding.

Since significant interfacial shear stresses only exist near the edges of a thin film, interfacial sliding is an edge effect, and as such, can be ignored for large-area films. However, with decreasing lateral film dimensions (e.g., in electronic applications where line widths are at the sub-micron level) these effects are likely to become important, particularly since the interfaces involved are very smooth and the interfacial shear stress is often augmented by normal tensile stresses (peeling stress) acting near the film edges.



### 3. Experimental Approach

Chen and Dutta [6] used an array of nominally 250 nm thick, 6  $\mu\text{m}$  square pure Al films that were deposited by thermal evaporation on to a Si (100) wafer utilizing a Ni mask. Their samples were subjected to 5 thermal cycles from 293K to 623K in a vacuum furnace at a pressure of  $\sim 5.0 \times 10^{-7}$  Torr. During thermal cycling, the ramp-up rate was  $\sim 20$  K/min, and the nominal cooling rate was  $\sim 2.5$  K/min. Figure 40 shows a typical AFM image of the square Al films on a Si substrate on a  $40\mu\text{m} \times 33\mu\text{m}$  scan area. Small scale scanning revealed that the surface roughness of the Si substrate is below 1 nm, suggesting that the interfaces between Al films and Si substrates are very smooth.

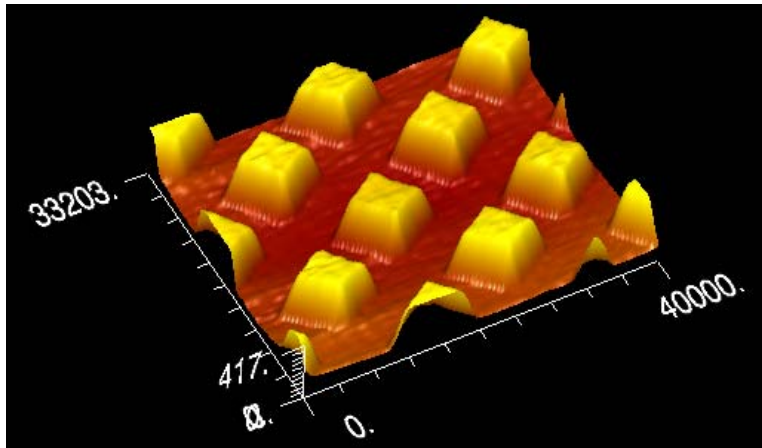


Figure 40. AFM Image of an Array of Square Al Thin Film Islands on Si. Each Island is Nominally 250nm Thick and Has Lateral Dimensions of  $6\mu\text{m} \times 6\mu\text{m}$ . [6]

A pattern of parallel 1.4  $\mu\text{m}$  wide Cu lines with a pitch of 2  $\mu\text{m}$  was deposited on a (100) Si wafer via electroplating at Motorola, Tempe Arizona. The basic fabrication procedure consisted of lithographically defining the lines in a photo-resist coated on to the wafer, sputter-depositing a barrier layer of Ta and a seed layer of Cu, followed by Cu electro-plating, planarizing, and resist-stripping. Subsequently, the sample was annealed for 30 minutes at 673K to stabilize the Cu-grain structure, and then subjected to 5 thermal cycles from 293K to 723K in vacuum at nominal heating and cooling rates of 10K/minute. Figure 41 shows a typical AFM image of the Cu lines on Si substrate over a  $10\mu\text{m} \times 5\mu\text{m}$  scan area.

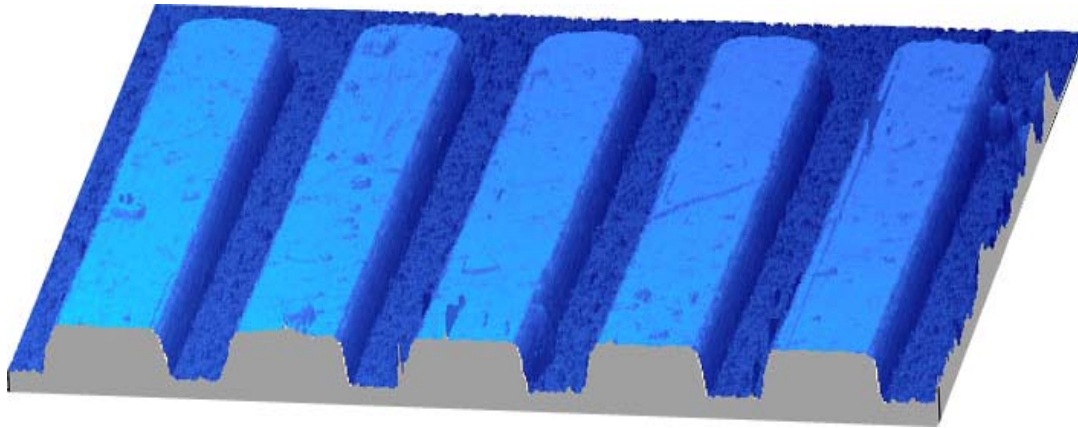


Figure 41. AFM Image of an Array of Parallel Cu Lines on Si. The Lines are Nominally 250nm Thick and 1.4 $\mu$ m Wide.

To identify the deformation induced by thermal cycling, the cross-sectional profiles of the square Al films and Cu lines were measured before and immediately after thermal cycling by an AFM at room temperature in air. For the square Al films, the profiles were measured parallel to the square edge through the center of the square. For the Cu lines, the profiles were measured perpendicular to the line length far from the ends of the lines. For the Al films, the AFM measurements were carried out in non-contact mode, whereas for the Cu films, the contact mode was used in order to yield a better resolution. The lateral displacement resolution produced was estimated to be better than 15nm with the 20 $\mu$ m scan range used for the Al films, and 10nm with the 10 $\mu$ m range used for the Cu lines.

#### 4. Modeling Approach

A plane-strain finite element (FE) model of a thin-film line on a Si substrate, with the model plane being normal to the line length, was developed in order to evaluate the film and interfacial stress and strain states associated with thermal cycling [6]. Figure 42 shows a schematic of the model with the appropriate nomenclature. The model was built with the multi-purpose FE program ANSYS™, utilizing 8-noded triangular solid elements for both film and substrate. The Si substrate was modeled as an isotropic elastic solid, whereas the metallic thin-film was represented as an isotropic elastic-plastic-

creeping solid exhibiting temperature-dependent bilinear properties, and subject to dislocation creep via power-law (PL) and power-law breakdown (PLB). Since the FE model could account for only one creep law, a sinh-law was picked because dislocation creep prevails over a wide range of stress/temperature conditions, although it is realized that Coble creep is likely to be important at high temperatures [15]. Therefore, the FEM analysis is expected to somewhat underestimate creep relaxation effects in the film at the higher end of the thermal cycle. Since temperature dependent thin film properties were not readily available, room temperature thin film properties were scaled to conform to the same temperature dependence as bulk polycrystalline elastic-plastic properties. For creep, data for bulk polycrystalline Al and Cu presented in [Reference 62](#) were utilized. In the model, the interface was assumed to be perfectly bonded and non-sliding, because of the difficulty of incorporating the planar interfacial creep law into the FE program. For both Al and Cu, the film was assumed to be 100nm thick ( $t_f$ ), and 5 $\mu$ m wide ( $l_f$ ), and the substrate was assumed to be 5 $\mu$ m thick ( $t_s$ ).

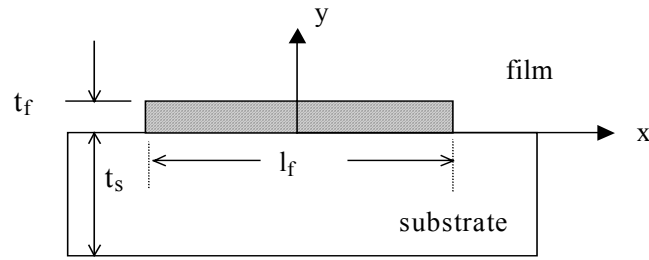


Figure 42. Schematic of the Film-Substrate System Used for the FE Model where  $l_f$  is the Film Width and  $t_f$  is the Film Thickness, and  $t_s$  the Substrate Thickness. Since the System is Laterally Symmetric, Only Half of the System (Corresponding to Positive x-Values) was Modeled. [6]

## 5. Results

### a. *Experimental*

In this section, we will briefly present results obtained by Chen and Dutta [6, 7] on evaporated Al films on Si, and use these results to compare with the results obtained on electroplated Cu films. Figure 43 shows typical cross-sectional profiles of the Al films before and after 5 thermal cycles. After thermal cycling, the film-width close to the interface became larger and the slope of the film edges became shallower,

indicating that (1) there was a gradient of plastic deformation along the through-thickness direction of the film, and (2) more plastic deformation occurred close to the interface. Since there was statistical variation in the size of the film islands, they randomly measured the widths of about 70 square films and plotted the size distribution of the samples before and after thermal cycling in Figures 44a and 44b. All the values were measured at a height of 20 nm from the Si-Al interface. By fitting the histograms to a Gaussian distribution, it was shown that the mean of the distribution (solid lines in Figure 44b) moves to a higher value after thermal cycling. Prior to thermal cycling, the edges of the square islands of Al-film were found to vary within a standard deviation ( $2\sigma$ ) of  $\pm 0.35\mu\text{m}$  from the mean of  $5.99\mu\text{m}$ . Following cycling, the mean shifted to  $6.20\mu\text{m}$ , with a  $2\sigma$  value of  $\pm 0.30\mu\text{m}$ . It was believed that the difference of  $\sim 0.2\mu\text{m}$  in the mean value arose due to plastic deformation of the film, induced by thermal cycling. The average lateral strain of the square films is  $\sim 3.3\%$ . After subtracting the elastic strain induced by residual tensile stresses, the plastic deformation of the films was estimated to be about 3%.

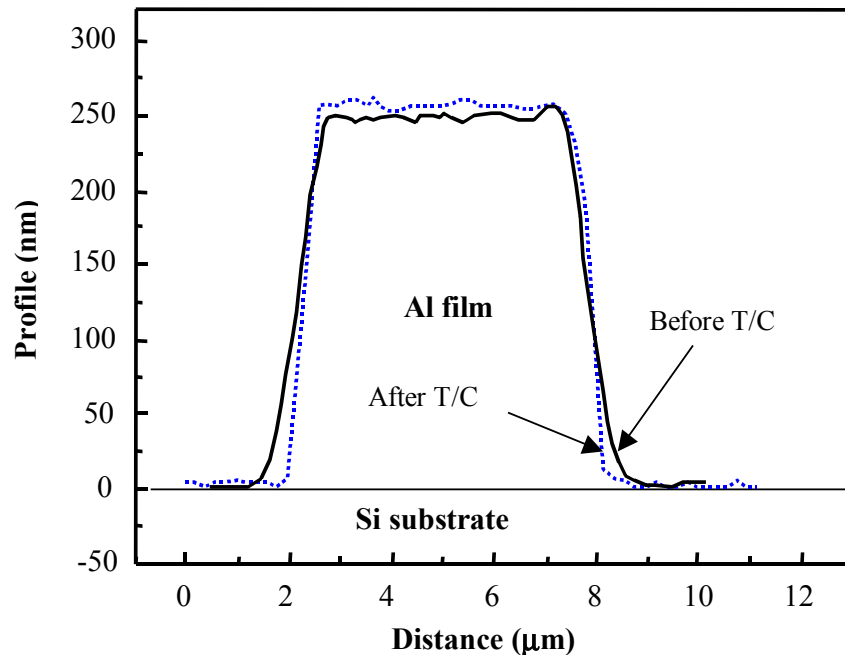


Figure 43. Representative Cross-Sectional Profiles of the Square Al Films Before and After 5 Thermal Cycles from 293 to 623K. [6]

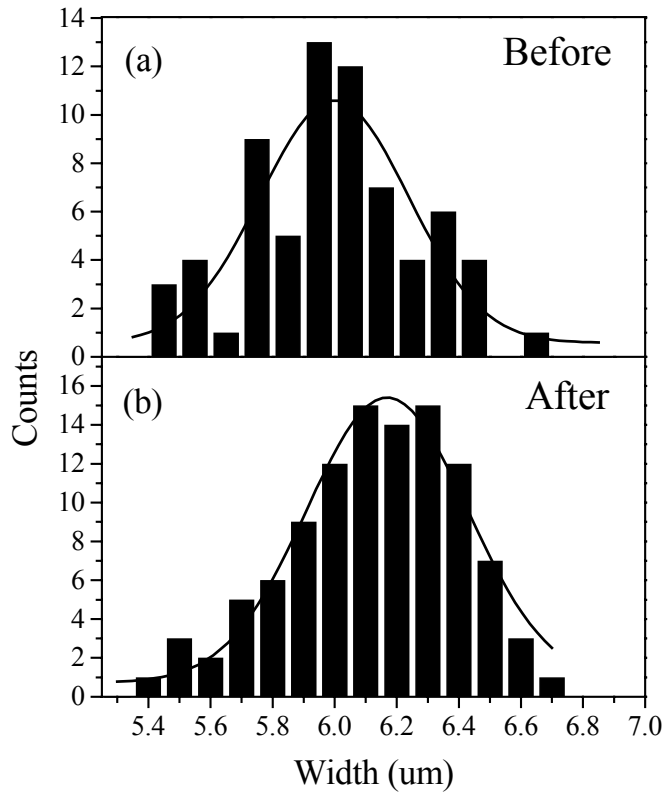


Figure 44. Histograms and the Associated Gaussian Fits of the Width Distribution of the Square Al Films at a Distance of 20nm from the Interface; (a) Before Thermal Cycles; and (b) After 5 Thermal Cycles. [6]

Figure 45 shows typical profiles of the Cu lines prior to, and following the first through fifth cycle. Contrarily to what is observed for Al films, the electroplated Cu lines are observed to shrink with progressive cycling, with the vertical profile of the film edges becoming sharper (i.e., less sloped). The histograms in Figure 46 show the line-width distributions 20nm from the interface at different stages of cycling. The mean of the distribution decreased from  $1.429\mu\text{m}$  in the uncycled state to  $1.294\mu\text{m}$  after the 5th cycle. The standard deviations of the width measurements ranged from  $0.013$  to  $0.022\mu\text{m}$ , well below the measured change in line width due to cycling. Figure 47 shows the change in width with progressive cycling. It is observed that the line width decreases almost linearly till the third cycle, after which the rate of change of width becomes slower.

Presumably, the ratcheting down of the line width will saturate at a finite number of cycles, beyond which the line width would remain stable. Figure 47 also shows that corresponding to the decrease in line width, there is an increase in the line thickness (or height) during cycling. This increase in thickness is associated with the requirement to maintain volume constancy during plastic deformation of the lines.

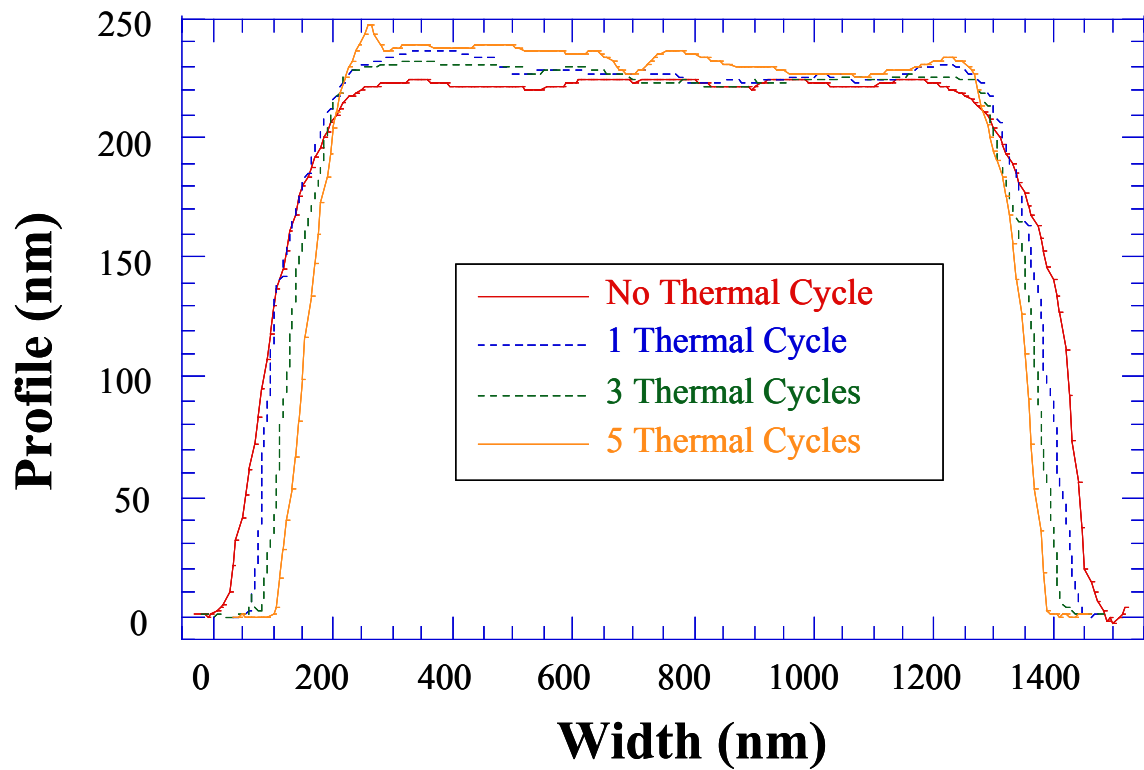


Figure 45. Typical Cross-Sectional Profiles of a Cu Line at Different Stages of Thermal Cycling from Ambient to 723K. The Width of the Cu Line is Observed to Decrease with Increasing Number of Thermal Cycles.

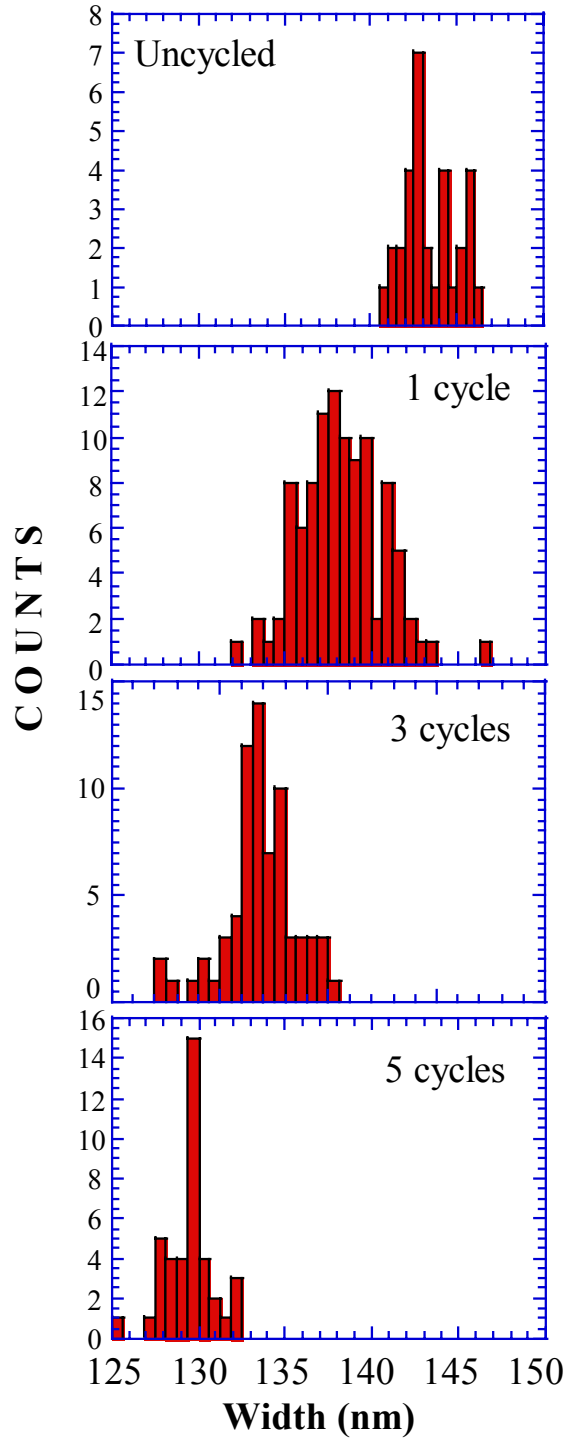


Figure 46. Histograms of the Width Distribution of Cu Lines at a Distance of 20nm from the Interface Prior to Thermal Cycling, and Following 1, 3 and 5 Thermal Cycles. The Means and Standard Deviations of the Distributions are as Follows : (a) Before :  $1429 \pm 15$  nm, (b) 1 Cycle :  $1382 \pm 21$  nm, (c) 3 Cycles:  $1317 \pm 16$  nm, and (d) 5 Cycles :  $1296 \pm 13$  nm.

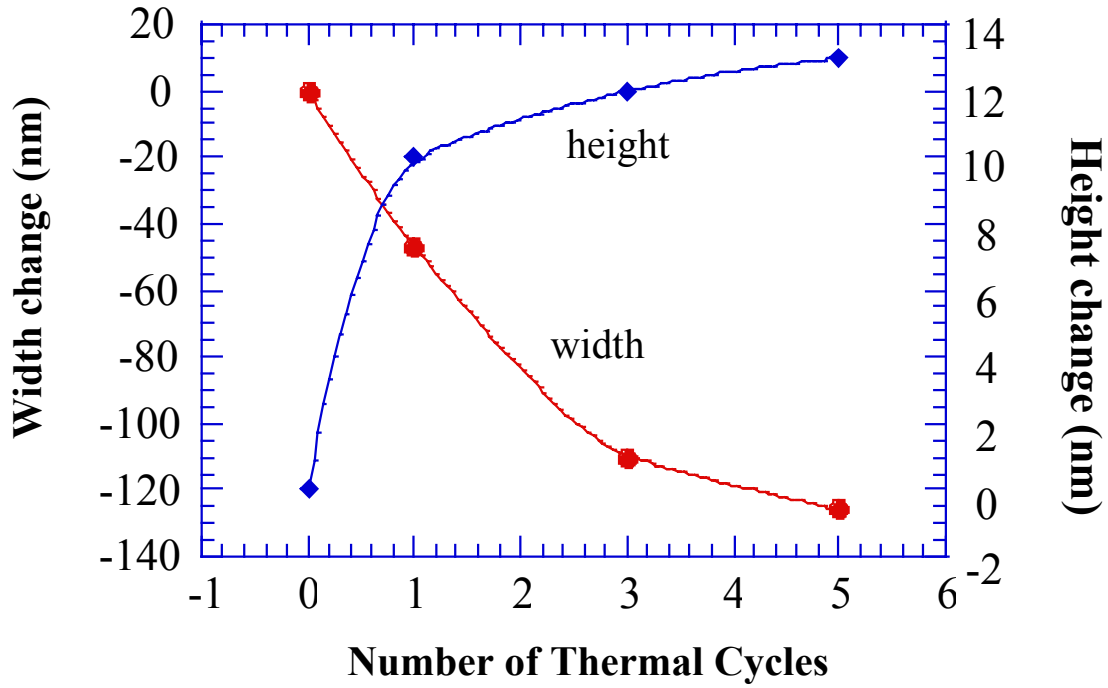


Figure 47. Changes in Cu Line Width and Line Thickness Plotted as a Function of the Number of Thermal Cycles.

**b. Modeling**

Figure 48 shows the computed stress distribution along the film width in an unpassivated Al film following cooling to ambient after annealing at 644K. Figure 48a plots the in-plane normal stress  $\sigma_{xx}$  very close to the interface ( $y/t_f \approx 0.02$ ), whereas Figure 48b shows the interfacial shear stress  $\tau_i$  at the interface ( $y/t_f = 0$ ). All the stresses have been normalized by the elastic misfit stress  $\sigma_o$ , which is given by:

$$\sigma_o = \frac{(\alpha_s - \alpha_f) \Delta T}{\left( \frac{1 - \nu_f}{E_f} \right) + \left( \frac{1 - \nu_s}{E_s} \right) \left( 4 \frac{t_f}{t_s} \right)} \quad (6.2)$$

where the subscripts f and s represent the film and the substrate, respectively,  $\alpha$ ,  $\nu$ ,  $E$  and  $t$  represent the coefficient of thermal expansion, Poisson's ratio, Young's modulus and thickness, respectively, and  $\Delta T$  is the temperature range of cooling. It is apparent from Figure 48a that with a decrease in film width relative to film thickness (i.e., with



increasing  $t_f/l_f$ ), the in-plane normal stress decreases, but varies over a greater proportion of the film width. Whereas for  $t_f/l_f=0.002$ ,  $\sigma_{xx}$  is nearly constant throughout the film width except right at the edge, for  $t_f/l_f=0.5$ ,  $\sigma_{xx}$  varies throughout the film width. Since the interfacial shear stress  $\tau_i$  is nominally proportional to the first derivative of  $\sigma_{xx}$  with respect to  $x$ , it is observed from Figure 48b that  $\tau_i$  is zero throughout most of the film width for  $t_f/l_f=0.002$ , but becomes non-zero over a larger proportion of the film width as  $t_f/l_f$  increases. In general,  $\tau_i$  is maximum at the film edge ( $2x/l_f = 1$ ), and decreases with increasing distance from the edge. Figure 48b also shows that in addition to a large interfacial shear stress that exists near the film edges, there is a normal tensile (or peeling) stress  $\sigma_{yy}$ , which is large at the film edge, and decreases rapidly on moving away from the edge. It is further observed that this normal interfacial stress increases with decreasing film width (or increasing  $t_f/l_f$ ). As discussed in section 6,  $\tau_i$  and  $\sigma_{yy}$  together provide the impetus for interfacial sliding near the film edges. Since both these quantities are larger for smaller  $t_f/l_f$ , a narrower film is expected to display a greater degree of interfacial sliding.

Figure 49 shows the computed variation of the maximum in-plane film stress, at  $2x/l_f = 0$  and  $y/t_f = 0.5$  (i.e., at the centerline of the sample and mid-plane of the film), during thermal cycling for a pure Al film on Si, following initial cooling from the annealing temperature. Also shown on the same plot are the Von-Mises (VM) creep and plastic strains at the same location. It is observed that the film stress starts from a large tensile value, which is rapidly relieved upon heating to  $\sim 350\text{K}$ , beyond which compressive stresses build up within the film. Around  $380\text{K}$ , the compressive stresses in the film start getting relieved because of creep processes, resulting in a knee in the plot. Commensurately, the VM creep strain is observed to increase rapidly. During cooling, tensile stresses build up, first slowly because of creep, and then rapidly as creep processes decelerate. This is reflected by the decreasing V-M creep strain, suggesting creep in the opposite direction. Finally, around  $350\text{K}$ , the tensile stresses become large enough to cause some yielding of the film, as reflected by an increase in the V-M plastic strain.

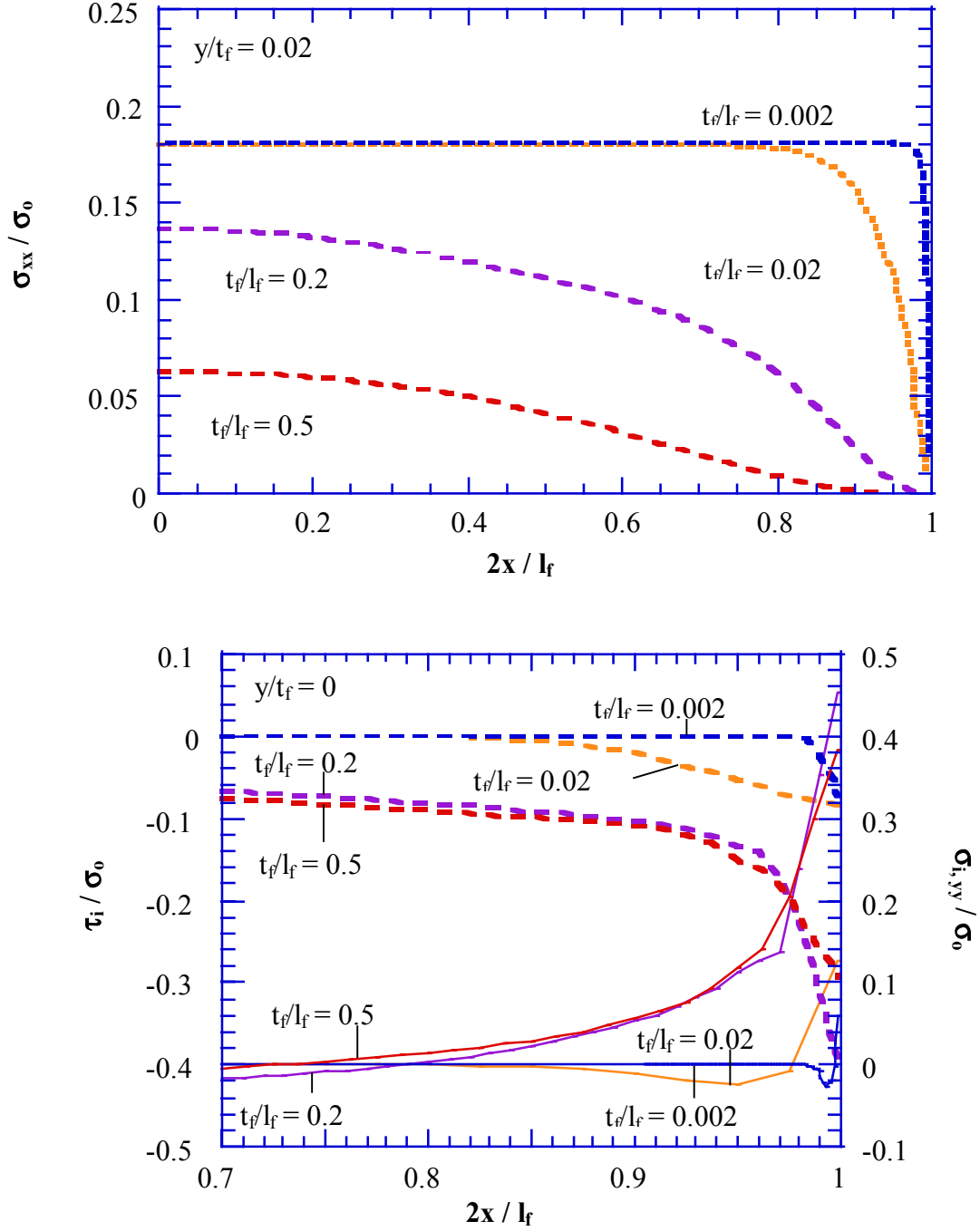


Figure 48. (a) Distribution of In-Plane Normal Stress ( $\sigma_{xx}$ ) Along Film-Width for an Al Film on Si at Ambient Temperature, Following Cooling from Annealing Temperature. (b) Distribution of Interfacial Shear ( $\tau_i$ ) and Normal ( $\sigma_{i,yy}$ ) Stresses Along Film-Width for the Same Conditions. The Dashed Lines Refer to  $\tau_i$ , While the Solid Lines Refer to  $\sigma_{i,yy}$ . All the Stress Distributions are Shown for Varying  $t_f / l_f$  Values. The Abcissa Represents Distance  $x$  Along the Film-Width, Normalized by Half the Film Width  $l_f / 2$ . [6]

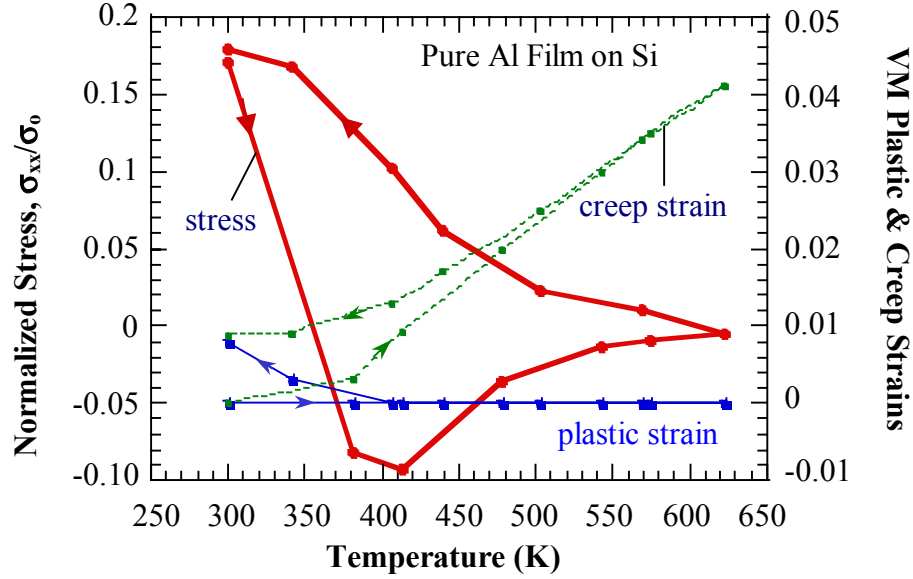


Figure 49. Computed Variation of  $\sigma_{xx}$  and the Von-Mises Effective Plastic and Creep Strains in an Al Film During Thermal Cycling. [6]

For clarity, it is useful to inspect the in-plane plastic and creep strain distributions ( $\epsilon_{xx}^{pl}$  and  $\epsilon_{xx}^{crp}$ ) within the film at 623K (end of heating segment) and 300K (end of cooling segment). Figure 50 shows these strain distributions close to the film-edge. It is apparent that at 623K, the cumulative  $\epsilon_{xx}^{pl}$  is in tension in most of the film (away from the edge), but the cumulative  $\epsilon_{xx}^{crp}$  is in compression. It should be realized that the plastic strain was induced during initial cooling from the annealing temperature, and not during the thermal cycle. The creep strain, on the other hand, is induced entirely during cycling. So a net compressive inelastic strain is induced in the film during heating to 623K, most of it due to creep. During subsequent cooling, substantial tensile creep occurs, leaving only a small negative creep strain at 300K. Concurrently, a large tensile plastic strain is induced at the lower temperatures, resulting in a net tensile inelastic strain after 1 complete cycle. This is consistent with Figure 43, from which it may be inferred that during one complete thermal cycle, the net plastic strain is tensile, and the net creep strain (which is tensile up to ~350K, compressive from 350 to 623K, and tensile again during cooling from 623 to 300K) is slightly compressive, resulting in a net tensile inelastic strain at the end of the cycle.

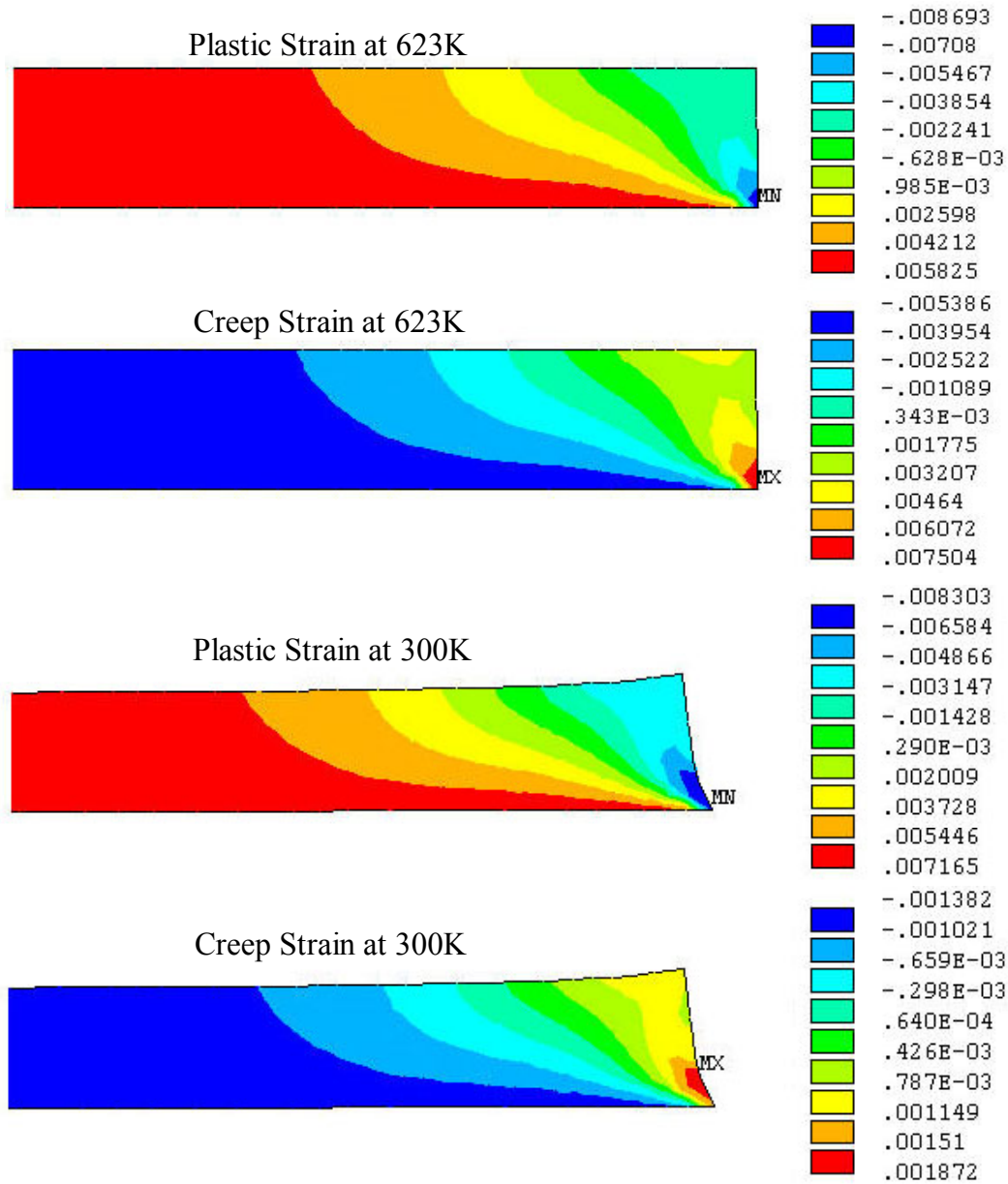


Figure 50. The Distribution of In-Plane Plastic and Creep Strains Near the Edge of the Al Film at the End of the Heating Segment (623K) and at the End of the Thermal Cycle (300K). The Displacement Scaling Has Been Exaggerated to Reveal Changes in the Edge Profile Associated with Cycling. The Middle of the Film Lies Far Away (Beyond the Picture) Towards the Left. All the Contour Plots have the Same Scaling, and the Observed Differences in Size and Location in the x-Direction Between the Two Temperatures are Representative of Reality. [6]

Despite the net tensile inelastic strain, the footprint of the film is not expected to change in the absence of interfacial sliding. The induced inelastic strains serve mainly to relax the film stresses, and cause a change in the film profile near the edge, as evident in Figure 50. Figure 51 shows the computed profiles of the right edge of the Al film at different stages of heating and cooling during the thermal cycle. Since interfacial sliding was not accounted for in the model, the observed changes in film width during cycling are related to associated changes in substrate dimensions at different temperatures. Because of the built-in stress state at ambient temperature, the film starts with a right-edge profile, which slopes inward from the interface to the top. Upon heating (e.g., to 478K), as the film attempts to expand more than the substrate, the edge profile becomes steeper, and becomes almost vertically straight at 623K. Upon cooling, the initial slope is regenerated, and the film-edge returns to its original location. Only a small change in the edge-profile is observed in association with film plasticity near the edge. Figure 52 shows the distribution of  $\tau_i$  near the edge of the Al film at various temperatures. Clearly, as the in-plane film stress transitions from tensile to compressive, the sense of the shear stress changes. At 300K,  $\sigma_{xx}$  is tensile and the sense of  $\tau_i$  is such that it would make the film-edge move outward (i.e., towards larger  $2x/l_f$  values) if sliding were allowed. At 478K during heating, on the other hand,  $\sigma_{xx}$  is compressive, and the prevailing sense of  $\tau_i$  would make the film-edge move inward (towards smaller  $2x/l_f$  values) with sliding occurring in the opposite direction. However, since  $\tau_i$  is negative over the majority of the thermal cycle, if interfacial sliding were to occur, the film-edge immediately adjacent to the interface would be expected move outward relative to its initial position, resulting in an enlargement of the film-footprint on the substrate. This, in addition to the slight reduction of the edge-slope after one complete cycle (Figure 51), is consistent with experimental observations on Al-Si, as noted earlier.

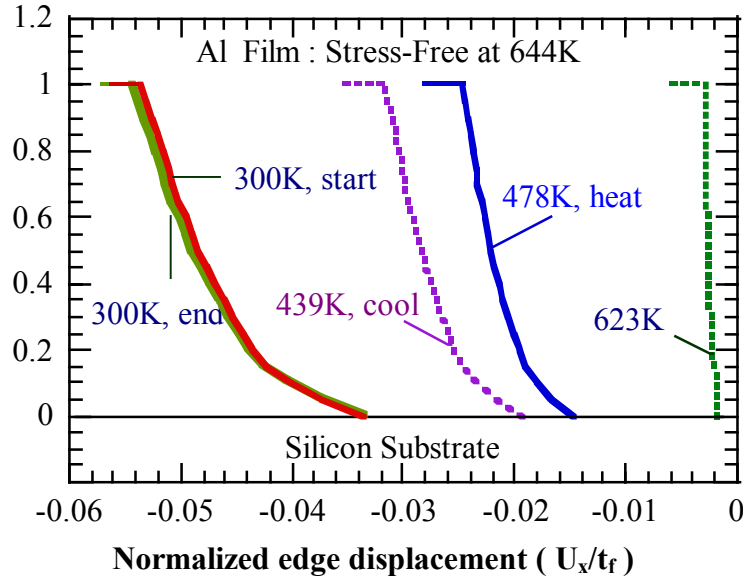


Figure 51. Computed Profiles of the Right Edge of the Al Film at Different Temperatures during Heating and Cooling. The Horizontal Line at the Top of Each Edge-Profile Has Been Drawn in to Delineate the Film Edge Clearly, and Do Not Represent the Actual Data.[6]

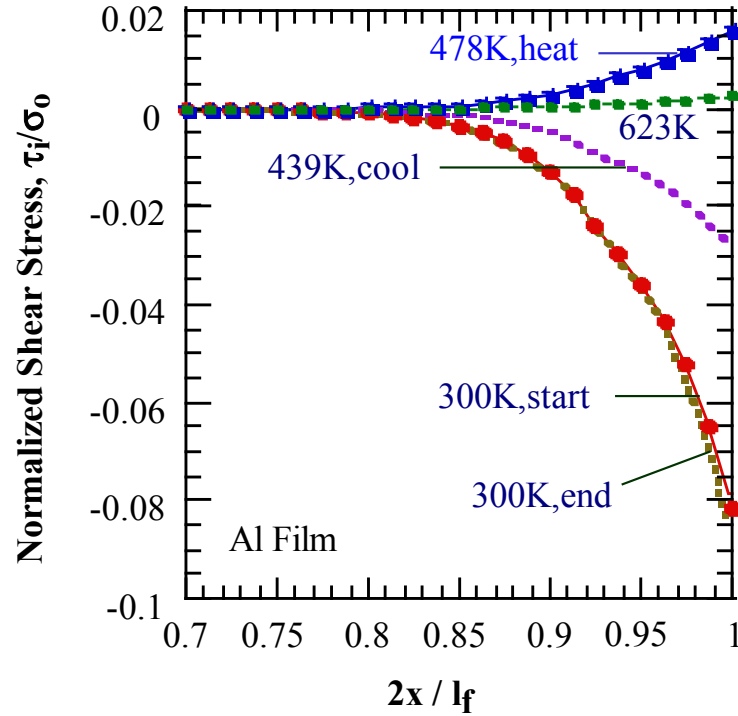


Figure 52. Distribution of Interfacial Shear stress  $\tau_i$  Close the Edge of Al Film at Different Temperatures during Thermal Cycling. [6]

Figures 53 through 56 show the equivalent plots for electroplated Cu on Si. The Cu is assumed to be stress-free at ambient temperature, since electroplated Cu has been observed to be nearly-stress free immediately following annealing [95]. As observed in Figure 53, even though the in-plane film stress starts at zero, it ratchets up and settles at a small positive value after one cycle. Following the first cycle, though, the stress does not ratchet up significantly any more. As in the case of Al, during heating, the stress builds up to a significant compressive value before relaxation via creep and plasticity occurs. Unlike in Al, however, even at the high temperature end of the cycle, the stress is not completely relieved, and the film remains in significant compression. During cooling, the compressive stress is relieved, and a tensile stress builds up, rapidly at first, and more slowly subsequently as the film undergoes plastic yielding. From the associated VM plastic strain plot, it is noted that unlike in the case of Al, the Cu film deforms by plastic yielding during heating (between 450 and 723K) as well as during cooling (below 400K).

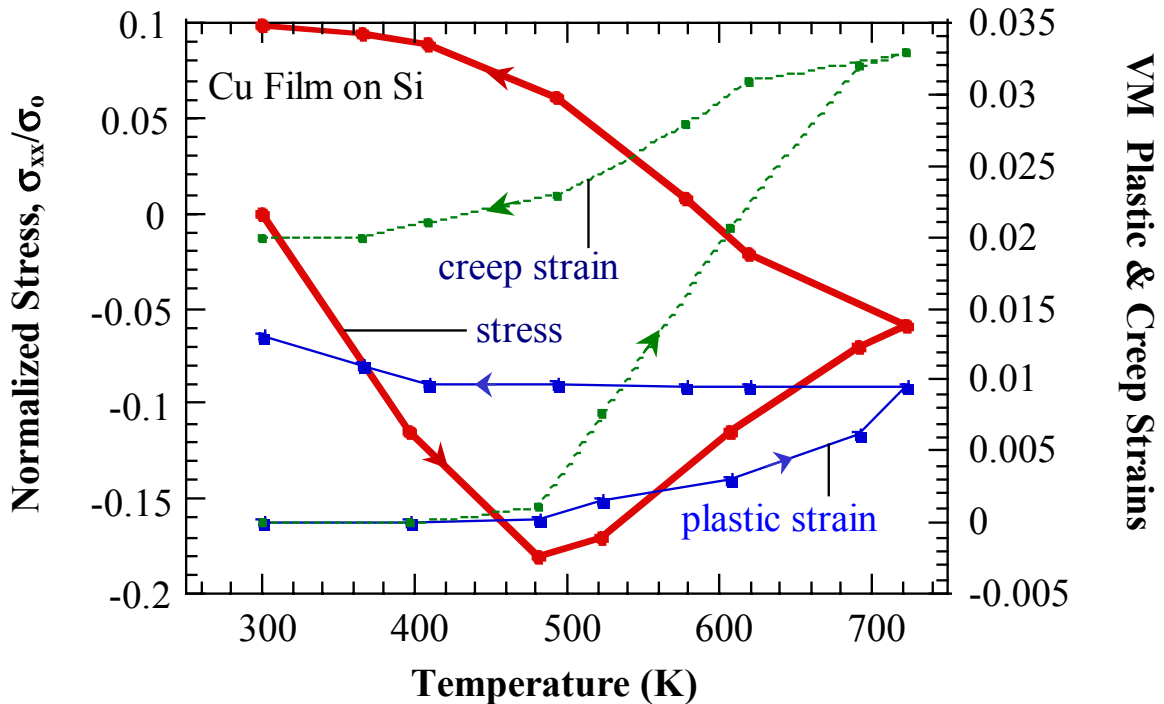


Figure 53. Computed Variation of  $\sigma_{xx}$  and the Von-Mises Effective Plastic and Creep Strains in an Cu Film on Si during Thermal Cycling. [6]

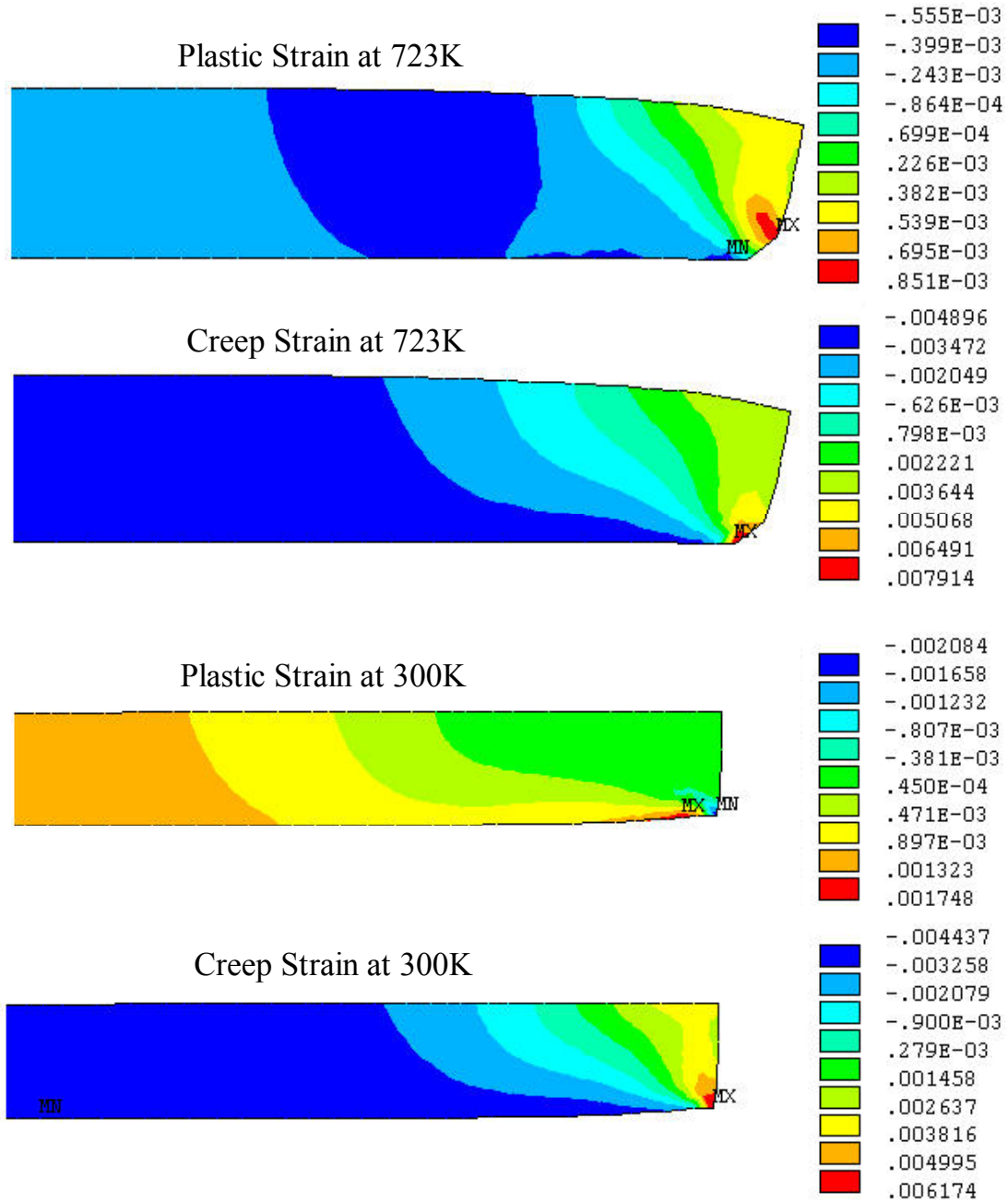


Figure 54. The Distribution of In-Plane Plastic and Creep Strains Near the Edge of the Cu Film at the End of the Heating Segment (723K) and at the End of the Thermal Cycle (300K). The Displacement Scaling Has Been Exaggerated to Reveal Changes in the Edge Profile Associated with Cycling. The Middle of the Film Lies Far Away (Beyond the Picture) Towards the Left. All the Contour Plots Have the Same Scaling, and the Observed Differences in Size and Location in the x-Direction Between the Two Temperatures are Representative of Reality. [6]



Figure 54 shows the distribution of  $\epsilon_{xx}^{pl}$  and  $\epsilon_{xx}^{crp}$  close to the edge of the Cu film at the ends of the heating and cooling segments of the thermal cycle (723K and 300K). Since the film is stress-free prior to cycling at 300K, and is in deep compression at 723K (see Figure 53), both  $\epsilon_{xx}^{pl}$  and  $\epsilon_{xx}^{crp}$  are in compression through most of the film away from the edge. During subsequent cooling, tensile creep occurs, but a significant negative creep strain is left at 300K. Concurrently, a small tensile plastic strain is induced at the lower temperatures, but the net inelastic strain after 1 complete cycle is still fairly large and compressive. This is consistent with Figure 53, from which it may be inferred that compressive creep contributes a large proportion of the inelastic strain during one complete cycle, resulting in a net compressive inelastic strain.

Again, since the model does not allow interfacial sliding, the compressive inelastic strain should not alter the footprint of the film on the substrate, although it causes a change in the edge profile of the film. Figure 55 shows the profile of the right edge of the Cu film at different stages during the thermal cycle. Because of the absence of stress at the starting temperature, the film starts out with a vertical right-edge profile. Upon heating, the film-edge profile begins to slope outwards from the interface to the top, the slope becoming shallower with increasing temperature. Upon cooling, the edge-slope becomes steeper, and eventually settles at a small but finite value away from the vertical. Interestingly, the footprint of the film on the substrate appears to be significantly smaller at the end of the cycle, although interfacial sliding was not accounted for in the model. This is attributable to the accommodation of compressive inelastic deformation of the film by elastic deformation of the substrate. This point is discussed further in section 6.

Figure 56 shows the distribution of  $\tau_i$  near the edge of the Cu film at various temperatures.  $\sigma_{xx}$  is compressive during the entire heating segment and the associated positive  $\tau_i$  would tend to make the film-edge move inward (towards smaller  $2x/l_f$ ) if sliding were allowed. This trend continues even during the cooling segment till  $\sigma_{xx}$  becomes tensile around 550K, below which  $\tau_i$  assumes a small negative value and tends to make the interface slide to the right. Overall though, if interfacial sliding could occur,

the sense of  $\tau_i$  over most of the thermal cycle would result in a net shrinkage of the film-footprint on the substrate, with the film edge moving inward. Once again, this is consistent with the trends observed experimentally on the Cu-Si sample.

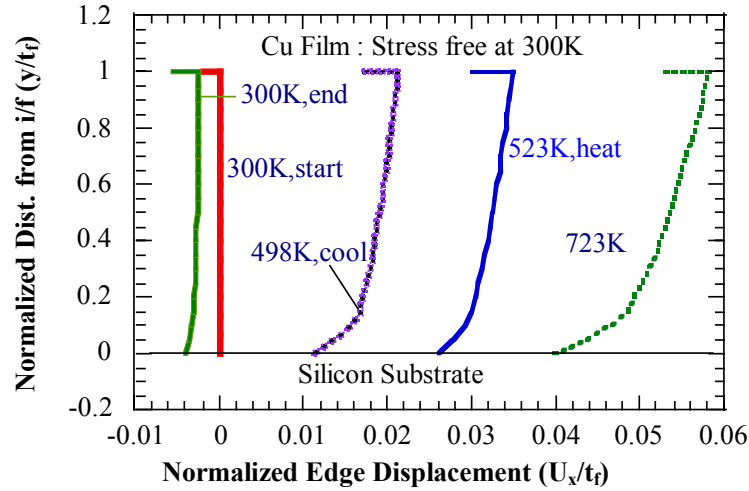


Figure 55. Computed Profiles of the Right Edge of the Cu Film at Different Temperatures During Heating and Cooling. The Horizontal Line at the Top of Each Edge-Profile Has Been Drawn in to Delineate the Film Edge Clearly, and Do Not Represent the Actual Data. [6]

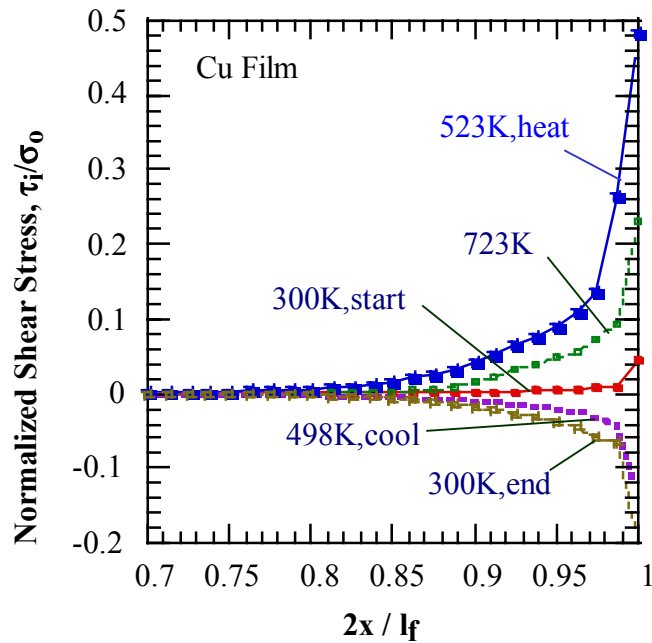


Figure 56. Distribution of Interfacial Shear Stress  $\tau_i$  Close the Edge of Cu Film at Different Temperatures During Thermal Cycling. [6]

## 6. Discussion

As noted above, the model showed that the Cu film displays an apparent footprint change even though interfacial sliding was not allowed. This is primarily attributable to the large net inelastic compressive deformation of the film during a complete thermal cycle, and the associated inability of the film stress to return to its starting value, as noted in Figure 54. Since the film ends with a tensile stress despite starting out stress-free, the substrate ends up with a compressive stress, and hence is elastically compressed at the end of the cycle relative to its starting state. This contraction of the substrate following cycling is responsible for the contraction of the line width apparent in Figure 55. Thus, a ratcheting of the stress state would typically be associated with an apparent change in line footprint, even when interfacial sliding does not occur. However, it should be noted that in the model, our substrate was only  $5\mu\text{m}$  thick, and therefore, would be expected to display significantly greater contraction than real Si substrates, which are typically  $500\text{--}700\mu\text{m}$  thick. As observed in Figure 55, the displacement of the film edge after one cycle is  $\sim 0.04t_f$ , which amounts to a footprint change of about  $8\text{nm}$ . In the experiment, the Si wafer was  $\sim 725\mu\text{m}$  thick, and therefore, apparent changes in film footprint due to elastic deformation of the substrate would be much less than  $8\text{nm}$ , and hence indiscernible in the AFM. Since we observe a mean film shrinkage of  $\sim 47\text{ nm}$  after the first cycle, and  $\sim 135\text{nm}$  after the fifth (Figure 46), this must be due to interfacial sliding.

Because of the paucity of lattice dislocations and the difficulty of dislocation glide in thin films [76], the yield strength of thin films is usually high, and plastic deformation via dislocation glide at low temperatures is likely to be limited during thermal cycling. The dominant mechanism of plastic deformation of the thin film is therefore believed to be creep/stress relaxation. Indeed, Cu films on Si have been noted to creep at temperatures as low as  $333\text{K}$  during thermal cycling [15] whereas Al films on  $\text{Al}_2\text{O}_3$  have been thought to creep at even lower temperatures [16]. This is also borne out by the FEM results presented above, even though accurate temperature-dependent yield strength and creep data for thin films were not available for the model, and diffusional creep effects were ignored (which would have the effect of overestimating plastic strains and underestimating creep strains). In practice, therefore, creep effects are even more

accentuated during thermal cycling than the FEM results would suggest. If interfacial sliding were not allowed, these large creep strains would simply result in stress relaxation of the film, with no discernible dimensional change. However, if interfacial sliding is allowed to occur, permanent relative change between the dimensions of the metal film and the Si substrate at the interface would be expected, as observed here experimentally. It is therefore believed that near the edges of the film, creep relaxation of the film is accommodated by interfacial sliding due to the presence of interfacial shear stresses, thereby allowing the film-dimensions to change. Since the permanent differential strain measured in the present work is ~3-8%, which is much larger than the differential thermal expansion of the Al or Cu relative to Si over the entire test temperature range, it is inferred that the observed plastic strain accrues cumulatively during thermal cycling due to continuous stress and temperature revision. This is consistent with Figure 46, which clearly demonstrates the cumulative nature of interfacial sliding displacement.

From the experimental results, it is interesting to note that the change in the Cu-line width after 5 cycles amounts to an average plastic strain of ~8%, which is significantly larger than the 3% plastic strain observed in the much wider Al films. This is despite the fact that the net inelastic strain induced in Cu during thermal cycling is on the same order (or somewhat smaller) as those in Al (compare Figures 49 and 53). This is consistent with the notion that interfacial sliding occurs only near the edges of the film where the shear stresses are significant. The Cu lines, being significantly narrower than the Al films in the present work, allow interfacial sliding to occur over a larger fraction of the line-width than the Al films. Since interfacial sliding is necessary to accommodate differential deformation of the film and Si, the Cu line shows a larger proportionate change in width than the Al films.

It was noted in the experiments that the edge-profile of the Cu line became steeper during cycling, as the Cu lines shrank. The model, however, showed that an originally vertical edge-profile developed a slope during cycling. However, these observations are not inconsistent when the nature of the slopes is taken into account. In the model, an originally vertical profile became positively sloped (sloping outward from the interface to the film surface, or acute angle  $\theta$  between film-edge and substrate surface). In the

experiment, an originally negative edge-profile (sloping inward from the interface to the film surface, or obtuse angle  $\theta$  between film-edge and substrate surface) tended to become vertical. Thus both model and experiment resulted in changes in the same direction, with  $\theta$  decreasing due to cycling.

The shape change of films wherein the slope of the side faces changes after thermal cycling indicates that plastic deformation of the films is non-uniform in the through-thickness direction, and the typically assumed plane-stress condition is not valid at the microscopic level. Generally, following thermal cycling, the film is strained to a greater extent close to the film-substrate interfaces. This is primarily because the film has a through-thickness gradient of in-plane normal stresses, particularly near the edges. The in-plane stresses are typically largest at the interface, thereby allowing maximum creep/plasticity near the interface, as demonstrated by the strain distributions in Figures 50 and 54. Also, near the interface, the film creep may be accommodated by interfacial creep, allowing the film dimensions to alter more.

From Figure 48, it is noted that with decreasing film aspect ratios (ratio of line-width to line-thickness), an increasingly larger proportion of the interface is subjected to shear stresses. Furthermore, significant peeling stresses (normal tensile stresses) may act on the interface near the film edges, the extent of the film subjected to such peeling stresses increasing with decreasing film aspect ratio. Indeed, as evident from Figure 48, for a film thickness of  $0.1\mu\text{m}$  and a line width of  $1\mu\text{m}$ , interfacial shear stresses prevail over nearly the entire film width, and tensile peeling stresses exist over a distance of about 20% of the film-width from each film-edge. It is this combination of interfacial shear stress and the normal peeling stress near the edges of the film that is thought to drive interfacial sliding in order to accommodate creep deformation of the film. Clearly, the sense of the interfacial shear stress changes depending on the stress state of the film, as noted earlier for Al and Cu, allowing the film to either expand or shrink relative to the substrate. With an alteration of the in-plane stress state, the normal interfacial stress  $\sigma_i$  also changes sign, being tensile (peeling) for a tensile  $\sigma_{xx}$ , and compressive for a compressive  $\sigma_{xx}$ . Thus for equal magnitudes of the interfacial shear stress  $\tau_i$ , the

interfacial creep rate ( $\dot{\gamma}_i$ ) should be greater when the film is in tension (since  $\sigma_i$  will augment  $\tau_i$ ; Equation 6.1), and slower when the film is in compression (since  $\sigma_i$  will result in a threshold stress; Equation 6.1). The sliding rate is also enhanced by smoother interfaces (smaller values of  $h$ ), which is why films deposited on smooth wafers (RMS roughness of  $<1\text{nm}$ , as in our experiments) display significant size changes. Interestingly, whereas a smoother interface tends to increase the sliding rate, it reduces the impact of the normal stress, since the effect of  $\sigma_i$  scales with  $(h/\lambda)^3$ . Therefore, for very smooth interfaces, the effect of the normal stress may become quite small, resulting in little noticeable difference in the sliding rates for films in tension and compression.

In summary, the phenomenon of interfacial sliding-accommodated inelastic deformation of films would be expected to be more prominent for films with small lateral dimensions (e.g., narrow lines) and smooth interfaces. As the micro-electronic industry moves towards progressively larger-scale integration, dimensional stability of metallic lines is likely to become increasingly important, making it critical to understand the mechanisms and kinetics of interfacial sliding. In particular, it is necessary to develop methodologies to characterize the kinetics of interfacial sliding, and analytical techniques to account for these effects in modeling efforts. This is particularly important since with the advent of new generations of dielectric films with low elastic moduli (which may be more than an order of magnitude smaller than those of metallic films), the constraint traditionally imposed on the deformation of metal lines by stiff oxide passivations is no longer available.

## 7. Conclusions

The cross-sectional profiles of thin Al and Cu films on Si substrates were measured using AFM before and after thermal cycling under different conditions. It was observed that thermal cycling resulted in alteration of the lateral film dimensions, with the Al film expanding and the Cu lines shrinking relative to the substrate. Additionally, the edge profiles of the films were found to change because of through-thickness variations in the film stress and strain states, particularly near the edges. These changes were attributed to inelastic deformation of the film (mainly creep and some plastic

yielding), accommodated by diffusionally accommodated sliding at the interface. This sliding process is driven by interfacial shear stresses, and may either be augmented or ameliorated by interfacial normal stresses.

The evolution of stress and strain states within the film during thermal cycling was modeled using finite element analysis, and the observations were found to be consistent with the experimental trends. It was observed that large interfacial shear stresses usually exist near the edges of thin films, in association with in-plane film stresses, which arise due to thermal expansion mismatch between the film and the substrate. It was further noted that with decreasing lateral film dimensions, interfacial shear stresses exist over a larger proportion of the film width. Since interfacial sliding is driven by these shear stresses, it is limited to regions very close to the film edge for large-area films. Therefore, for large-area films, dimensional changes due to interfacial sliding and film plasticity are negligible compared to film dimensions. However, with decreasing film dimensions, interfacial sliding, and hence changes in film dimensions, become more prominent.

The model also predicted slope changes of the film-edge profile due to through-thickness strain variations near the film edges, the predicted trends being consistent with experiments. Further, the model showed that the sense of the interfacial shear stress changes depending on whether the film is in in-plane tension or compression. This allows the direction of interfacial sliding to adjust itself so that the footprint of films subjected to a net tensile inelastic strain during thermal cycling can expand relative to the substrate, whereas films subjected to a net compressive inelastic strain can contract. This is consistent with the experimental observation that evaporated Al films expand whereas electroplated Cu films contract relative to the substrate during cycling. Finally, it was noted that decreasing interfacial roughness accelerates interfacial sliding, while reducing the contribution of interfacial normal stresses to the sliding kinetics.

## **B. Cu/LOW k DIELECTRIC STRUCTURES ON Si**

Published in Silicon Materials Processing-Characterization and Reliability, Veteran, J, O'Meara, D. L., Misra, V., Ho, P., eds., MRS Symp. Proc., 2002.  
(co-authored with I. Dutta and C. Park)

### **1. Introduction**

The large mismatch in the coefficients of thermal expansion (CTE) between metallic thin films and Si substrates usually causes plasticity and creep of the film during thermal cycling [15]. This mismatch also generates shear stresses at the interface, which can drive diffusionally accommodated interfacial sliding, resulting in alteration of the film footprint on the substrate [6, 8, 9]. In large-area films, these shear stresses (and hence sliding) are limited to regions close to the film-edges; but for films with small lateral dimensions (e.g., narrow interconnect lines), sliding may occur over a large area-fraction of the interface. In Al/SiO<sub>2</sub> back-end interconnect structures (BEIS), sliding and the associated line-dimension changes are constrained by the stiff SiO<sub>2</sub> dielectric. However, with the increasing use of mechanically compliant low-k dielectrics (LKD) in the back-ends of modern devices, changes in line dimensions due to plasticity and sliding are unlikely to be fully constrained. This is particularly exacerbated by global shear stresses imposed on the BEIS due to joining of the device to a package-level substrate (typically an organic with a much higher CTE than Si). Under the joint action of the local (film/Si level) and global (Si/package level) stresses, the film can yield incrementally during each thermal cycle, resulting in crawling of the film on the substrate in the direction of the global shear stress [96]. Under interfacial sliding conditions, crawling is likely to be exaggerated, particularly when the surrounding LKD is unable to provide sufficient mechanical constraint, possibly resulting in shifting line positions and large-scale line distortions. In addition to occurring along the in-plane Cu/Si interfaces, sliding also occurs at vertical Cu/LKD interfaces due to out-of-plane CTE mismatch between Cu and LKD, causing steps to appear at these interfaces [11, 97].



In this section, we present results of atomic force microscopy (AFM) measurements of both lateral and out-of-plane dimensions of (a) stand-alone Cu lines on Si, and (b) Cu/LKD structures on Si, with the intent of delineating the role of interfacial sliding during thermal cycling of devices during processing and service. Some preliminary observations of deformation of back-end structures due to global package-level loads are also reported.

## 2. Experimental Approach

Three types of samples were used for the AFM experiments. The first type (A) comprised a pattern of parallel 1.4  $\mu\text{m}$  wide, 250nm thick, electroplated Cu lines with a pitch of 2  $\mu\text{m}$  on Si with a 35nm Ta barrier layer at the interface. This sample was utilized to study deformation and sliding of standalone Cu lines on Si along both *in-plane* (IP) and *out-of plane* (OOP) directions. The second sample type (B) consisted of one layer of 350nm thick, alternating parallel Cu and LKD lines on Si. The width of the Cu lines, which were surrounded on the sides and bottom by a 35nm thick Ta barrier layer, varied from 0.2 to 1.8 $\mu\text{m}$ , with the corresponding LKD width ranging from 1.4 to 1.1 $\mu\text{m}$ . This sample, fabricated via the damascene process using a hybrid organic/inorganic silicate-based LKD, and chemo-mechanically polished (CMP) to produce a nominally flat surface, was used to study deformation and sliding along the OOP direction. Both samples were annealed for 30 minutes at 673K after Cu-electroplating, producing Cu lines, which were nearly stress-free at 293K [95, 98]. Both samples A and B were subjected to 5 thermal cycles from 293K to 723K in vacuum at nominal heating and cooling rates of 10K/minute, and the surface profiles were measured perpendicular to the Cu line length before and after each cycle by an AFM at 293K. Sample B was also cycled *in-situ* in the AFM (in air) from 293K to 398K, and the profiles were recorded at selected temperatures.

A third type of sample (C) comprised a single layer of alternating Cu/LKD lines, capped by a 200nm LKD layer. The sample cross-section was revealed by micro-cleaving normal to the interconnect lines, followed by focused ion beam (FIB) polishing. The sample was then bonded to an Al plate ( $\text{CTE} = 22 \times 10^{-6}/\text{K}$ ) using a glass-filled epoxy

( $E = 11\text{GPa}$ ,  $\text{CTE} = 21 \times 10^{-6}/\text{K}$ ) and cycled *in-situ* in the AFM to simulate and observe BEIS deformation due to stresses related to flip-chip packaging.

### 3. Results and Discussion

Figure 41 shows typical profiles of a standalone Cu line (Sample A) prior to, and following the first through fifth cycle between 293 and 723K. A perspective AFM image of the Cu line structure on Si is also shown as an inset. The Cu lines are observed to shrink laterally with progressive cycling, along with a corresponding increase in line thickness (height). Statistical analysis of the line profiles revealed that the rate of these changes slowed with progressive

Figures 57 and 58 show typical surface and profiles of sample B (Cu/LKD) before and after cycling from 293-723K. Before cycling, a  $\sim 10\text{nm}$  step was noted on the sample-surface at the vertical Cu/LKD interfaces, indicating that the Cu lines were a little thicker than the LKD after CMP. After cycling, the interfacial step height ( $\Delta_i$ ) was found to change differently for different Cu line widths. This is shown in the surface step height vs. probability plots in Figure 59, which show that  $\Delta_i$  increases with cycling for  $1.8\mu\text{m}$  wide Cu lines, remains roughly unaltered for  $0.8\mu\text{m}$  lines, and decreases with cycling for  $0.2\mu\text{m}$  wide lines. As noted in Figure 45 the  $1.8\mu\text{m}$  Cu lines are expected to shrink appreciably in the IP direction. The adjacent LKD lines are unlikely to be able to constrain this deformation because of the low Young's modulus of LKD ( $4\text{-}5\text{GPa}$ ) relative to Cu ( $130\text{GPa}$ ). Assuming that the vertical Cu/Ta/LKD interfaces are strongly bonded, the large lateral shrinkage of the Cu lines places the intervening LKD in IP tension, resulting in OOP shrinkage of the LKD due to Poisson effect as shown in Figure 60a. Estimating the OOP Poisson's ratio of the LKD to be 0.2 and a  $40\text{nm}$  IP expansion of the  $1.4\mu\text{m}$  wide LKD (i.e.,  $20\text{nm}$  contraction of the  $1.8\mu\text{m}$  Cu line on each side) would result in OOP shrinkage of  $\sim 2\text{nm}$  per cycle. When the OOP expansion associated with the IP contraction of the Cu lines is added to this OOP shrinkage of LKD,  $\Delta_i$  can increase considerably, as observed in Figure 59a.

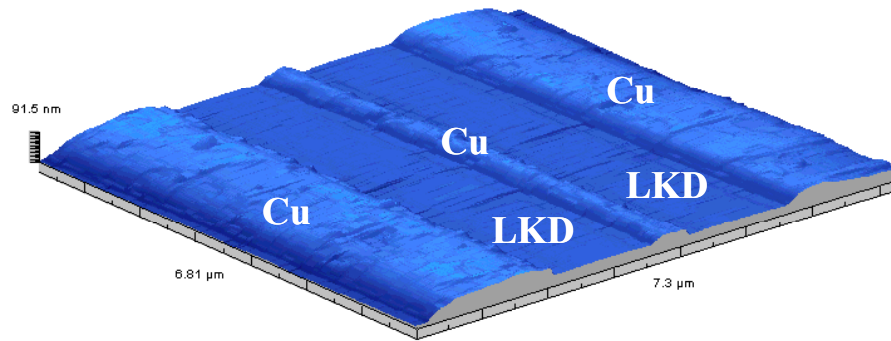


Figure 57. AFM Image of the CMPed Surface of a Single Level Interconnect Structure on a Si Device, Consisting of Parallel Cu Lines of Alternating Widths of 1.8 and 0.2 μm, Separated by a Low-K Dielectric (LKD).

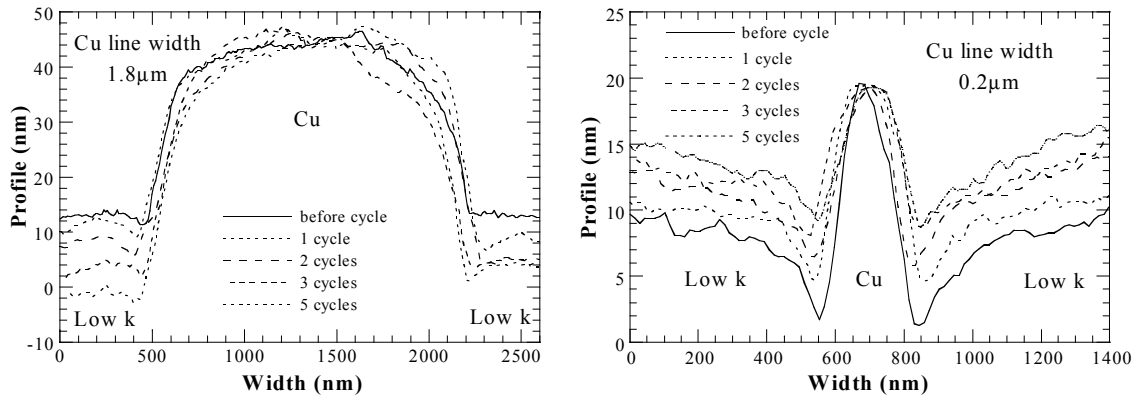


Figure 58. Surface Profiles Showing Changes in Interfacial Step Height Between Cu and LKD During Thermal Cycling Over 293-723K.

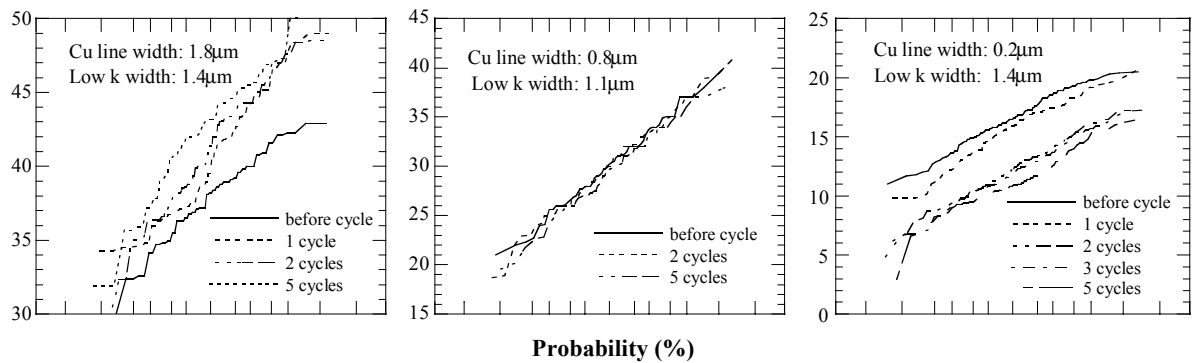


Figure 59. Change in Interfacial Step Height vs. Probability for 1.8, 0.8 and 0.2 μm Wide Cu Lines Following Thermal Cycling from 298K to 723K.



creep significantly at temperatures above 323-343K [15, 99]. This permanent OOP shrinkage of Cu relative to LKD is consistent with the decrease of  $\Delta_i$  after cycling observed in Figure 59c. It should be noted that the observed shrinkage of Cu relative to LKD can also be rationalized by assuming OOP inelastic deformation of the LKD at high temperatures under the tensile constraint imposed by the Cu lines. However, this is incompatible with Figure 59a, where the *wider* Cu lines would be expected to impose greater OOP tensile constraint, and therefore cause greater expansion of the LKD relative to Cu, instead of the observed shrinkage as shown in Figure 60b. Therefore, OOP inelastic deformation of LKD does not appear to be an issue. In summary, for all Cu line widths, the OOP step height changes are driven by both IP and OOP deformation of Cu, with the effects of IP deformation dominating for wide Cu lines, OOP deformation dominating for narrow Cu lines, and both effects having roughly equal but opposite contributions for Cu lines of intermediate width (Figure 59b).

The observation that all changes in step height occur exactly at the interface (Figure 58) suggests that the differential OOP deformation of Cu and LKD is

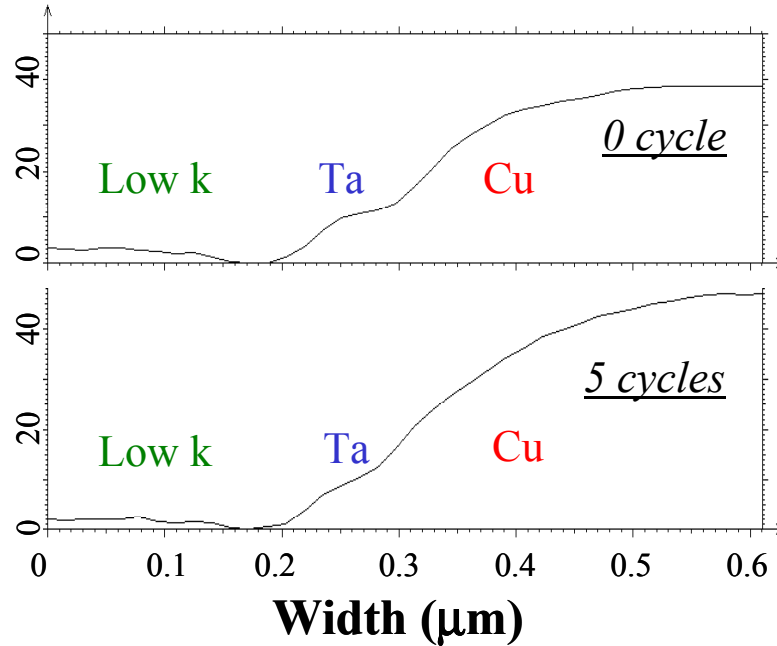


Figure 61. Cu Line Edge Profile Before and After 5 Thermal Cycles from 298K to 723K in Vacuum.

accommodated at the interface by a sliding mechanism. This is illustrated by the edge profile of a Cu line before and after cycling till 723K, shown in Figure 61. The height difference between LKD and the Ta barrier layer is observed to remain constant, whereas the height difference between Ta and Cu line changes upon cycling. This demonstrates that the differential deformation between Cu and LKD is accommodated at the Cu/Ta interface, consistent with the findings of [Reference 11](#). The mechanism of this sliding phenomenon is discussed later.

Figures 62a and b show the *in-situ* surface profiles of sample B straddling the 0.2 and 0.8 $\mu$ m wide lines, respectively, at different stages of a 293-398K cycle. For neither line is any significant change in  $\Delta_i$  noted between 293 and 348K. However, between 348 and 398K, the step height increases significantly, this being more prominent for the wide Cu lines. Upon cooling back to 293K,  $\Delta_i$  decreases slightly, but remains larger than before cycling. Because of the low temperatures involved, inelastic deformation of Cu is not expected. However, during heating, the differential expansion of Cu and LKD can be accommodated by interfacial sliding, but only at the higher end of the temperature range (>348K). It should be noted that two separate effects drive the increase in  $\Delta_i$  at the higher temperatures: (a) greater OOP expansion of Cu relative to LKD, and (b) smaller IP expansion of LKD relative to Si, which causes a small OOP contraction of LKD. Still, both these effects combined are expected to cause no more than 2-3 nm of step height increase in the prescribed temperature range. Since this is much smaller than the observed increase in  $\Delta_i$ , it is believed that the balance is due to oxidation of the Cu lines during cycling in air. A recent study showed that Cu thin films rapidly grow a compact Cu<sub>2</sub>O layer under 523K, which protects the film from further oxidation [100]. At 398K, this layer can be estimated to be ~2nm thick. In addition to this continuous oxide layer, discontinuous growth of oxide particles, ~2-4nm in thickness, were observed on the Cu lines in our samples. Therefore, it can be inferred that of the 6-10nm of  $\Delta_i$  increase noted in Figure 62, 4-6nm is attributable to oxide layer growth, whereas the balance is likely due to interfacial sliding under the shear stress which develops in the OOP direction due to CTE mismatch between Cu and LKD.

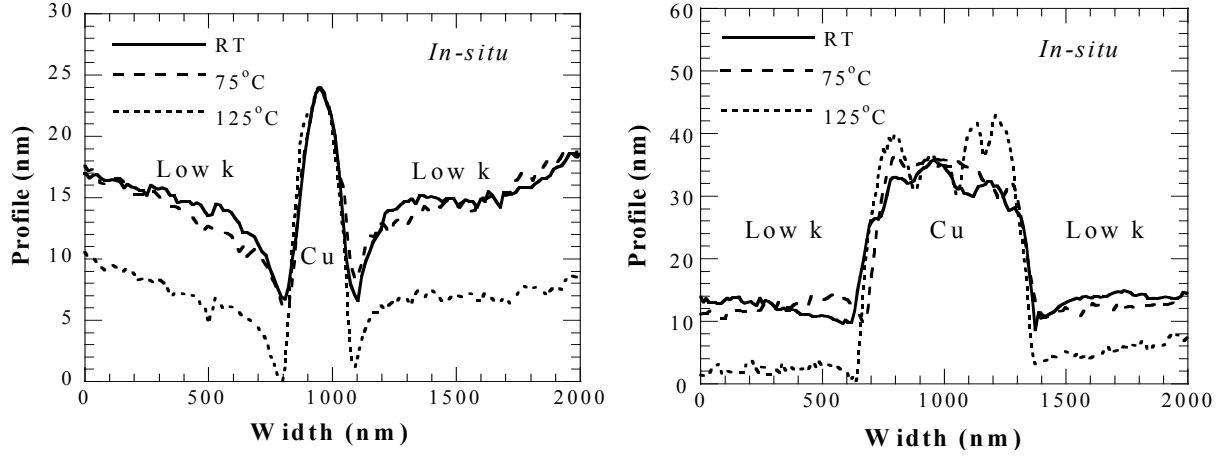


Figure 62. In-Situ Surface AFM Profiles for Sample B for 0.2μm and 0.8μm Cu Lines at 298, 348 and 398K.

Funn and Dutta [3] have shown that interfaces between dissimilar materials slide by a diffusional creep process akin to grain boundary sliding [32], the sliding rate  $\dot{\gamma}_i$  being given by:

$$\dot{\gamma}_i \approx \frac{4\delta_i D_i \Omega}{kTh^3} \left[ \tau_i + 2\pi^3 \left( \frac{h}{\lambda} \right)^3 \sigma_n \right] \quad (6.3)$$

where  $\tau_i$  and  $\sigma_n$  are the shear and normal stresses acting on the interface, respectively,  $D_i$  is the interface diffusivity,  $\Omega$  is the atomic volume of the film species,  $\delta_i$  is the interfacial thickness, and  $\lambda$  and  $h$  are the morphological periodicity and roughness, respectively, of the interface. The combination of far-field  $\tau_i$  and  $\sigma_n$  produce local normal stress gradients at the interface, which drive diffusive fluxes along the interface, resulting in relative movement of the two sides. Recent experiments on model Al-Si interfaces [58] showed that very thin amorphous layers often present at interfaces act as fast diffusivity paths, leading to rapid sliding even at relatively low applied shear stresses and temperatures. Since  $\dot{\gamma}_i$  is enhanced by smooth interfaces (small  $h$ ), most interfaces encountered in microelectronics are highly susceptible to sliding. In particular, interfaces

with a tensile  $\sigma_n$  are particularly susceptible, since this augments the effective  $\tau_i$ . In the interconnect structures discussed above, sliding occurs along the Cu/Ta interfaces due to rapid interfacial diffusion of Cu, driven by the shear stresses which arise due to CTE mismatch of Cu with Si or LKD, and assisted by the smoothness of the interfaces ( $h < 1\text{nm}$ ). This is aided when a tensile  $\sigma_n$  is present (e.g., at vertical Cu/LKD interfaces due to lateral Cu line shrinkage, Figure 59a).

In addition to the effects of chip-level stresses discussed above, very large package-level shear stresses are induced in the BEIS when a Si device joined to an organic substrate is thermally cycled. These stresses increase with increasing in-plane distance from the center of the chip, and may be large enough to cause large-scale plasticity of the Cu lines. Figure 63a shows a cross-section of sample C, revealing alternating narrow and wide Cu lines embedded in LKD. During *in-situ* cycling, the cross-section of one of the narrow ( $0.4\mu\text{m}$ ) lines was observed, and points along the perimeter of the line at an elevation of 20nm from the adjacent regions (Si or LKD) were recorded from a series of line profiles. The locus of these points was then plotted to reveal the outline of the Cu line at different stages of thermal cycling (Figure 63b). It is seen that the line undergoes large shear distortion during heating to 398K, much of which remains upon cooling to 298K, suggesting that the line is plastically deformed. This is consistent with the phenomenon of film crawling during thermal cycling, where Al lines on Si were noted to deform in shear, with the strain ratcheting up with increasing number of cycles, eventually breaking a SiN barrier layer surrounding the line [96]. It is possible that similar effects may be observed in the present system after numerous cycles, with the distorted Cu line breaking the Ta barrier layer, and migrating laterally relative to Ta via interfacial creep. The inability of the LKD to constrain such migration makes this a likely failure mechanism in Cu/LKD BEIS. Studies are currently under way to identify the various deformation mechanisms operative in BEIS.



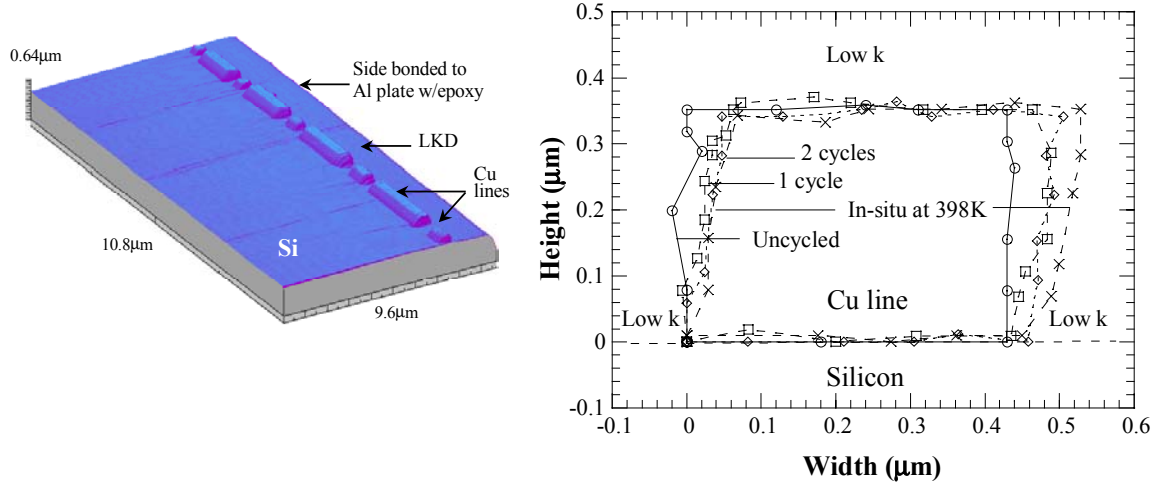


Figure 63. (a) AFM Image Showing Cross-Section of Cu/LKD Structure on Si. (b) Perimeter of a 0.4μm Wide Cu Line at Different tages of Thermal Cycling from 298K to 398K.

#### 4. Conclusions

Thermal cycling resulted in lateral shrinkage of Cu lines on Si, along with a change in edge-profile. This was attributed to inelastic deformation of the film, accommodated by diffusional interfacial sliding. Lateral Cu-line shrinkage, along with CTE mismatch between Cu and dielectric, also provided the driving force for out-of-plane interfacial sliding, which accentuated steps on CMPed single layer Cu/low-K structures. Narrow, 0.2μm Cu lines also underwent out-of-plane inelasticity due to CTE mismatch with low-K. Observations of the cross-sectional perimeter of a 0.4μm wide Cu line embedded in low-K showed that under package level stresses, Cu lines undergo permanent shear deformation, which increases progressively with cycling.

## VII. CONCLUSIONS

The mechanical behavior of interfaces plays a key role in the overall performance of structures. In multicomponent structures, shear stresses frequently arise during thermomechanical excursions due to differential expansion/contraction between the different components. At elevated temperatures, interfaces can undergo diffusionally accommodated sliding (interfacial creep) to relieve the thermal stresses, usually resulting in dimensional changes, which affect the overall reliability and performance of the system. In this dissertation, a methodology for measuring interfacial sliding in engineering systems was developed to study the mechanism and kinetics of interfacial creep, and the impact of this phenomenon on thin film-substrate applicable to microelectronics was investigated.

Initially, well-bonded Si/Al interfaces were produced via diffusion bonding in high vacuum at 843K for 1 hour with an applied pressure of 1.5 MPa in a uni-axial compression die. An experimental approach to isolate and measure the creep behavior of interfaces in multi-component systems was refined, and used to study model diffusion-bonded Al-Si interfaces. The kinetic parameters for interface sliding were experimentally determined for the Si-Al system by measuring the interface displacement rates at various temperatures while varying the interfacial shear stress, normal stress, and roughness. All the experiments thus far indicate that only one mechanism (interfacial diffusion-controlled diffusional creep) operates over the present testing range ( $T/T_m$  of  $\sim 0.45$ - $0.72$ ,  $\tau_i/G$  of  $\sim 2 \times 10^{-5}$  to  $2 \times 10^{-4}$  with respect to Al) with an apparent activation energy of  $\sim 42$  kJ/mol. Additionally, the interfacial normal stress ( $\sigma_n$ ) and roughness ( $h$ ) were also varied ( $\sigma_n$  of 0 to 3.0 MPa,  $h$  of  $\sim 18$ , 54, and 174 nm), resulting in alteration of the creep kinetics although the same mechanism continued to prevail. The experimental data affirms that the model proposed by Funn and Dutta [3] is accurate for planar interfaces with various interfacial roughnesses at high homologous temperatures (with respect to Al) with or without applied normal stresses.

The impact of interfacial creep on the reliability of microelectronics was evaluated via atomic force microscopy, based on stand alone Cu interconnect lines on Si and Cu/low k dielectric interconnect structures on Si. Thermal cycling experiments showed that lateral shrinkage of stand alone Cu lines on Si occurred, along with changes in the cross-sectional profiles. In the Cu/low k dielectric structures, the lateral Cu-line shrinkage, along with CTE mismatch between Cu and dielectric, also provided the driving force for out-of-plane interfacial sliding accentuating the step on an initially flat (chemically-mechanically polished) single layer Cu/low-k structure. These changes were attributed to inelastic deformation of the film, accommodated by diffusionally accommodated sliding at the interface.

Initial observations of cross-sections of the back-end structures of a Si device via atomic force microscopy revealed that Cu lines embedded in low k dielectric undergo permanent shear deformation due to package level stresses generated during thermal cycling. This can potentially lead to diffusionally accommodated interface sliding between the Cu lines and the Si substrate, enabling gross film crawling during thermo-mechanical cycling associated with service conditions. More detailed AFM observations are needed to verify this hypothesis.

## LIST OF REFERENCES

1. Yoda, S. Kurihara, N. Wakashima, K. and Umekawa, S., "Thermal Cycling Induced Deformation of Fibrous Composites with Particular Reference to the Tungsten-Copper System", *Metall. Trans.*, 9A, pp. 1229-1236, 1978.
2. Dutta, I., Mitra, S., Wiest, A. D., "Some Effects of Thermal Residual Stresses on the Strain Response of Graphite-Aluminum Composites During Thermal Cycling", in *Residual Stresses in Composites*, E.V. Barrera and I. Dutta, eds., TMS-AIME, Warrendale, Pennsylvania, pp. 273-292, 1993.
3. Funn, J. V., and Dutta, I., "Creep Behavior of Interfaces in Fiber Reinforced Metal-Matrix Composites", *Acta Mater.*, 47, pp. 149-164, 1999.
4. Nagarajan, R., Dutta, I., Funn, J. V. and Esmele, M., "Role of Interfacial Sliding on the Longitudinal Creep Response of Continuous Fiber Reinforced Metal-Matrix Composites", *Mater. Sci. Engng.*, A259, pp. 237-252, 1999.
5. Dutta, I., "Role of Interfacial and Matrix Creep During Thermal Cycling of Continuous Fiber Reinforced Metal-Matrix Composites", *Acta Mater.*, Vol. 48, pp.1055-1074, 2000.
6. Chen, M. W. and Dutta, I., *Appl. Phys. Let.*, 77, p. 4298, 2000.
7. Dutta, I., Chen, M. W., Peterson, K., Shultz, T., TMS Annual Conf., 2001.
8. Dutta, I., Chen, M. W., Peterson, K., Shultz, T., *J. Elect. Mat.*, Vol. 30, No. 12, p. 1537, 2001.
9. Dutta, I., Peterson, K. A. and Chen, M. W., in *Plasticity, Damage and Fracture at Macro, Micro and Nano Scales*, A.S. Khan and O. Lopez-Pamies, eds., NEAT Press, p. 117, 2002.
10. Peterson, K. A., Park, C. and Dutta, I., in *Silicon Materials-Processing, Characterization and Reliability*, Proc. 2002 MRS Spring Mtg., in press.
11. Zhmurkin, D. V., Gross, T. S., and Buchwalter, L. P., "Interfacial Sliding in Cu/Ta/Polyimide High Density Interconnects as a Result of Thermal Cycling", *J. Electronic. Mater.*, 26, p. 791, 1997.
12. Zhmurkin, D. V., Gross, T. S. and Buchwalter, L. P., "Interfacial Sliding in Cu/Ta/Polyimide High Density Interconnects as a Result of Thermal Cycling", in 'Creep and Stress Relaxation in Miniature Structures and Components', H. D. Merchant, ed., TMS-AIME, 1997, pp. 255-270.
13. Jobin, V. C., Raj, R. and Phoenix, S. L., "Rate Effects in Metal-Ceramic Interface Sliding from the Periodic Film Cracking Technique", *Acta Metall. Mater.*, 40, pp. 2269-2280, 1992.
14. Hu, C. K., Luther, B., Kaufman, F. B., Hummel, J., *Thin Solid Films*, 262, p. 84, 1995.

15. Thouless, M. D., Gupta, J. and Harper, J. M. E., "Stress Development and Relaxation in Copper Films During Thermal Cycling", *J. Mater. Res.*, 8, pp. 1845-1852, 1993.
16. Shen, Y.-L. and Suresh, S., "Steady-State Creep of Metal-Ceramic Multilayered Materials", *Acta Mater.*, 44, pp. 1337-1348, 1996.
17. Suhir, E., "Approximate Evaluation of the Elastic Interfacial Stresses in Thin Films with Application to High-Tc Superconducting Ceramics", *Int. J. Solids Structures*, 27, pp. 1025-1034, 1991.
18. Suhir, E., "Stresses in Bi-Metal Thermostats", *J. Appl. Mech.*, 53, pp. 657-660, 1986.
19. Suresh, S., Giannakopoulos, A. E. and Olsson, M. J., *Mech. Phys. Solids*, 42, p. 979, 1994.
20. Lambropoulos, J. C. and Wan, S. M., "Stress Concentration Along Interfaces of Elastic-Plastic Thin Films", *Mater. Sci. Eng.*, A107, pp. 169-175, 1989.
21. Kallmayer, C., Oppermann, J., Anhock, S., Klein, M., Kalicki, R., Aschenbrenner, R., Reich, H., "Reliability Investigations of Flip Chip Solder Bumps on Palladium", *Proc. 49th Electronic Comp. Tech. Conf.*, IEEE, Piscataway, NJ, pp. 135-140, 1999.
22. Wiese, S., Feustel, F., Rzepka, S., Meusel, E., "Creep and Crack Propagation in Flip Chip SnPb37 Solder Joints", *Proc. 49th Electronic Comp. Tech. Conf.*, IEEE, Piscataway, NJ, pp. 1015-1024, 1999.
23. Mishra, R. S. and Mukherjee, A. K., "On Superplasticity in Silicon Carbide Reinforced Aluminum Composites", *Scripta Metall. Mater.*, 25, pp. 271-275, 1991.
24. Mishra, R. S., Bieler, T. R. and Mukherjee, A. K., "Superplasticity in Powder Metallurgy Aluminum Alloys and Composites", *Acta Metall. Mater.*, 43, pp. 877-891, 1995.
25. Mishra, R. S., Bieler, T. R. and Mukherjee, A. K., "Mechanism of High Strain Rate Superplasticity in Aluminum Alloy Composites", *Acta Mater.*, 45, pp. 561-568, 1997.
26. Arzt, E., Ashby, M. F. and Verall, R. A., *Acta Metall.*, "Interface Controlled Diffusional Creep", 31, pp. 1977-1989, 1983.
27. Mitra, S., Dutta, I. and Hansen, R. C., "Thermal Cycling Studies of a Cross-Plied P100 Graphite Fiber Reinforced 6061 Aluminum Composite Laminate", *J. Mater. Sci.*, 26, p. 6223, 1991.
28. Furness, J. A. G. and Clyne, T. W., "Application of Scanning Laser Extensometry to Explore Thermal Cycling Creep of Metal Matrix Composites", *Mater. Sci. Engng.*, A141, pp. 199-207, 1991.

29. Cox, B. N., "Interfacial Sliding Near a Free Surface in a Fibrous or Layered Composite During Thermal Cycling ", *Acta Metall. Mater.*, 38, pp. 2411-2424, 1990.
30. Rosler, J., Bao G., and Evans, A. G., "Effects of Diffusional Relaxation on the Creep Strength of Composites", *Acta Metall. Mater.*, 39, pp. 2733-2738, 1991.
31. Rosler, J. and Evans, A. G., "Effect of Reinforcement Size on the Creep Strength of Intermetallic Matrix Composites", *Mater. Sci. Engng.*, A153, pp. 438-443, 1992.
32. Raj R. and Ashby, M. F. "On Grain Boundary Sliding and Diffusional Creep", *Metall. Trans.*, 2, pp. 1113-1127, 1971.
33. Ashby, M. F., "On Interface-Reaction Control of Nabarro-Herring Creep and Sintering", *Scripta Metall.*, Vol. 3, pp. 837-842, 1969.
34. Stang, R. G. and Barrett, C. R., "Newtonian Viscous Creep in Fe-3%Si", *Scripta Metall.*, 7, p. 233, 1973.
35. Sautter, F. K. and Chen, E. S., *Proc. Bolton Landing Conf. on Oxide Dispersion Strengthening*, Gordon & Breach, New York, p. 495, 1969.
36. Ignat, M. and Bonnet, R., "Role of the Phase Boundaries in the Hot Deformation in Tension of Al-CuAl<sub>2</sub> Single Eutectic Grains – A Deformation Model", *Acta Metall.*, 31, pp. 1991-2001, 1983.
37. Gupta, D., Vieregge, K. and Gust, W., "Interface Diffusion in Eutectic Pb-Sn Solder", *Acta Mater.*, 47, pp. 5-12, 1999.
38. Hsiung, L. M. and Nieh, T. G., "Creep Deformation of Lamellar TiAl Alloys Controlled by Viscous Glide of Interfacial Dislocations", in 'Interstitial and Substitutional Solute Effects in Intermetallics', I. Baker, R. D. Noebe and E. P. George, eds., TMS, pp. 201-210, 1998.
39. Vala, J., Svoboda, J., Kozak, V. and Cadek, J., "Modeling Discontinuous Metal Matrix Composite Behavior under Creep Conditions: Effect of Interface Diffusional Matter Transport and Interface Sliding", *Scripta Metall. Mater.*, 30, pp. 1201-1206, 1994.
40. Iyengar, N. and Curtin, W. A., "Time Dependent Failure in Fiber-Reinforced Composites by Matrix and Interface Shear Creep", *Acta Mater.*, 45, pp. 3419-3429, 1997.
41. Meyer, D. W., Cooper, R. F. and Plesha, M. E., "High Temperature Creep and the Interfacial Mechanical Response of a Ceramic Matrix Composite", *Acta Metall. Mater.*, 41, pp. 3157-3170, 1993.,
42. Mori, T., Tanaka, K., Nakasone, Y., Huang, J. and Taya, M., "Creep of a Metal Matrix Composite with or without Diffusion and Sliding on Matrix/Reinforcement Interfaces", *Key Engng Mater.*, vols. 127-131, pp. 1145-1152, 1997.

43. Ashby, M. F., "Boundary Defects and the Mechanism of Particle Movement through Crystals", *Scripta Metall.*, pp. 843-848, 1969.
44. Goto S. and Mclean, M., "Role of Interfaces in Creep of Fiber-Reinforced Metal-Matrix Composites: I. Continuous Fibers", *Acta Metall. Mater.*, 39, pp. 153-164, 1991.
45. Dlouhy, A., Merk, N., Eggeler, G., "A Microstructural Study of Creep in Short Fiber Reinforced Aluminum Alloys", *Acta Metall. Mater.*, 41, pp. 3245-3256, 1993.
46. Dlouhy, A., Eggeler, G., Merk, N., "A Micromechanical Model for Creep in Short Fiber Reinforced Aluminum Alloys", *Acta Metall. Mater.*, 43, p. 535, 1995.
47. Kelly, A. and Street, K. N., *Proc. Roy. Soc. Lond. A*, "Creep of Discontinuous Fibre Composites II: Theory for Steady State", 328, pp. 283-293, 1972.
48. Bullock, E., Mclean, M. and Miles, D. E., "Creep Behavior of a Ni-Ni<sub>3</sub>Al-Cr<sub>3</sub>C<sub>2</sub> Eutectic Composite", *Acta Metall.*, 25, pp. 333-344, 1977.
49. Kim, K. T. and McMeeking, R. M., "Power Law Creep with Interface Slip and Diffusion in a Composite Material", *Mech. Mater.*, 20, pp. 153-164, 1995.
50. Nimmagadda, P. B. R. and Sofronis, P., "Creep Strength of Fiber and Particulate Composite Materials : The Effect of Interface Slip and Diffusion", *Mech. Mater.*, 23, pp. 1-19, 1996.
51. Sofronis, P. and McMeeking, R. M., "Effect of Interface Diffusion and Slip on the Creep Resistance of Particulate Composite Materials ", *Mech. Mater.*, 18, pp. 55-68, 1992.
52. Soye, G., Elssner, G., Ruhle, M. and Raj, R., "Constrained Yielding in Niobium Single Crystals Bonded to Sapphire", *Acta Mater.*, 46, pp. 3571-3581, 1998.
53. Nimmagadda, P. B. R. and Sofronis, P., "On the Calculation of the Matrix-Reinforcement Interface Diffusion Coefficient in Diffusional Relaxation of Composite Materials at High Temperatures", *Acta Mater.*, 44, pp. 2711-2716, 1996.
54. Stobbs, W. M., "Work Hardening of Copper-Silica: Diffusional Stress Relaxation", *Philosophical Magazine*, 27, pp. 1073-109, 1973.
55. Kaur, I., Gust, W. and Kozma, L., 'Handbook of Grain Boundary and Interphase Boundary Diffusion Data', Vols. 1 & 2, Ziegler, Stuttgart, 1989.
56. Dymant, F., Iribarren, M. J., Vieregge, K. and Herzig, C., "Comparison between Interphase and Grain-Boundary Diffusion in Zirconium-Based Materials", *Phil. Mag. A*, pp. 959-9661, 1991.
57. Straumal, B. B., Klinger, L. M. and Shvindlerman, L. S., "Effect of Crystallographic Parameters of Interphase Boundaries on their Surface Tension and Parameters of the Boundary Diffusion ", *Acta Metall.*, 32, pp. 1355-1364, 1984.

58. Peterson, K. A., Dutta, I. and Chen, M. W., *Scripta Mater.*, 2002, in press.
59. Bhushan, B, Li, XD, *J. Mat. Res.*, Vol. 12, No. 1, p. 59, 1997.
60. ASM Metals Handbook, 9<sup>th</sup> Ed, Metals Park, Ohio, p. 65, 1986.
61. Mondolfo, L. F., *Aluminum Alloys*, Butterworths, London, 1976.
62. Frost, H. J. and Ashby, M. F., *Deformation Mechanisms Maps*, Pergamon Press, Oxford, 1982.
63. Whitehead, J. R., *Proc. Roy. Soc. London A*, 201, p. 109, 1950.
64. Unkov, E. D., *An Engineering Theory of Plasticity*, Buttersworths, London, 1951.
65. Klomp, J. T. and Van De Ven, A. J. C., *J. Mat. Sci.*, 15, p. 2483, 1980.
66. Humphreys, F. J., *Acta Metall.*, Vol. 25., p. 1323, 1977.
67. Humphreys, F. J., Miller, W. S., Djazeb, M. R., *Mater. Sci. Tech.*, Vol. 6, p. 1157, 1990.
68. Humphreys, F. J., Kalu, P. N., *Acta Metall.*, Vol. 38, p. 917, 1990.
69. Humphreys, F.J., *Acta Mater.*, Vol. 45, No. 12, p. 5031, 1997.
70. Ratnaparkhi, P. L. and Howe, J. M., *Acta Metall. Mater.*, Vol. 42, No. 3, p. 811, 1994.
71. He, X., Yang, S. Z., Tao, K., Fan, Y., *Mater. Lett.*, Vol. 33, p.175, 1997.
72. Ye, F., Lei, T. C., Zhou,Y., *Mater. Sci. Eng.*, A281, p. 305, 2000.
73. Koumninou, P., Stoemenos, J., Nouet, G., Karakostas, T., *J. Crystal Growth*, Vol. 203, p. 103, 1999.
74. Brandes, E. A. and Brook, G. B., *Smithell's Metals Reference Book*, Butterworth-Heinemann, Oxford, pp. 13-73, 1992.
75. Majumdar, B. S., *Titanium Matrix Composites-Mechanical Behavior*, S. Mall and T. Nicholas, eds., Technomic Publ., pp. 113-168.,1996.
76. Nix, W. D., "Mechanical Properties of Thin Films", *Metall. Trans. A*, 20A, pp. 2217-2245, 1989.
77. Peterson, K. A., Dutta, I., and Chen, M.W., *J. Mat. Proc. Tech.*, 2002, in press.
78. He, X., Yang, S. Z., Tao, K. and Fan,Y., *Mater. Lett.*, 33, 175, 1997.
79. Strombom, J., Henderson, P. J. and Savage, S. J., *Scripta Metall. Mater.*, 27, p. 1179, 1992.
80. Kingery, W. D., Bowen, H. K., Uhlmann, D. R. "Introduction Ceramics", John Wiley, 92, 1976.
81. Geiger, G. H. and Poirier ,D. H., "Transport Phenomena in Metallurgy", Addison-Wesley, Reading, MA, pp. 14-22, 1980.
82. Turnbull, D. and Hoffman, R. E., *Acta. Metall.*, 2, p. 419, 1954.



83. Valiev, R. Z., Kaibyshev, O.A., Astanin, V. V., and Emaletdinov, A. K., *Phys. Stat Sol. (a)*, 78, p. 439, 1983.
84. Kokawa, H., Watanabe, T., and Karashima, S., *Phil. Mag., A*, 44, p. 123, 1981.
85. Balluffi, R. W. and Sutton, A. P., *Interfaces in Crystalline Materials*, Clarendon Press, Oxford, p. 557, 1995.
86. Balluffi, R. W. and Cahn, J. W., *Acta. Metall.*, 29, p. 49, 1981.
87. Monty, C. and Atkinson, A., *Cryst. Latt. Def. And Amorph. Mat.*, 18, p. 97, 1989.
88. Atkinson, A., *Solid State Ionics*, 12, p. 309, 1984.
89. Atkinson, A., *Solid State Ionics*, 28-30, p. 1377, 1988.
90. Gleiter, H. and Chalmers, B., *High Angle Grain Boundaries*, Pergamon Press, New York, p. 94, 1972.
91. Peterson, N. L., *In Grain Boundary Structure and Kinetics*, American Society for Metals, Metals Park, Ohio, p. 209, 1980.
92. Atkinson, A., *J. Physique*, 46, Colloq. C4, Supple., Au no. 4, pp. C4-379, 1985.
93. Hirth, J. P. and Lothe, J., *Theory of Dislocations*, Wiley, New York, 1982.
94. Brotzen, F. R., "Mechanical Testing of Thin Films", *Int. Mater. Rev.*, 39, pp. 24-45, 1994.
95. Gignac, L. M., Rodbell, K. P., Cabral, C. Jr., Andricacos, P. C., Rice, P. M., Beyers, R. B., Locke, P. S. and Klepeis, S. J., *Proc. Mat. Res. Soc. Symp.* Vol. 564, p. 373, 1999.
96. Huang, M., Suo Z. and Ma, Q., *Acta Mater.*, 49, p. 3039, 2001.
97. Gosz, M. and Okyar, A. F., *Mech. Mater.*, 31, p. 317, 1999.
98. Lau, S. H., Huang, S. and Koo, A., *Semiconductor International*, 23, p. 239, 2000.
99. Flinn, P. A., *J. Mater. Res.*, 6, 1498, 1991.
100. Gao, W., Gong, H., He, J., Thomas, A., Chan, L. and Li, S., *Mater. Lett.*, 51, p. 78, 2001.
101. Arrhenius, S., *Z. Physik. Chem*, Vol. 4, p. 226, 1889.
102. Bhushan, B, Li, XD, *J. Mat. Res.*, Vol. 12, No. 1, p. 59, 1997.

## INITIAL DISTRIBUTION LIST

1. Defense Technical Information Center  
Ft. Belvoir, Virginia
2. Dudley Knox Library  
Naval Postgraduate School  
Monterey, California
3. Professor Indranath Dutta, Code ME/Du  
Department of Mechanical Engineering  
Naval Postgraduate School  
Monterey, California
4. Dr. K. L. Murty  
Program Director  
Metal, Ceramics, and Electronic Materials  
National Science Foundation  
Materials Research Division  
Arlington, Virginia
5. Dr. John Roese  
Space Warfare Center Systems  
San Diego, California
6. John A. Peterson  
Holiday, Florida